University of Alberta

Investigation of Flow Upstream of Hydropower Intakes

by

Md Rashedul Islam

A thesis submitted to the Faculty of Graduate Studies and Research
in partial fulfillment of the requirements for the degree of

Doctor of Philosophy
in
Water Resources Engineering

Department of Civil and Environmental Engineering

Spring 2011
Edmonton, Alberta

ABSTRACT

This thesis is primarily focused on flow-field upstream of hydropower intakes, with emphasis on the use of temperature control curtains and predicting the flow acceleration zone. By reviewing the available literature, it is concluded that the flow-field upstream of hydropower intake systems can be modeled by potential flow theory. The understanding of near intake flow-field can be useful in fish entrainment studies and in designing fish repulsion systems. To control downstream river temperatures, a flexible curtain was installed upstream of several dams in California. Flow downstream of the curtain was analyzed using a Computational Fluid Dynamic (CFD) solver with rigorous validation by experimental data. The experiment was conducted with a 4 beam Acoustic Doppler Velocimeter (ADV) probe. The study shows that wall jet properties downstream of the curtain are affected by the water depth and the inlet Reynolds number. Empirical expressions were developed to predict jet properties and the wall shear stress. Flow upstream of the curtain was analyzed using potential flow theories with validation by the CFD solver. In this part, a theory based on Schwarz-Christoffel transformation was developed to predict the flow-field upstream of the curtain without accounting for any density stratification in the water body. It is observed that the acceleration zone upstream of the curtain can be affected by sink opening size, its location and water depth. The effect of boundaries on flow upstream of a line sink and the interaction of multiple sinks were analyzed. The effect of stratification on a line sink is also analyzed. A theory is developed to predict the incipient withdrawal condition when a sink is located on the horizontal bottom. The theory is also extended to a tilted bottom. The effect of boundaries on the incipient withdrawal condition is analyzed. When only one layer is being withdrawn, it is shown that a homogenous equation can be applied to a stratified condition by assuming an upper layer boundary at the interface. In addition to these works, a despike algorithm for ADV data is developed, and a numerical analysis on central difference scheme is presented.

ACKNOWLEDGEMENTS

I would like to thank my supervisor Dr. David Zhu for his superb supervision. I am grateful to the University of Alberta, Alberta Ingenuity Fund and NSERC to finance my research in different periods. I am also thankful to Mr. Perry Fedun for providing technical support. I am thankful to anonymous reviewers and thesis examiners to provide valuable comments.

Above all, I am thankful to the Almighty Allah to make everything possible.

TABLE OF CONTENTS

LIST OF TABLES

LIST OF FIGURES

NOTATIONS

A_o	cross-sectional area of the orifice
a	size of the intake opening
b	jet half width, distance of the line sink from the bottom
b_c	distance of the intake centerline from the bottom
b_{in}	size of the inlet opening
c	velocity decay coefficient
D	molecular diffusivity
D_x	diffusion coefficient in the x direction
D_y	diffusion coefficient in the y direction
d	diameter of the orifice, size of the intake opening
g	acceleration due to gravity
F	incipient Froude no for the line sink
F_{in}	inlet Froude no ($= u_{in}/\sqrt{g b_{in}}$)
F_l	incipient Froude no for the line sink
F_p	incipient Froude no for the point sink
H	water depth
h	water depth, vertical distance between the interface and the intake
h_i	incipient water depth
h'	vertical distance from the interface to the sink level.
h_x	band width in x direction
h_y	band width in y direction
I	turbulent intensity
k	turbulent kinetic energy
k_{in}	turbulent kinetic energy at the inlet
L	length of the basin
l_h	horizontal dimension of the rectangular orifice
l_v	vertical dimension of the rectangular orifice
M	momentum flux
M_{in}	momentum flux at inlet
M_∞	momentum flux at infinity
N	number of samples
P	cell-Peclet number, pressure integral

P_k	production of the turbulence
p	Pressure
Q	flow rate
q	flow rate per unit width
q_i	incipient flow rate per unit width
R_{in}	inlet Reynolds number (= $u_{in}b_{in}/\nu$)
r	radial distance
r_a	volume fraction of phase a
r_b	volume fraction of phase b
S	jet spreading rate
S_u	Submergence
U	velocity along streamwise direction
U_c	centerline velocity
U_{max}	maximum velocity at a section
U_s	velocity at the line sink
U_∞	velocity at far upstream of the intake
u	streamwise velocity
u_{in}	velocity at the inlet
u_m	maximum u-velocity at a section
$u*$	friction velocity
V	velocity along vertical direction
V_c	center line velocity of orifice
V_o	average velocity of an orifice
v	velocity along vertical direction
W	width of the basin
w	velocity along vertical direction
x	streamwise direction
x_a	extent of the acceleration zone
y	vertical direction
y_b	end depth
y_c	critical depth
y_s	cusp height
y_2	sequent depth

z	transverse direction
α	interior angle
α_a	volume fraction of air
α_w	volume fraction of water
Δu	gradient of *u* velocity
Δy	distance of the first grid point from the wall
$\Delta \rho$	density gradient
θ	rotation angle of principal axes
κ	von-Karman constant
ε	dissipation rate
ε_{in}	dissipation rate at the inlet
μ_a	molecular viscosity of air, molecular viscosity of phase *a*
μ_b	molecular viscosity of phase *b*
μ_t	eddy viscosity
μ_w	molecular viscosity of water
v	kinematic viscosity
ρ	density of fluid
ρ_a	density of air, density of phase *a*
ρ_b	density of phase *b*
ρ_w	density of water
τ_w	wall shear stress

Chapter 1

Introduction

Flow upstream of a hydropower dam is accelerated by the operation of intake units. This accelerated flow-field can attract resident fish towards the intake which might cause fish mortality (FERC, 2005). In order to protect fish from entrainment, fish repulsion systems, (e.g., strobe light, sounding devices, nets) are often used (RL&L, 2000; NPP 2005). To ensure the efficiency of fish repulsion systems, obtaining accurate near intake flow-fields and identifying the acceleration zone is necessary. For migratory fishes, fish passages and surface bypass systems were installed in several dams located in the Columbia River basin (Khan et al., 2004). Understanding the near intake flow-field is also important for efficient operation of these systems. Hydropower intake systems can be modeled as multiple orifices and potential flow theory can be applied to get the near intake flow field. The first objective of this study is to assess the capability of potential flow models (PFM) in predicting the flow upstream of hydropower intakes. This objective will focus on studying available literature on flow upstream of hydropower intakes.

For high head dams, flow upstream of the dam can be stratified due to temperature variations throughout the depth (Fischer et al., 1979). This stratification can affect the withdrawal characteristics and downstream river water temperature, which in turn can affect the river habitat. Withdrawal of warm surface water increased the downstream river temperature by 5-7^{o}C in California which was identified as a problem to the survival of salmon fry (Vermeyen, 2000). On the other hand, selectively withdrawing cold water was identified as a problem to the bull trout fish in Montana (Kubitschek et al., 1997). To maintain the downstream river temperature, a flexible curtain upstream of the intake was installed on the Whiskeytown and the Lewiston reservoir located in California (Johnson and Vermeyen, 1993), which is known as a temperature control curtain. A steel shutter frame structure was installed in the Shasta reservoir and the Hungry Horse reservoir, which is known as a temperature control device (Vermeyen, 1998; Kubitschek et al., 1997). These structures, especially curtains, can significantly affect the near-intake flow field. An experimental study of this flow-field was carried out by Shammaa et al. (2009) without considering stratification and by Shammaa and Zhu (2010) considering stratification. As this study was carried out for only a specific flow rate and basin geometry, further study is needed to get a comprehensive idea on how a curtain affects the flow field. Downstream of the curtain, the flow-field turns into a wall jet with a recirculation zone on top (Shammaa et al., 2009). At the inlet, the Froude number greater than 1. This flow field is a submerged jump, on which substantial amount of literature is available. However, not enough information is available at low

Froude numbers. In submerged jump studies, there are a number of issues for which further research is justified. For example, Wu and Rajaratnam (1995) found that velocity profiles in a submerged jump may show wall jet like or free jump like behavior at similar submergence ratios, though the reason was not adequately identified. Ead and Rajaratnam (2002)'s study shows that momentum flux is not preserved after some distance, and thereafter wall jet behavior is lost. The reason for this phenomenon was also not well understood. The effect of reducing the length scale on the jet region is another issue which is not explored yet. This study will carry out investigations at different water depths, length scales and with varying inlet Froude numbers to get a comprehensive knowledge on the near intake flow-field. This is the second objective of this study.

Flow upstream of the curtain can be modeled as a two dimensional sink. Increased velocity causes by the two-dimensional sink can also be a critical issue from the fish entrainment point of view. For a two dimensional intake, Shammaa et al. (2009) observed that the flow acceleration zone is limited within 1.5*h*, where *h* is the water depth. However, the effect of intake location and its size is not analyzed yet, and no theoretical justification is available in predicting the acceleration zone. This study developed a Schwarz-Christoffel (S-C) transformation based method to get the flow-field upstream of the two dimensional intake at variable locations and different sizes and computed the acceleration zone. The effect of intake location, and size on acceleration zone was analyzed. Interaction of multiple sinks is also an area that was focused on.

When the flow is stratified upstream of the curtain, either one layer, or both layers can be aspirated. For a two-dimensional line sink, Craya (1949) defined a criterion to distinguish the two,

$$F_l = \frac{q}{\sqrt{g\frac{\Delta\rho}{\rho}h'^3}}$$

Equation 1.1

where, F_l is the densimetric Froude number for the line sink, h' is the vertical distance from the sink level to the interface level, $\Delta\rho$ is the density difference between the two layers, ρ is the reference density, q is the discharge per unit width. According to Craya (1949)'s ideal fluid theory, both layers will be aspirated when $F_l > 1.72$. This criterion is valid for a reservoir of infinite depth. Jirka (1979) theoretically computed the critical Froude number for a skimmer wall problem. However, no theoretical model is available when the sink is located on a horizontal bottom, which is typical for a curtain. Predicting and analyzing the velocity field when one layer withdraws or both layers withdraw is an interesting area to explore. This study focused on developing a theoretical model to determine incipient withdrawal criteria when a sink is located at the horizontal bottom and assessed to what extent the unstratified equation can be applied in a stratified environment. This is the fourth objective of the study.

The numerical data was extensively verified by experiments for objective two. Experimental data was taken with a four beam ADV having 200 Hz sampling frequency. In the wall jet region, due to excessive turbulence, spike concentration is found to be significantly high, where a standard despiking algorithm, (e.g. Goring and Nikora 2002,Wahl 2003, Cea et al. 2007) is found to be less efficient. The despiking methods of Goring and Nikora (2002) and Cea et al. (2007) are primarily based on using a fixed threshold coefficient (for example, universal threshold) multiplied by the standard deviation or median absolute deviation to detect outliers/spikes. A threshold coefficient is determined for data with a small volume of spikes is found inefficient for data with a large volume of spikes, and vice versa. This study develops a method using kernel density function to isolate the data cluster from the spike clusters. This work is presented in Appendix A.

Advection schemes are potential sources of error in a numerical solver. The central difference scheme causes oscillation in advection dominated flows, while the upwind scheme is diffusive (Versteeg and Malalasekera, 2007). This study conducted theoretical analysis on minimizing the error associated with the advection scheme for a one dimensional problem. This work is presented in Appendix B.

This study has six chapters. The objective of each chapter is:

1. Chapter 2 assesses the feasibility of applying potential flow theories to identify the acceleration zone of hydropower intakes.
2. Chapter 3 investigates the flow downstream of a temperature control curtain.
3. Chapter 4 investigates the unstratified flow upstream of a curtain.
4. Chapters 5 investigates the stratified flow upstream of a curtain.

Besides these four objectives, a despike algorithm is developed and is presented in Appendix A. A numerical analysis on central difference scheme is presented in Appendix B.

References

Cea, L., Puertas, J., and Pena, L., (2007), Velocity measurements on highly turbulent free surface flow using ADV, Experiment in Fluids., 42, 333-348.

Craya, A., (1949), Theoretical research on the flow of nonhomogenous fluids, La Houille Blanche, 4, 44-55.

Ead, S.A., and Rajaratnam, N., (2002), Plane turbulent wall jets in shallow tailwater, Journal of Engineering Mechanics, ASCE.

FERC (2005), Fish entrainment and turbine survival evaluation for Tillery and Blewett falls developments, FERC no 2206, Progress Energy.

Fischer, H.B., List, E.J., Imberger, J., Koh, R.C.Y., Brooks, N.H., (1979), Mixing in Inland and Coastal Waters, Academic Press, NY.

Goring, D.G., and Nikora, V.I., (2002), Despiking acoustic Doppler velocimeter data, Journal of Hydraulic Engineering, 128(1), 117-126.

Jirka, G.H., (1979), Supercritical withdrawal from two layered fluid systems, Part-1, two dimensional skimmer wall, Journal of Hydraulic Research, 17(1), 43-51.

Johnson, P.L., and Vermeyen, T.B., (1993), A flexible curtain structure for control of vertical reservoir mixing generated by plunging inflows, Proc., Conference on Hydraulic Engineering, ASCE, 2377-2382, California.

Khan, L.A., Wicklein, E.A., Rashid, M., Ebner, L.L., and Richards, N.A., (2004), Computational fluid dynamics modeling of turbine intake hydraulics at a hydropower plant, Journal of Hydraulic Research, 42(1), 61-69.

Kubitschek, J., Sund, R., and Christensen, R., (1997), Selective withdrawal at Hungry Horse dam, Montana, Proc. Waterpower 97, 421-430.

NPP (2005), Fish Entrainment and Mortality Study, Vol 1, Niagra Power Project, New York Power.

RL&L, (2000), Resident fish entrainment: information review, RL&L Environmental Services Ltd, Edmonton, AB.

Shammaa, Y. and Zhu, D.Z., (2010), Selective withdrawal in two layer fluids using a temperature control curtain, Journal of Hydraulic Engineering, 136(4), 236-244.

Shammaa, Y., Zhu, D.Z., and Rajaratnam, N., (2009), Flow field in a rectangular basin with a line inlet and a circular outlet, J. Hydraul. Engng., ASCE, 135(10), 857-864.

Vermeyen, T.B., (2000), Application of flexible curtains to control mixing and enable selective withdrawal in reservoirs, Proc. 5th International Symposium on Stratified Flows, 457-462, Vancouver.

Vermeyen, T.B., (1998), First year selective withdrawal performance of the Shasta dam temperature control device, Proc., Water Resources Engineering 98, 944-949.

Versteeg H.K., Malalasekera W., (2007), An Introduction to Computational Fluid

Dynamics: The Finite Volume Method, Pearson-Prentice Hall, 132.

Wahl, T.L.,(2003), Discussion of “Despiking acoustic Doppler velocimeter data” by Derek G. Goring and Vladimir I. Nikora, Journal of Hydraulic Engineering, 484-489.

Wu, S., and Rajaratnam, N., (1995), Free jumps, submerged jumps, and wall jets, Journal of Hydraulic Research, 33(2), 197-212.

Chapter 2

A Review on Flow Upstream of Hydropower Intakes[1]

2.1 Background

This study reviewed the flow-field upstream of several hydropower dams from published literature and assessed the feasibility of applying potential flow models (Shammaa et al., 2005; Bryant et al., 2008) in the case of a real hydropower dam to generate the near intake flow field. Understanding the flow-field upstream of a hydropower dam can have wider applications including fish passage and fish repulsion system design. The necessity of retrofitting fish passages was felt rigorously for hydropower dams located on the Columbia River to protect Pacific

---

[1] A version of this chapter has been submitted for publication to the Canadian Journal of Water Resources.

salmonids, which was listed as an endangered species, primarily due to the dam operations in the river (Khan et al. 2004; Christman, 1997; Mih, 1991). Downstream migration was felt as a serious problem in other basins as well, for example, in the Mokau River located in New Zealand for silver eels (Boubee and Williams, 2006). On the other hand, fish repulsion systems were designed to avoid resident fish entrainment. Fish passage systems may include fish screens and surface bypass facilities and fish repulsion systems may include behavioral barriers such as, strobe lights, electric fields, bubble curtains, etc. to repel fish away from the intake (NPP, 2005). Figure 2.1 shows qualitatively fish screens, gate wells, vertical barrier screens, a collection channel, turbines, and the tail race of the Bonneville second power house facility (Mih, 1987).

Understanding flow fields upstream of the intake is necessary to design a safe and improved fish passage system. For example, fish screens can also be responsible for fish injury if the impingement velocity (i.e. water velocity perpendicular to the screen) is greater than 0.8 m/s (Mih, 1991). To design a surface bypass system, one needs to assess the surface flow-field, as there should be sufficient attraction flow to ensure its proper performance (Odeh and Orvis, 1997). To place the behavioral barrier in order to avoid resident fish entrainment, one needs to identify the acceleration region, on where fish might not be able to escape entrainment if its burst speed and swimming speed is not sufficient.

This review work is divided into five sections. In Section 2, flow upstream of an orifice is reviewed under ideal channel geometry and intake conditions which include theoretical, experimental and numerical works. In Section 3, fore-bay flow-fields of several hydropower dams are reviewed, which includes field measurements, physical models and CFD studies. These studies may help to understand how local bathymetry, channel and intake geometry, and orientation of intake bays can affect the flow field upstream of the intake and the feasibility of applying potential flow models in real hydropower dams. In Section 4, the effect of stratification and vortices are discussed. Finally, some concluding remarks are provided.

2.2 Hydraulics of Orifices under Ideal Conditions

If a hydropower intake is idealized as an orifice or sink, theoretical, experimental and numerical studies available in the literature for predicting flow upstream of an orifice and sink, which can be applied to assess the forebay flow-field. Shammaa et al. (2005) applied potential flow theory to assess the flow upstream of an orifice considering the free-surface and channel bottom. In this approach, the finite-size orifice is assumed as an integration of point sinks, where the flow-rate through each sink is computed by dividing the flow-rate through the orifice by its cross-sectional area. This implicitly assumes a uniform velocity at each point of the orifice. Hence, the velocity at a particular point upstream of the orifice is the algebraic summation of the flow induced by each point sink. The velocity potential for such an orifice is computed as,

$$\varphi(r,\theta) = \frac{-2Q}{\pi^2 d^2} \int_0^{2\pi} \int_0^{d/2} \frac{r_0 dr_0 d\theta_0}{\left(r^2 + r_0^2 - 2rr_0 \cos\theta \cos\theta_0\right)^{1/2}}$$

Equation 2.1

where, Q is the flow-rate through the orifice, d is the diameter of the orifice, (r, θ) is the polar coordinates of a point upstream of the orifice located at the plane-of-symmetry, and (r_0, θ_0) is the coordinate of a point sink constituting the orifice located on the plane of orifice. The plane of orifice is perpendicular to the plane of symmetry.

Shammaa et al. (2005) solved the integration numerically and computed the velocity components. The expression for computing the centerline velocity, V_c, is derived as,

$$\frac{V_c}{V_0} = 1 - \left(1 + \frac{d^2}{4x^2}\right)^{-1/2}$$

Equation 2.2

where, V_0 is the average velocity at the orifice, based on the flow-rate and the cross-sectional area of the orifice (A_0) and x is the longitudinal distance from the orifice.

For a rectangular orifice, the velocity potential is computed as,

$$\varphi(x, y, z) = \frac{-V_0}{\pi} \int_{-\frac{l_v}{2}}^{\frac{l_v}{2}} \int_{-\frac{lh}{2}}^{\frac{lh}{2}} \frac{dz_0 dy_0}{[x^2 + (z - z_o)^2 + (y - y_o)^2]^{1/2}}$$

Equation 2.3

where, l_h and l_v is the horizontal and vertical dimensions of the rectangular orifice respectively,(x,y,z) is the longitudinal, vertical and transverse coordinates, respectively, of a point upstream of the orifice with an origin located at the centroid of the orifice, and (z_o, y_o) is the Cartesian coordinate of a point sink constituting the orifice located on the plane of orifice.

To consider the effect of finite depth, Shammaa et al. (2005) added an image orifice. To get velocities at a point in finite depth, the velocity obtained from image orifices should have to be added to the velocity obtained from a real orifice. To determine side-wall effects, another set of image orifices should be added in the transverse direction.

Bryant et al. (2008) applied Shammaa et al. (2005)'s procedure to multiple orifices by adding the flow-field induced by each single orifice. This superposition of flow-fields predicted the velocity field very close to the experimental results. In the case of a large orifice, velocity along the orifice can increase with depth due to the increase in pressure with depth. Including this effect, Bryant et al. (2008) computed the velocity potential for a circular orifice in the Cartesian coordinate system as follows,

$$\varphi(x, y, z) = \frac{-2Q}{\pi^2 d^2} \int_0^{2\pi} \int_0^{\frac{d}{2}} \frac{\sqrt{(1 - r_o \cos\theta_o / h_o)}\, r_0 dr_0 d\theta_0}{[x^2 + (y - r_o \cos\theta_0)^2 + (z - r_o \sin\theta_0)^2]^{1/2}}$$

Equation 2.4

where, z is the Cartesian axis in the transverse direction. This correction is applicable only when the pressure downstream of the orifice is atmospheric. In a hydropower dam, if water is discharged into the tail-race through a conduit that is submerged in the tail-race, the pressure difference should not vary across the conduit depth and this correction may not be applicable.

In order to get velocity components (V_x,V_y,V_z) from the velocity potential, one needs to differentiate Equation 2.3 with respect to *x, y* and *z,* respectively. These components and the radial velocity (V_r) are as follows,

$$V_x(x,y,z) = \frac{V_0}{2\pi} \int_{-\frac{l_v}{2}}^{\frac{l_v}{2}} \int_{-\frac{lh}{2}}^{\frac{lh}{2}} \frac{x dy_0 dz_0}{[x^2 + (y-y_o)^2 + (z-z_o)^2]^{3/2}}$$

$$V_y(x,y,z) = \frac{V_0}{2\pi} \int_{-\frac{l_v}{2}}^{\frac{l_v}{2}} \int_{-\frac{lh}{2}}^{\frac{lh}{2}} \frac{(y-y_o) dy_0 dz_0}{[x^2 + (y-y_o)^2 + (z-z_o)^2]^{3/2}}$$

$$V_z(x,y,z) = \frac{V_0}{2\pi} \int_{-\frac{l_v}{2}}^{\frac{l_v}{2}} \int_{-\frac{lh}{2}}^{\frac{lh}{2}} \frac{(z-z_o) dy_0 dz_0}{[x^2 + (y-y_o)^2 + (z-z_o)^2]^{3/2}}$$

$$V_r = \sqrt{V_x^2 + V_y^2 + V_z^2}$$

Equation 2.5

For a point sink in a half-space, radial velocities ($V_{r,s}$) can be computed as follows,

$$V_{r,s} = \frac{Q}{2\pi r^2}$$

Equation 2.6

This study generated flow upstream of the Dworshak dam, located in Idaho, USA, using Equation 2.5. Figure 2.2 shows radial velocities upstream of the dam when a single intake is in operation. This figure shows that radial velocity contours are hemi-spherical upstream of the intake in both the *x-y* and *x-z* plane. Very close to the intake, contours are hemi-elliptical. Figure 2.3 shows velocity contours upstream of the center intake, when three intakes are in operation. The contours were tapered laterally due to the influence of the other intakes. All the flow features matched very well with the CFD simulation carried out by Cook and Richmond (2004). Hence, potential flow models (PFM) can be considered as a reliable tool to generate the near-intake flow-field upstream of a dam head-wall.

Applying Equation 2.1 and Equation 2.6, this study evaluated the effect of (i) finite depth (with infinite width), and (ii) the orifice size, and These effects are shown in Figure 2.4. The effect of a free surface and a boundary were accounted for by adding image orifices. This figure shows that water depth has no significant effect when $h_o > 3d$. Beyond that limit, the solution merges with the infinite depth solution. The stream-wise velocity is found asymptotic to zero in all cases. In the case of infinite depth $V_c \approx 0.01V_o$ at about $x = 3.5d$. When $h_o = d, V_c \approx 0.035V_o$ at about $x = 3.5d$ and $V_c \approx 0.01V_o$ at about $x = 10d$.

The point-sink solution (Equation 2.6) has notable differences from the orifice solution (Equation 2.1) at $x < 3.5d$. Beyond that limit, these are almost equal. For example, at $x = d$, the orifice solution is 180% greater than the point-sink solution. This gives emphasis to the importance in using an orifice solution instead of a sink-solution in the case of an orifice. Again, the sink solution is singular at origin, which is not the case for the orifice solution.

The extent of the acceleration region is an important quantity for design purposes. The centerline velocity typically reduces sharply close to the intake, and thereafter it becomes asymptotic towards the mean velocity of the approach channel. Hence, one needs to define a threshold to estimate the extent of the acceleration region, because theoretically it can extend to infinity. In this study, the extent of the acceleration region was defined as a distance x_a, where the difference between the centerline velocity and the velocity at infinity is 1% of the difference between the orifice velocity and the velocity at infinity. Mathematically, $\frac{(V_{c,a} - V_{\infty})}{(V_o - V_{\infty})} \approx 1\%$ where, $V_{c,a}$ is the center-line velocity at a distance x_a, and V_{∞} is the centerline velocity at infinity. For reservoirs having infinite depth or width, $V_{\infty} \approx 0$, and for reservoirs with finite depth and width, V_{∞} should be equal to Q/A, where A is the cross-sectional area of the channel. In such case, the acceleration region can be shortened.

Anayiotos et al. (1995)'s experimental and numerical work showed that at a distance equal to 1.5*d*, the centerline velocity is equal to 5% of the average velocity at orifice (V_o). The theoretical work of Shammaa et al. (2005) also supported this. Hence, numerical, experimental, and theoretical works showed that within $1.5d$, the centerline velocity is less than $0.05V_o$.

It is of interest to know how the size of the orifice will affect the flow upstream. Shammaa et al. (2005) compared the orifice solution with a single point sink solution and found that both approaches predicted the same velocity field at a distance 1.5*d* upstream of the orifice or point sink. The iso-velocity surfaces are hemi-spherical downstream of this point for both the orifice and sink solution. Upstream of this point, the iso-velocity surfaces tend to be hemi-elliptical in the case of an orifice solution, and remain hemi-spherical in the case of a sink solution. Hence, it can be concluded that the size of the orifice does not affect the flow at a distance greater than 1.5*d* upstream of the orifice. This theoretical outcome complies with the experimental and numerical investigation of Anayiotos et al. (1995) and numerical investigation of Rodriguez et al. (1992), who also found that iso-velocity surfaces are nearly hemi-spherical at a distance greater than 2*d* upstream of the orifice.

The intake of a hydropower dam is typically contoured to minimize head loss. A sharp-edged intake can have a loss coefficient in the order of 0.5 to 0.6, whereas a contoured intake can have a loss coefficient as low as 0.05 (Murray, 1993). Minimizing head-loss is more important for low-head hydropower dams (Cotroneo and O'Dea, 1984). Hence, an assessment is needed to quantify to what extent the flow-field estimated from a sharp-edged orifice can account for the flow-field upstream of a contoured orifice. Radius of contraction of intake structures of Shasta dam located in California (Vermeyen, 1998), and Hungry Horse dam located in Montana (Kubitschek, 1997), etc. is negligible compared to the pipe diameter. Hence, intake of these dams is closer to the sharp-edged orifice.

Marghzar et al. (2003) carried out a turbulence study as well as a numerical simulation on the flow upstream of a rectangular orifice at low submergence. His study showed that $V_c \leq 0.05V_o$, within 1.5*d* from the orifice, which is consistent with findings reported above. The maximum vertical velocity occurs from $0.2d \leq x \leq 0.4d$ upstream of the orifice along the plane of symmetry and at $y = \pm 0.5d$. Maximum transverse velocity is located at x = 0.2d and at $z = \pm d$.Turbulence measurements with a Laser Doppler Velocimeter (LDV) showed a general trend of having higher intensity at the locations where there is strong curvature in streamlines.

2.3 Hydraulics of Hydropower Intakes

Although hydropower layouts can vary over a wide range, it can be expected that the PFM based prediction is applicable as long as the intake units are reasonably perpendicular to the approach channel. This property is desirable in most hydropower dams and for these dams potential flow models can be used when a faster solution is required. Some studies field-scale studies are discussed hereafter.

Vermeyen (2002) measured velocities at 3.33*d* upstream of a municipal and industrial intake located on the Folsom dam. Although a hydropower intake unit was in operation close to the municipal intake during measurement, it was observed that the horizontal velocity at the intake level was only 2.7% of the average velocity at the municipal intake. The field-scale CFD study of the orifice-like spill structure of the Dworshak dam showed that the centerline velocity is 5% of the average velocity at the orifice at a distance of 1.75*d* (Cook and Richmond, 2004). This is consistent with the experimental and numerical findings of Anayiotos et al. (1995) and theoretical work of Shammaa et al. (2005) which showed that centerline velocity is less than 5% of the average intake velocity at a distance greater than 1.5*d*. It appears that lab-scale and theoretical predictions correspond well to the field-scale flow scenarios.

The interference of multiple orifices is another point of interest. There are three orifices like spills are available on the Dworshak dam with a distance between each outlet of approximately 3.5*d*. Despite this configuration, the iso-velocity surfaces of each orifice still remain hemispherical and the acceleration region is confined to 3.5*d*. Hence, interference can be negligible if orifices are located at a distance greater than 3.5*d*. Figure 2.3 shows the radial velocity contours when three intakes are in operation.

It was previously discussed that the intake on a dam is generally contoured to minimize head loss. The radius of contraction can be significantly large compare to the water depth as shown in Figure 2.1. It is of interest to check how the upstream flow pattern for such an intake geometry is comparable to the PFM works. A CFD simulation of the flow pattern upstream of the Wanapum dam located on the Columbia River was carried out by Meselhe and Odgaard (1998). The intake of this dam has a large radius of contraction. The CFD model solved the three-dimensional Reynolds Averaged Navier Stokes (RANS) equations with a $k-\varepsilon$ turbulence model using a curvilinear coordinate system in a finite-difference frame-work. The free-surface was modeled as a rigid lid with a symmetric boundary condition. The CFD model was validated with a 1:16 undistorted scale model and thereafter was used to predict the flow structure in the reservoir, including a surface bypass system on the existing dam system.

The structure of the Wanapum dam is essentially the same as shown in Figure 2.1, with one notable difference, the upstream wall is truly vertical. The authors' works showed that the velocity profile immediately upstream of the intake is skewed towards the channel bottom, that is, the velocity closer to the intake floor is approximately two times higher than that of the intake ceiling. The intake geometry should be responsible for this velocity skewness. As the intake ceiling is gradually lowered and the bottom is kept nearly horizontal, maximum velocity should be observed closer to the channel bottom. The potential flow models should not be able to predict such geometry-induced skewness.

It is of interest to assess Equation 2.2 on predicting the acceleration region under such geometry. Due to the skewness of the velocity at the intake head-wall, V_o is chosen as the average velocity. Using Equation 2.2, the maximum velocity at a distance equal to 0.24*d* upstream of the intake head wall is computed as $0.57V_o$, similarly, the CFD result reported by Meselhe and Odgaard (1998) showed that the average velocity at this section was $0.57V_o$. At a distance of $x = 0.94d$, the observed velocity profile was almost uniform, which implies that the acceleration region is confined to a distance equal to *d* due to the finite water depth. Hence, the rule of thumb (i.e., the acceleration region is confined within 3.5*d*) is applicable for this geometry and the theoretical works can yield a reasonably accurate flow-field if a non-uniform skewed velocity is assigned at the orifice outlet.

There are a few dams where powerhouse units were constructed parallel to the approach channel. For example, at Rocky Reach dam, and Dalles dam located on the Columbia River basin (Birch and Lemon, 1993). For these dams, flow enters the intake bays obliquely and theoretical works may not be able to predict the flow-field. Studies related to the flow pattern of these dams are discussed below.

Rocky Reach dam’s spillway is located close to the left bank and is perpendicular to the main flow direction, while the intake units are parallel to the direction of flow and thus creates an ‘L’ shaped layout. A wall perpendicular to the flow direction was constructed connecting the downstream end of the intake units and the right bank of the river to retain water. Field measurements using an Acoustic Doppler Current Profiler(ADCP) showed that flow near the intake increases in magnitude and rotates counterclockwise with depth, thus becoming more axial to the intake face (Birch and Lemon, 1993). A 1:30 scale physical model (Sweeney et al. 1997) and a CFD study (Lai et al.,2003) showed that water enters the intake units obliquely and a recirculation zone was created between the intake bays and the right bank on the downstream side of the dam. It was observed that the majority of fish population used the intake units located on the downstream side of the dam facility for their downstream migration as a last resort (Sweeney et al., 1995) and a surface bypass system was constructed on that side to assist migration (Christman et al., 1997).

At Dalles dam, the powerhouse is also parallel to the main flow direction (Khan et al., 2002); the difference from Rocky Reach dam is that spillways connect the right bank to the downstream end of the powerhouse. A surface recirculation eddy was observed at the Dalles dam; the size of the eddy was affected by the amount of spillage. This issue was investigated by Khan et al. (2002) using a CFD model. The study showed that at no-spill conditions, a large recirculation zone developed at the upstream side of the spillways, whereas, with increasing spill rate, the size of this recirculation zone gradually reduced. It is easily perceivable that the theoretical works would not be applicable in these situations.

Although PFM can estimate flow fields at an infinite distance upstream of the intake, the orifice induced acceleration zone is confined within 10*d* at shallow depths. Beyond that limit, the velocity can be estimated using the Q/A relationship. However, irregularities in channel alignment and river bathymetry can impose complexity in velocity estimations. For example, Meselhe et al. (2000) simulated a 7 km reach of the Columbia River upstream of Wanapum Dam, which showed that the upstream reach is meandering with bar and pool formations and triangular in cross-section. In the forebay area of Dalles dam, a hundred meter deep pool was observed (Johnson et al., 2006). The potential effect of such a pool cannot be predicted with PFM theories. Wicklein et al. (2002) carried out CFD studies of Howard Hanson dam located in Washington state. The simulated flow-field showed strong curvature upstream of the intake associated with large recirculation eddies. These flow structures cannot be predicted by the potential flow models.

A hydropower facility may be operated under full load or split load conditions. A full load condition means that all the intake units are in operation and a split load condition means that only a few of the intake units are in operation. Flow patterns produced by these two conditions were investigated by Rakowski et al. (2002) using a CFD model for the Bonneville powerhouse. It was observed that under a full-load condition the flow upstream of the intake bays can be idealized as a single orifice with a large aspect ratio, whereas under a split load, the flow can be idealized as multiple orifices. Applying the idea of multiple orifices, PFMs should be able to predict flow-field at both full-load and split load conditions.

The surface bypass system experiments conducted by Meselhe and Odgaard (1998) and Meselhe et al. (1996) consisted of installing vertical slots on the upstream side of the dam and partially blocking the existing intake. By installing a vertical structure, fish had to choose the slots constructed close to the surface for their downstream migration. The vertical slots are connected to a collection channel. It may be possible that the surface bypass system and intake units can be modeled as multiple orifices as long as these facilities are perpendicular to the main flow channel. The CFD study showed that this partial blockage of intakes lowered the acceleration region towards the bottom, which is expected. However, partially blocking the intake with sharp-edged barriers can increase head loss, and will create flow separation close to the ceiling, which in turn can cause unsteady vortex shedding in the free shear layer. As a remedy for this, the barrier-edge could extend inside the intake with a curved streamlined shape.

Khan et al. (2004) used a CFD model and a 1:25 scale physical model to design a surface attraction facility for Dalles dam located on the Columbia River basin. A partial blockage of the intake was done using a ‘J’ shaped structure instead of a vertical slot as used by Meselhe and Odgaard (1998). The objective of constructing this trash rack was to establish a quiescent zone on the upper portion of the intake which could compel fish to move to the surface bypass intake rather than proceeding to the hydro-intake. The effect of such an extrusion cannot be modeled with theoretical works. The CFD result showed that although a dead-zone was established upstream of the ‘J’ shaped structure, inside the intake, it created a flow-separation and large three-dimensional eddies close to the intake ceiling. The authors estimated that these eddies will reduce the turbine efficiency by about 4.8%.

2.4 Stratification and Other Issues

Stratification is an issue that was ignored in most hydraulic studies of the fore-bay. In summer, the fore-bay of a hydropower dam can be thermally stratified with the warm surface water layer (epilimnion) resting on the cold deeper layer (hypolimnion) (Brooks and Koh, 1969). In a thermally stratified reservoir, a penstock intake located at a particular elevation tends to withdraw water from that level only, a behavior which is known as selective withdrawal. Hence, the thermal stratification can significantly affect the flow upstream of an intake and the degree of impact will primarily depend on the density gradient of the fore-bay and flow rate through the intake. For discrete two-layer stratification, to determine whether one layer or both layers will be aspirated, Craya (1949) introduced a Froude number which can be defined as,

$$F_l = \frac{q}{\sqrt{g\frac{\Delta\rho}{\rho}h'^3}}$$

$$F_p = \frac{q}{\sqrt{g \frac{\Delta\rho}{\rho} h'^5}}$$

Equation 2.7

where, F_l and F_p are the Froude numbers for the line sink and the point sink, respectively, h' is the vertical distance from the sink`s centroid to the interface level, $\Delta\rho$ is the density difference between the two layers, ρ is the reference density, q is the discharge per unit width and Q is the total discharge through the sink. Craya (1949) computed F_l = 1.72, and F_p =2.55 as the lower limits for which only one layer will be aspirated. Figure 2.5 demonstrates the two cases. In the first case, only the lower layer is flowing, while in the second case, both layers are flowing. Withdrawal from both layers can be achieved by increasing Q (or q). It can also be achieved by reducing h' or $\Delta\rho$ or both.

If only the layer adjacent to the intake is aspirated, a two-layer stratified reservoir can be assumed to be an unstratified reservoir, having a water depth equal to the depth of the aspirated layer. Under this assumption, the theoretical work of Shammaa et al. (2005) for finite water depth can be applied to the aspirated layer. If both layers are aspirated, theoretical works can still be applicable with reasonable accuracy. For example, Shammaa and Zhu (2010) carried out experimental works of withdrawal from a stratified reservoir, which showed that potential flow theory works reasonably well when both layers as well as one layer are aspirated.

For a linear density profile and line sink, the theoretical works of Koh

(1966) showed that water will be withdrawn from a layer of finite thickness, known as the withdrawal layer. The thickness of the withdrawal layer will increase with distance from the sink following the equation,

$$\delta = \frac{7.14x^{1/3}}{\left(\frac{\varepsilon g}{D\nu}\right)^{1/6}}$$

Equation 2.8

where, δ is the withdrawal layer thickness, D is the molecular diffusivity, ν is the molecular viscosity, and $\varepsilon = -\frac{1}{\rho_o}\frac{d\rho}{dy}$ in which ρ_o is the density at the sink, and ρ is the ambient density. The formation of the withdrawal layer is subjected to the condition that the Froude number defined as,

$$F = \frac{q}{\sqrt{g\varepsilon h^4}}$$

Equation 2.9

exceeds $1/\pi$ (Yih, 1958). Here, q is the discharge per unit width, and h is the water depth.

The experimental works of Mahony and Pritchard (1981) for a line intake showed that withdrawal occurred only from a layer of finite thickness. The centerline velocity is 5% of the average intake velocity within $50a$, where a is the width of the intake opening. Shammaa et al. (2005)'s theoretical work for flow upstream of a line intake showed that at a distance equal to 1.5h, flow is nearly uniform. Due to the different length scale from these two studies, it is not possible to check whether theoretical works are applicable in the withdrawal layer.

EPRI (1992)'s review work found that resident fish entrained at Klebler dam remain at an intermediate depth during the summer and the fall, while they are closer to the intake ceiling during the winter and spring. It can be hypothesized that the water in the intake is stratified in summer and fish prefer to remain closer to the intermediate depth or bottom to avoid warmer water. Hence, stratification can affect fish behavior. In another example, Ploskey and Carlson (1999)'s study showed a lower Fish Guidance Efficiency (FGE) in summer compare to the FGE in spring for an extended length screen installed in John Day dam located in the Columbia River, which can also be due to the effect of stratification. The stratification effect can be ignored for a head-pond of a low-head dam (or run-of-river hydro-projects) due to its shallower depth and vertical mixing due to the turbulence.

Thermal stratification of the forebay at McNary dam located on the Columbia River was reported by Haque et al. (2005). The field measurements at this forebay showed sharp decreases in temperature in the upper portion (4^{o}C within 28% of total water depth) and only 0.6^{o}C temperature variation throughout the remaining depth. If the warm epilimnion water is withdrawn through the intake, temperature at the gate-well and collection channel will increase and the authors hypothesized that this thermal shock can be harmful to the migrating salmonids. The authors developed a CFD model using a commercial package, FLUENT, in order to obtain a modification of the intake roof geometry which would impede the withdrawal of warm surface water. This model employed a finite-volume scheme with hybrid unstructured meshes to solve non-hydrostatic RANS equations using SIMPLE algorithm for pressure-velocity coupling. The stratification was incorporated by solving the transport equation for temperature, applying a turbulent Prandtl number equal to 0.85. The simulation showed that the stratification increases water temperatures in the gatewells and fish-bypass systems and the modification of the intake roof geometry has little effect on reducing the water temperatures inside the intake. This simulation did not show formation of a withdrawal layer, and hence, potential flow models should predict the flow field well. This study did not analyze how much the near-surface temperature of the forebay exceeded the average temperatures of the Columbia River prior to the construction of McNary dam. If the difference is insignificant, the temperature at the gate-well should be well-tolerated by the salmon species.

The formation of a withdrawal layer is more likely in high-head dam. A recirculation on the surface layer was observed by Khangaonkar et al. (2005) in the stratified forebay of the 134 m high Round Butte dam located in Oregon. As the intake is located close to the bottom, it selectively withdraws the colder hypolimnion water and a recirculation pattern develops on the upper part which results in backflow of the warm surface water. This implies that a withdrawal layer was formed, and one may apply the potential-flow-model in the withdrawal layer. The author applied numerical tools to their study, which applied a three dimensional hydrodynamic model coupled with a vertically integrated continuity equation to resolve the free-surface. A transport equation for temperature was incorporated and this transport equation accounts for heat exchange across the free surface.

Selective withdrawal of warm surface water along with other environmental factors increased downstream river temperatures by 5-7^{o}C in California which was identified as a problem for the survival of salmon fry (Vermeyen, 2000; Vermeyen, 1997). On the other hand, selectively withdrawing cold water was identified as a problem for the bull trout fish in Montana (Kubitschek et al., 1997). To maintain the downstream river temperature, a flexible curtain upstream of the intake was installed on the Whiskeytown and Lewiston reservoirs located in California (Johnson and Vermeyen, 1993; Vermeyen and Johnson, 1993), which is known as temperature control curtain (TCC). Steel shutter-frame structures were installed in the Shasta and the Hungry Horse reservoirs, which are known as temperature control devices (TCD) (Vermeyen, 1998; Kubitschek et al., 1997). These structures, especially curtains can significantly affect the near-intake flow field. An experimental study of this flow-field was carried out by Shammaa et al. (2009) without considering stratification and by Shammaa and Zhu (2010) considering stratification. The effect of these structures on downstream or upstream migrating fish has not been assessed yet. Although the potential-flow-models may predict the flow upstream of the curtain, it will not be able to predict the flow downstream of the curtain as the flow is dominated by a turbulent jet.

The headwalls of dams are often constructed incline rather than truly vertical. Anayiotos et al. (1995) and Anayiotos et al. (1998) carried out numerical investigations to assess the effect of the inclination on the acceleration region.

Anayiotos et al. (1998) described the inclination as negative if it makes a clockwise angle with the vertical (when flow moves from left to right) and positive for an anti-clockwise rotation. For example, the inclination of the Bonneville second power house headwall (Figure 2.1) is negative according to this definition. It was observed that for positive inclination, the acceleration region extends further upstream. For example, with an inclination angle of 63^o, the centerline velocity is 25% of the average orifice velocity at a point, whereas it is only 5% of the average orifice velocity when the inclination angle is 0^o (i.e., vertical wall) at the same point. On the other hand, when the angle of inclination is negative, it was observed that the acceleration region was shortened and this shortening was very insignificant. As the angle of inclination in the case of a dam headwall is very small, this inclination is not expected to have a significant effect on the velocity field.

Vortices at the intake drew much interest in the last decade and most works are based on the vertical intake. Intake vortices can initiate from the free-surface (i.e. free-surface vortex) or from the channel bottom, and side-walls (i.e. sub-surface vortex) (Rajendran and Patel, 2000). Free-surface vortices can entrain air (air-entraining vortex) or may not have sufficient strength to entrain air (Carriveau et al., 2002). It is reported that, intake vortices (air-entraining or non air-entraining) can cause vibrationa, damage to components (Ansar and Nakato, 2001), pump efficiency decreases (Rajendran and Patel, 2000), frazil ice deposition (Carriveau et al., 2002), sediment deposition (Tokyay and Constantinescu, 2006) and even affect the Fish Guidance Efficiency (FGE) of the fish-screen (Mih, 1991). There are no well-defined criteria available to predict the occurrence and nature of the vortices and one often needs to rely on scale modeling with dye tests and Particle Image Velocimetry to detect such vortices (Tokyay and Constantinescu, 2006). If scale modeling shows the existence of vortices, modification of the intake geometry is carried out in an effort to obtain a vortex free intake (Rajendran and patel, 2000). Asymmetry in the approach flow and geometry are considered responsible for such vortex formations. However, it can also happen in symmetric geometry under certain hydraulic conditions (ASCE, 1995). Recently, several CFD studies have been published applying a RANS based turbulence model as well as applying LES. They have reported being successful in capturing the free-surface as well as wall-attached vortices (Tokyay and Constantinescu, 2006). Occurrence of air-entraining vortices was reported at the intake of the Bonneville second power house facility, which was found to affect the FGE (Mih, 1991). Another occurrence of stable air-entraining vortices was reported in the intake of Sidney A. Murray Jr hydroelectric power plant located on the lower Mississippi River (Alam, 1989). The potential flow models are not able to predict the occurrence of air-entraining or subsurface vortices. One needs to depend on physical models and high-resolution CFD models for this issue.

2.5 Concluding Remarks

Very high velocities close to the intake can cause entrainment of fish and debris and therefore understanding the near-intake flow-field is important. Upstream of the orifice, the centerline velocity sharply reduces and retains the mean velocity of the channel (*Q*/*A*) within a distance of 3.5*d*. Field measurements, numerical simulations, experiments, and potential flow models developed by Shammaa et al. (2005) supported this hypothesis. This region, where velocity is accelerated by the influence of the orifice, is termed as the acceleration region.

It is found that a finite water depth (with infinite width) has no significant effect when the water depth is greater than 3*d*. In general, a finite water depth reduces the acceleration zone as the velocity at infinity is *Q*/*A*, instead of zero. The size of the orifice has a notable effect inside the acceleration region; outside the acceleration region, the predicted velocity is very similar to the sink solution. For multiple intakes located at a distance greater than 3.5*d*, the acceleration region is confined within 3.5*d*.

A practical problem is that if the intake is contoured with a large radius of contraction, the velocity field at the intake-face is found to be skewed, which is not possible to predict by the theoretical work of Shammaa et al. (2005). However, if the flow at the orifice is provided as skewed in the potential-flow-model, it should be able to predict the flow-field upstream of the head-wall with reasonable accuracy.

Shammaa et al. (2005)'s work may also be applicable to reservoirs having discrete and continuous stratification. If a distinct withdrawal layer is formed, one may apply the potential flow theory in the withdrawal layer. In such a case, true boundaries will have to be shifted to the withdrawal layer boundaries.

Applying the idea of multiple orifices developed by Bryant et al. (2008), it appears that a complex system of intake units, and fish slots can be modeled integrally if the head-wall is perpendicular to the approach channel. This integrated model may be recommended for design purposes as this approach will provide a solution faster than a CFD or physical model. The theoretical work will not be applicable for predicting flow inside the intake and turbine passage and the occurrence of vortices upstream of the intake.

Far upstream of the intake, PFMs are not applicable when cross-sections are irregular, non-uniform and the approach channel is curved. For nearly uniform cross-sections and straight reaches, flow velocities far upstream can be estimated using Q/A, and applying PFMs would be rather inefficient.

2.6 References

Alam, S., (1989), Hydraulic model studies of Sydney A. Murray Jr, hydroelectric plant, Proc. Waterpower 89, New York, 537-546.

Ansar, M., Nakato, T., (2001), Experimental study of 3D pump-intake flows with and without cross flows, J. of Hydraul. Engng, 127(10), 825-834.

Anayiotos, A.S., Fan, P., Perry, G.J., Myers, J., Elmahdi, A.M., Nanda, N.C., (1998), Analysis of the proximal orifice flow-field under pulsatile flow conditions and confining wall geometry: Implications in valvular regurgitation, Echocardiography: American Journal of CV ultrasound and Allied Tech. ,15(3), 219-232.

Anayiotos, A.S., Perry, G.J., Myers, J.G., Green, D.W., Fan, P.H., Nanda, N.C., (1995), A numerical and experimental investigation of the flow acceleration region proximal to an orifice, Ultrasound in Medicine and Biology, 21(4), 501-516.

ASCE (1995), Guidelines for Design of Intakes for Hydroelectric Plants, ASCE, NY.

Birch, R., and Lemon, D., (1993), Acoustic flow measurements at the Rocky Reach dam, Proc., Waterpower 93, ASCE, Tennessee, 2187-2196.

Boubee, J.A.T., and Williams, E.K., (2006), Downstream passage of silver eels at a small hydroelectric facility, Fisheries Management and Eco.,13,165-176.

Brooks, N.H., and Koh, R.C.Y., (1969), Selective withdrawal from density stratified reservoirs, Proceedings of the ASCE, Journal of the Hydraulics Division, HY4, 1369-1400.

Bryant, D.B., Khan, A.A., and Aziz, N.M., (2008), Investigation of flow upstream of orifices, Journal of Hydraulic Engineering, 134(1), 98-104.

Carriveau, E.C., Baddour, R.E., Kopp, G.A., (2002), The entrainment envelope of dye-core vortices at submerged hydraulic intakes, Canadian Journal of Civil Engineering, 29, 400-408.

Christman, B., Lang, A., and Walter, R., (1997), Surface collector impact upon turbine efficiency, Proc. Waterpower 97, ASCE, Georgia, 1737-1746.

Cook, C.B., and Richmond, M.C., (2004), Simulating the Flow Field Upstream of the Dworshak Dam Regulating Outlets, Pacific Northwest National Laboratory, Washington.

Cotroneo, G.V., and O’Dea, D.T., (1984), Physical hydraulic modeling for a small hydroelectric redevelopment, Proc. Water for Resource Development, ASCE, ID, 454-458.

Craya, A., (1949), Theoretical research on the flow of nonhomogenous fluids, La Houille Blanche, 4, 44-55.

EPRI (1992), Fish Entrainment and Turbine Mortality Review and Guideline, Final Report, Electric Power Research Institute, TR 101231.

Haque, M.M., Koken, M., Constantinescu, G., and Weber, L., (2005), Use of a 3D RANS model to predict stratification effects related to fish passage at hydropower dams, Proc., XXXIst International Association of Hydraulic Research Congress, Seoul, Korea.

Johnson, G.E., Khan, F., Skalski, J.R., Rakowski, C.L., Richmond, M.C., Serkowski, J.A., (2006), Hydroacoustic Evaluation of Juvenile Salmonid Passage at the Dalles Dam Spillway, 2005, Final Report, Pacific Northwest National Laboratory.

Johnson, P.L., and Vermeyen, T.B., (1993), A flexible curtain structure for control of vertical reservoir mixing generated by plunging inflows, Proc., Conference on Hydraulic Engineering, ASCE, 2377-2382, California.

Khan, L.A., Wicklein, E.A., Rashid, M., Ebner, L.L., and Richards, N.A., (2004), Computational fluid dynamics modeling of turbine intake hydraulics at a hydropower plant, Journal of Hydraulic Research, 42(1), 61-69.

Khan, L.A., Wicklein, E.A., Rashid, M., Ebner, L.L., and Richards, N.A., (2002), Analyses of the forebay hydraulics of the Dalles dam, Oregon for different spill scenarios, Proc., Hydro Vision 2002, Oregon.

Khangaonkar, T., Yang, Z., DeGaspari,C., Marshall, K., (2005), Modeling hydrothermal response of a reservoir to modifications at a high-head dam, Water International, 30(3), 378-388.

Koh, R.C.Y., (1966), Viscous stratified flow towards a sink, Journal of Fluid Mechanics, 24(3), 555-575.

Kubitschek, J., Sund, R., and Christensen, R., (1997), Selective withdrawal at Hungry Horse dam, Montana, Proc., Waterpower 97, 421-430.

Lai, Y.G., Weber, L.J., Patel, V.C., (2003), Nonhydrostatic three dimensional model for hydraulic flow simulation. II: Validation and application, Journal of Hydraulic Engineering, 129(3), 206-214.

Mahony, J.J., Pritchard, W.G., (1981), Withdrawal from a reservoir of stratified fluid, Proceedings of the Royal Society of London. Series A, Mathematical and Physical Sciences, 376 (1767), 499-523.

Marghzar, S.M., Montazerin, N., and Rahimzadeh, H., (2003), Flow field, turbulence and critical conditiona at a horizontal water intake, Proc., Institution of Mechanical Engineers.: J. Power and Energy, 317(A),53-62.

Meselhe, E.A., Weber, L.J., Odgaard, A.J., Johnson, T., (2000), Numerical modeling for fish-diversion studies, Journal of Hydraulic Engineering, 126(5), 365-374.

Meselhe, E.A., Odgaard, A.J.,(1998), 3D numerical flow model for fish diversion studies at Wanapum dam, Journal of Hydraulic Engineering, 124 (12), 1203-1214.

Meselhe, E.A., Odgaard, A.J., and Patel, V.C., (1996), Three-dimensional numerical model for fish diversion studies, Proc., Hydrosoft 96, 281-290.

Mih, W.C., (1991), Improved intake design for downstream migrating fish at hydropower plants, Proc., Hydraulic Engineering 1991, ASCE, Tennessee, 822-827.

Mih, W.C., (1987), Research to improve Bonneville second power house for migrating juvenile salmon, Proc., Waterpower 87, Oregon, 582-589.

Murray, D.G., (1993), Design criteria for water power intakes, Proc., Waterpower 93, ASCE, Tennessee, 1368-1377.

NPP (2005), Fish Entrainment and Mortality Study, Vol 1, Niagra Power Project, New York Power Authority.

Odeh, M., and Orvis, C.,(1997), Status of downstream fish passage at hydroelectric projects in the northeast, USA, Proc., Waterpower 97, ASCE, Georgia, 645-654.

Ploskey, G.R., Carlson, T.J.,(1999), Comparison of hydroacoustic and net estimates of fish guidance efficiency of an extended submersible bas screen at John Day dam, North American Journal of Fisheries Management, 19, 1066-1079.

Rajendran, V.P., Patel, V.C., (2000), Measurement of vortices in model pump-intake bay by PIV, Journal of Hydraulic Engineering, 126(5), 322-334.

Rakowski, C.L., Richmond, M.C., Serkowski, J.A., Ebner, L., (2002), Three dimensional simulation of forebay and turbine intakes flows for the Bonneville project, Proc., of Hydro Vision 2002, Oregon.

Rodriguez, L., Anconina, J., Flachskampf, F.A., Weyman, A.E., Levine, R.A., and Thomas, J.D., (1992), Impact of finite orifice size on proximal flow convergence. Implications for Doppler quantification of valvular regurgitation, Circulation Research, Journal of the American Heart Association, 70, 923-930.

Shammaa, Y. and Zhu, D.Z., (2010), Selective withdrawal in two layer fluids using a temperature control curtain, Journal of Hydraulic Engineering, 136(4), 236-244.

Shammaa, Y., Zhu, D.Z., and Rajaratnam, N., (2009), Flow field in a rectangular basin with a line inlet and a circular outlet, Journal of Hydraulic Engineering., ASCE, 135(10), 857-864.

Shammaa, Y., Zhu, D.Z., and Rajaratnam, N., (2005), Flow upstream of orifices and sluice gates, Journal of Hydraulic Engineering, 131(2), 127-133.

Sweeney, C.E., Christman, B., and Gatton, B., (1997), Update on juvenile fish bypass at Rocky Reach dam, Proc., Waterpower 97, Georgia, 589-598.

Sweeney, C.E., Christman, B., and Weitkamp, D.E., (1995), Surface attraction fish bypass at Rockey Reach dam, Proc., Waterpower 95, 311-320, CA.

Tokyay, T.E., Constantinescu, S.G., (2006), Validation of a large-eddy simulation model to simulate flow in pump intakes of realistic geometry, Journal of Hydraulic Engineering, 132(12), 1303-1315.

Vermeyen, T.B., (2002), Measuring selective withdrawal characteristics using an Argonaut Acoustic Doppler Velocimeter in Folsom Lake, California, Proc., Hydraulic Measurements and Experimental Methods Conference, 2002, Colorado, USA, 1-9.

Vermeyen, T.B., (2000), Application of flexible curtains to control mixing and enable selective withdrawal in reservoirs, Proc., 5th International Symposium on Stratified Flows, 457-462, Vancouver.

Vermeyen, T.B., (1998), First year selective withdrawal performance of the Shasta dam temperature control device, Proc., Water Resources Engineering 98, 944-949.

Vermeyen, T.B., (1997), Modifying reservoir release temperatures using temperature control curtains, Proc., 27th Congress of the International Association of Hydraulic Research, IAHR, 483-488, California.

Vermeyen, T.B., and Johnson, P.L., (1993), Hydraulic performance of a flexible curtain used for selective withdrawal: A physical model and prototype comparison, Proc., Conference on Hydraulic Engineering, ASCE, 2371-2376, CA.

Wicklein, E.A., Khan, L.A., Rashid, M., Deering, M.K., and Nece, R.E., (2002), A three dimensional computational fluid dynamics model of the forebay of Howard Hanson dam, Washington, Proc., Hydro Vision 2002, Oregon.

Yih, C.S., (1958), On the flow of a stratified fluid, Proc., Third National Congress of Applied Mechanics, 857-861.

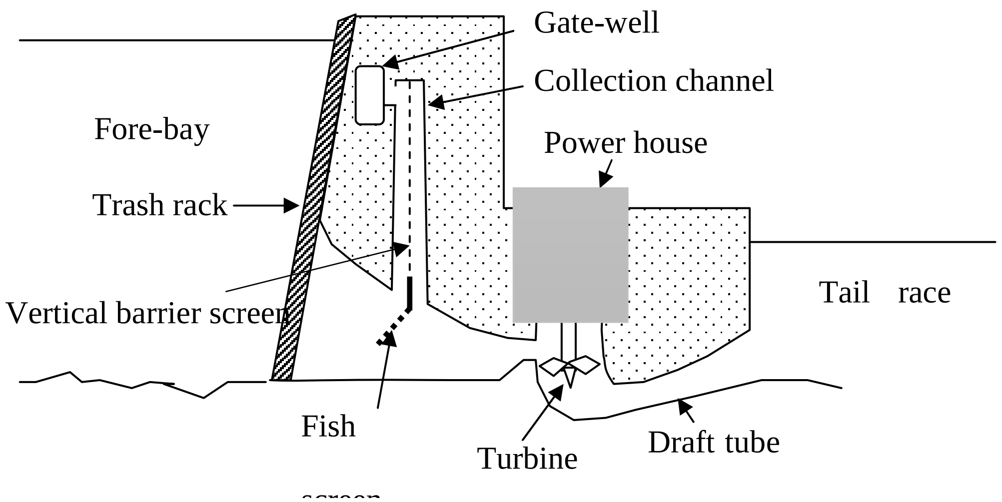

Figure 2.1: A qualitative diagram of the Bonneville second power-house facility and the fish passage system located on the Columbia River.

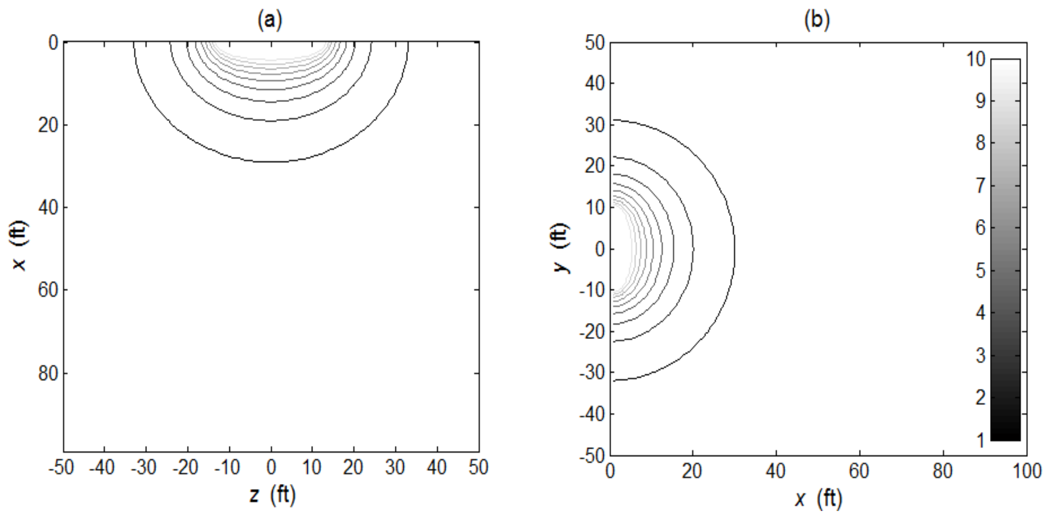

Figure 2.2: Contours of radial velocity upstream of the Dworshak dam intake #2, (single intake with Q = 5650 cfs).

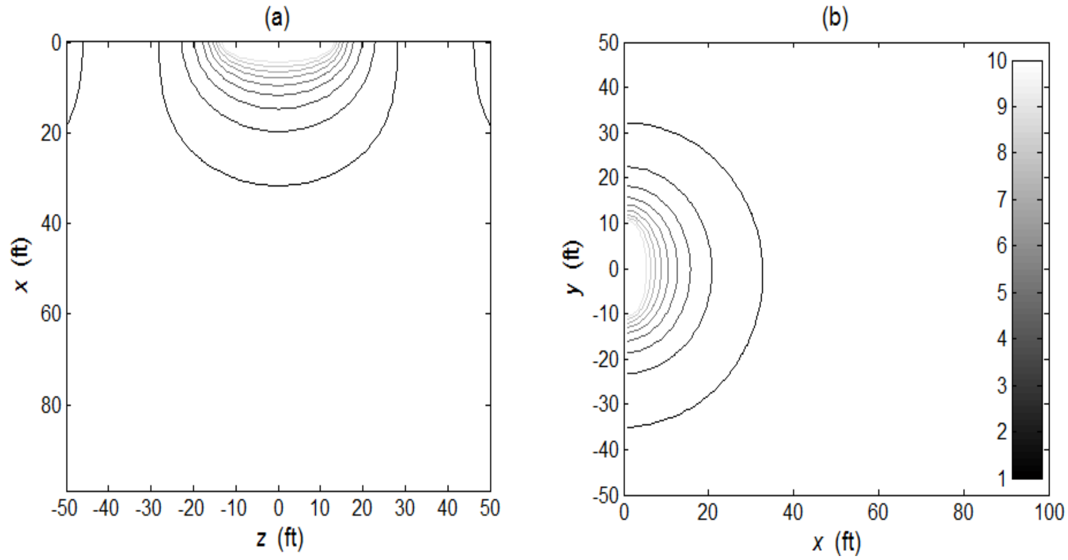

Figure 2.3: Contours of radial velocity upstream of the Dworshak dam intake #2, (three intakes with Q = 5650 cfs at each intake).

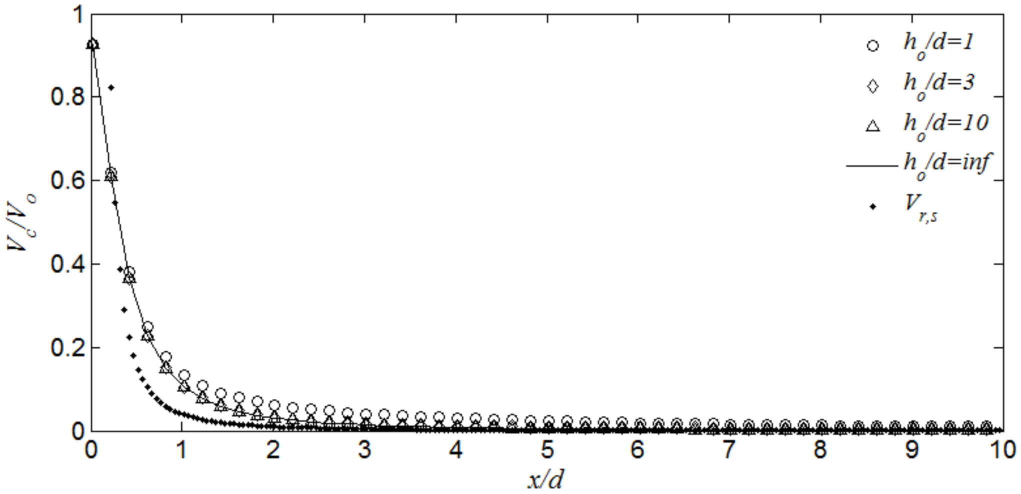

Figure 2.4: Decay of normalized centerline velocity for different water-depths having infinite width.

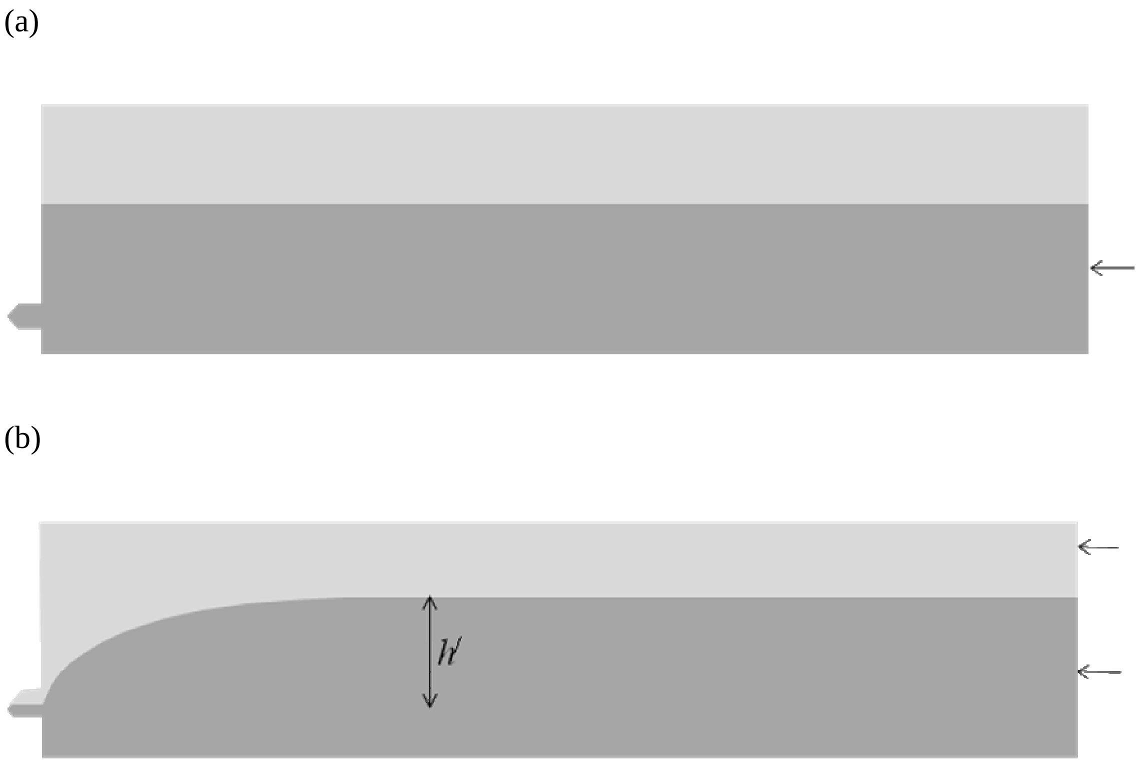

Figure 2.5: Demonstration of selective withdrawal, (a) only lower layer is flowing; (ii) both layers are flowing.

Chapter 3

A Numerical Study on Confined Wall Jets[2]

3.1 Introduction

Wall jets in confined spaces have wide range of engineering applications including selective withdrawal with a curtain (Shammaa and Zhu, 2010), flow in settling basins (Naser et al., 2005) and storage reservoirs (Hannoun and Boulos, 1997), among others. Rajaratnam (1965) treated a submerged jump as a wall jet under adverse pressure gradient with a recirculation zone on top. Wu and Rajaratnam (1995) found that velocity profiles in submerged jump may show wall jet like or free jump like behavior in different scenarios; the reason was not adequately identified. Ead and Rajaratnam (2002)'s study showed that momentum flux is preserved up to some distance, and thereafter wall jet behavior is lost. The reason for this phenomenon was not well understood. Shammaa et al. (2009)

---

[2] A version of this chapter has been submitted to the Journal of Hydraulic Research.

studied wall jet behavior in a confined space at a comparatively lower inlet Reynolds number. However, any systematic investigation on how wall jet properties are affected by inlet Reynolds number and confinement are not available in the literature. Although backward step flow experiments (Nie and Armaly, 2004) are concerned with recirculation pattern in a geometric expansion, this area of research uses large inlet opening compared to the channel depth and therefore not comparable with jet flow. The numerical simulation of submerged jump was attempted by Long et al. (1991), Ma et al. (2002); among others. These studies showed that numerical solvers have excellent capability in predicting jet behaviors in a submerged jump.

It appears that there is a necessity of doing further research on this area in order to get reasonable answer of some unexplained behavior in earlier studies, and to get a complete picture on how confinement can affect the jet behavior. Therefore, this study has two primary objectives: (a) to find out the reason for several unexplained wall jet behaviors, and (b) to carry out systematic investigation on the effect of water depth, inlet Reynolds number and length scale on wall jet.

This study primarily uses a CFD solver (ANSYS CFX) to obtain the flow field. The accuracy of the CFD solver is verified by eight experiments.

3.2 Numerical Model Description

3.2.1 Governing Equations

The numerical model solves three-dimensional unsteady Reynolds Averaged

Navier Stokes (RANS) equation using unstructured mesh and a two-equation turbulence model to assess the eddy viscosity. The free surface was modelled with the Volume of Fluid (VOF) method. The continuity and the momentum equations solved by the CFX solver (ANSYS CFX) is as follows (in tensor form),

$$\frac{\partial \rho u_j}{\partial x_j} = 0$$

$$\frac{\partial \rho u_i}{\partial t} + \frac{\partial \rho u_j u_i}{\partial x_j} = -\frac{\partial p}{\partial x_i} + \frac{\partial}{\partial x_j}\left\{(\mu + \mu_t)\left(\frac{\partial u_i}{\partial x_j} + \frac{\partial u_j}{\partial x_i}\right) - \frac{2}{3}\rho k \delta_{ij}\right\} + (\rho - \rho_a) g_i$$

$$\rho = \alpha_w \rho_w + \alpha_a \rho_a$$

$$\mu = \alpha_w \mu_w + \alpha_a \mu_a$$

Equation 3.1

where, ρ_w is the density of water, ρ_a is the density of air, α_w is the volume fraction of water, α_a is the volume fraction of air, k is the turbulent kinetic energy, δ_{ij} is the Kronecker delta, p is the pressure, μ_w is the molecular viscosity of water, and μ_a is the molecular viscosity of air. The transport equation for α_w and α_a are,

$$\frac{\partial \alpha_w}{\partial t} + u_j \frac{\partial \alpha_w}{\partial x_j} = 0$$

$$\alpha_a = 1 - \alpha_w$$

Equation 3.2

A curvature corrected $k-\varepsilon$ model is used to assess the eddy viscosity. This model applies Spalart and Shur (1997)’s curvature correction on Launder and Spalding (1974)’s $k-\varepsilon$ model. The governing equations are as follows,

$$\frac{\partial \rho k}{\partial t}+\frac{\partial \rho k u_j}{\partial x_j}=\frac{\partial}{\partial x_j}\left\{\left(\mu+\frac{\mu_t}{\sigma_k}\right)\frac{\partial k}{\partial x_j}\right\}+fP_k-\rho\varepsilon-\frac{\mu_t}{\sigma_\rho \rho}g_i\frac{\partial \rho}{\partial x_i}$$

$$\frac{\partial \rho \varepsilon}{\partial t}+\frac{\partial \rho \varepsilon u_j}{\partial x_j}=\frac{\partial}{\partial x_j}\left\{\left(\mu+\frac{\mu_t}{\sigma_\varepsilon}\right)\frac{\partial \varepsilon}{\partial x_j}\right\}+C_1\frac{\varepsilon}{k}P_k-C_2\rho\frac{\varepsilon^2}{k}$$

$$P_k=\mu_t\left(\frac{\partial u_i}{\partial x_j}+\frac{\partial u_j}{\partial x_i}\right)\frac{\partial u_i}{\partial x_j}$$

$$\mu_t=\rho C_\mu\frac{k^2}{\varepsilon}$$

Equation 3.3

where, μ_t is the eddy viscosity, P_k is the production of turbulence. Standard values for the model constants are used, which are: C_1=1.44, $C_2=1.92$, $\sigma_k=1.0, \sigma_\varepsilon=1.3$, and $C_\mu=0.09$. In the buoyancy production term, σ_ρ= 2 is used. The curvature corrected $k-\varepsilon$ model multiplies P_k by a factor (*f*), to account for streamline curvature. The detail formulation to estimate f is given by Spalart and Shur (1997).

3.2.2 Boundary Conditions and Mesh

The numerical set-up is shown in Figure 3.1. In this figure, coordinates and velocity directions are shown by x, y, z and u, v, w respectively; *H* is the tail-water depth, and bin is the size of the inlet opening. The mass flow rate was provided at the upstream boundary, and zero static pressure was provided at the downstream boundary. No-slip boundaries were provided at side-walls. Hence, simulated results are two-dimensional in nature. The turbulence intensity (*I*) at the upstream boundary is specified as 1%. The solver uses the following expression to compute

k and ε at the inlet from the given value of intensity (CFX 2009),

$$k_{in} = \frac{3}{2} I^2 u_{in}^2 \qquad \varepsilon_{in} = \rho C_\mu \frac{k^2}{100 I \mu_l}$$

Equation 3.4

At the no-slip wall, CFX solver uses a no-flux boundary condition $(\partial k / \partial n = 0)$ for the kinetic energy equation. To calculate the dissipation rate (ε), the following equation was used,

$$\varepsilon = \frac{\rho u^* C_\mu^{3/4} k^{3/2}}{\mu \kappa \tilde{y}^*}$$

Equation 3.5

where, κ is the von-Karman constant, $\tilde{y}^*$ is $\rho u^* \Delta y / \mu$ or 11.06, whichever is larger, Δy is the distance of the first grid point from the wall, and u^* is computed by,

$$u^* = C_\mu^{1/4} k^{1/2}$$

Equation 3.6

The channel bottom was specified as a no-slip boundary, where standard wall function was used. The top surface was specified as an opening boundary. This is a pressure boundary which allows both inflow and outflow. The wall shear stress is computed as follows,

$$\tau_w = \rho u^* u_\tau$$

Equation 3.7

where, u^* is computed using Equation 3.6, and u_τ is computed using,

$$u_\tau = \frac{u}{\frac{1}{k} \ln\left(\rho u^* \Delta y / \mu\right) + 5.5}$$

Equation 3.8

The central difference scheme is used as the advection scheme. Unstructured tetrahedral mesh is used in the solution domain. Local refinement is provided in the wall jet layer. The thin wall jet layer was solved with about 25 nodes and maximum node spacing in this region was 1 mm. At other locations, maximum node spacing of 5 mm was used. The time step was varied from 0.05 to 0.1 second. The initial values of velocities were provided as zero and the initial pressure was assumed as hydrostatic for the water region and zero for the air region. For simulations B, the simulated result of a simulation is used as the initial condition for another simulation. Table 3.1 shows the flow and the geometric variables of all numerical test runs. Series A assesses the water depth effect, series B assesses the inlet Reynolds number effect, series C is carried out to validate empirical expressions, and series D is carried out to assess the effect of length scale and the outlet.

3.2.3 Validation and Sensitivity Tests

Eight simulations (simulation A2, A6, B7, B8, C7, D3, D4, and D5) are validated with experiments. The experimental data is taken with a four beam ADV probe (Probe ID: Vectrino VCN 7569, Nortek AS). The sampling frequency is 200 Hz and the data at each point is averaged for 5 minutes.

The experiment was conducted at the T.R. Blench Hydraulics Laboratory of the University of Alberta. The experimental set-up is similar to the geometry shown in Figure 3.1 having a width of 0.485 m. The height and location of the outlet weir can be varied and the spilled water was recirculated using a pump. The flow-rate was measured by a magnetic flow-meter. Figure 3.2 shows the experimental and the numerical velocity profiles for simulation B8. Figure 3.3 shows the comparison of simulation and the experiment of Shammaa et al. (2009) conducted at inlet Reynolds number 1250. The correlation coefficient between the experimental and the numerical measurement is found to be 0.99 in all the test cases. The Mean Absolute Error (MAE) is also found to be less than 0.05 m/s in all these cases. The MAE is computed by averaging absolute differences between the experimental and the simulated result. Sensitivity for the inlet turbulence intensity (I) is tested for the simulation B8 by increasing intensity to 5% and no sensitivity is observed. Grid independence was checked for the simulation A8, B6, and B9 by doubling the nodes, and no notable difference was observed. Figure 3.4 shows the grid independence check for the simulation A9.

3.3 Results and Analysis

3.3.1 Momentum Flux Balance

Figure 3.5 shows the plot of the streamline, normalized stream-wise momentum flux and pressure integral for the simulation C4. The stream-wise momentum flux (M) and the pressure integral (P) are computed as follows,

$$M = \int_{y=0}^{H} \rho u^2(y)dy$$

$$P = \int_{y=0}^{H} p(y)dy$$

Equation 3.9

where, $p(y)$ and $u(y)$ are the pressure and stream-wise velocity at depth y located at x. In Figure 3.5 , M_{in} is $\rho u_{in}^2 b_{in}$,where u_{in} is the average velocity at the inlet, and P_{ref} is P at x = 0.

The center of the recirculation zone is located close to x/H = 2.0 (Figure 3.5a). Figure 3.5b shows that downstream of this location stream-wise momentum flux decreases and pressure integral (or pressure force) increases. The recirculation ends at x/H = 5, and both momentum fluxes and pressure integrals are nearly constant downstream of this location. This rise in pressure integral downstream of the center of recirculation causes loss of momentum flux. As the pressure gradient is adverse beyond the center of recirculation, flow is not expected to behave as a classical wall jet in this region. The momentum loss in the case of wall jet with finite water depth was observed by Ead and Rajaratnam (2002).

Based on the distribution of the pressure integral, the flow domain can be divided into four distinct regions (Figure 3.5): region I extends from the origin to the center of recirculation, where pressure-integral shows near zero gradient; region II extends from the center of the recirculation to the point where recirculation ends (u is positive at surface), where pressure integral shows steep adverse gradient; region III extends from the end point of recirculation to the point where zero pressure gradient (ZPG) exists; and region IV is the outlet region where pressure drop is observed due to the effect of the outlet. This pressure distribution and classification is valid for and assessed at S_u>0.5, H/b_{in}>8.0, and R_{in} >1,200. When S_u <0.5, or H/b_{in}<8.0, pressure gradient can be adverse in region I and the classification is not applicable for these regimes. As the horizontal extent of the region I and region II are affected by the depth of the inlet wall ($H - b_{in}$), or water depth (when $H >> b_{in}$), the scaling parameter for these figures are chosen as H. The main difference between this classification and the classification of Shammaa et al. (2009) is that this classification is based on the pressure distribution inside the domain, while Shammaa et al. (2009)'s classification is based on the observed flow structure.

3.3.2 Effect of Water Depth

Effect of water depth on stream wise velocity profile is assessed in series A (Table 3.1). Figure 3.6 shows the normalized velocity profile at $x/H = 2.0$ with H/b_{in} of 24, 20, 16, 12, and 8. The normalization is done by the maximum stream-wise velocity (u_m), and the jet half width (b) at this section. The jet half width is defined as the vertical distance from the bottom of the channel to the point where $u = u_m/2$ located in the free shear layer. Figure 3.6 shows that u velocity profiles are self-similar. Experimental wall jet profile of Abrahamson et al. (1994) of infinite environment is added in this figure.

In wall jet, the decay of the maximum velocity (u_m) along x can be well approximated by the relationship,

$$\frac{u_m}{u_{in}} = \frac{c}{\left(x/b_{in}\right)^{1/2}}$$

Equation 3.10

where, c is the decay coefficient. Ead and Rajaratnam (2002) found c = 4.0 in their wall jet study. Figure 3.7 shows velocity decay curve for various H/b_{in} ratio for $R_{in} = 31{,}300$, where R_{in} is the inlet Reynolds number, computed by $u_{in}b_{in}/\nu$. It is observed that at this R_{in} and at $H/b_{in} \geq 14$ velocity decay profiles collapse in region I and can be fitted by Equation 3.10 with c = 4.0. At $H/b_{in} < 14$, velocity decays faster and k = 4.0 is found no longer applicable. At $H/b_{in} < 8$, water depth is smaller than the length of the potential core ($\approx 15b_{in}$) and the center of recirculation falls inside the potential core. This causes the decay of velocity inside the potential core as observed in Figure 3.7. Free jump profile from Rajaratnam (1965)'s data is added in Figure 3.7. It is observed that at low H/bin ratio, velocity profiles get closer to the free jump like profile even though submergence is high (simulation A9) or flow is subcritical (simulation A10). Potential core is not observed in simulations A9 and A10, which also observed in free jump.

Figure 3.8 shows the normalized pressure integral for simulations A3, A4, A6, A7, and A8. This figure shows that at shallow water depth ($H/b_{in} < 8$) the pressure integral shows strong adverse gradient at region I, which in turn causes increased decay of stream-wise velocity. This is for this reason free-jump like behavior is observed at this range of H/b_{in}.

Jet spreading rate (S) is defined as the rate of change of jet half width with x, or db/dx. The literature regarding the spreading rate of wall jet (S) shows high degree of scatter. Launder and Rodi (1981) compiled jet spreading and other wall jet variables of fifteen experiments available in the literature. Schneider and Goldstein (1994) added four new experimental results on Launder and Rodi (1981)'s compilation. The compilation of these 19 experiments along with Eriksson et al. (1998) and Abrahamsson et al. (1994)'s experiment show that jet spreading rate varies from 0.056 to 0.085 for inlet Reynolds number (R_{in}) ranges from 6,080 to 56,000. This study finds that with increasing H/b_{in} ratio, jet spreading rate decreases. At $H/b_{in} > 14$, the asymptotic value of the jet spreading rate is found to be 0.076, which is equal to the value found by Ead and Rajaratnam (2002).

3.3.3 Effect of Inlet Reynolds Number

The B series simulations are carried out to assess the effect of Inlet Reynolds number (R_{in}). The R_{in} is varied from 1,250 to 83,300. It is found that self similarity is preserved in the whole range tested. However, velocity decay coefficient (c) is found to increase with increasing R_{in}. Figure 3.9 shows the profiles of um at various R_{in} for $H/b_{in} \approx 14$. It is observed that profiles achieve the wall jet profile (c= 4) at R_{in} > 10,400 for $H/b_{in} \approx 14$. Assessing Figure 3.7 and Figure 3.9, it appears that wall jet behavior is affected by both H/b_{in} ratio and R_{in} at typically low Reynolds number and at shallow water depth.

Jet spreading rate is found to decrease with increasing R_{in} at lower Reynolds number. At R_{in} >10,000, the jet spreading rate becomes asymptotic to 0.076, the value obtained by Ead and Rajaratnam (2002). Abrahamsson et al. (1994)'s work shows that jet spreading is decreasing with increasing inlet Reynolds number even at R_{in} greater than 10,000. For circular jet, Rajaratnam and Flint-Petersen (1989) reported a 25% increase in jet spreading rate at Reynolds number equal to 2,000 compared to its asymptotic value.

Increasing flow velocity at the inlet causes decrease in submergence (S_u) and flow becomes closer to the free jump. Submergence is computed as $(H - y_2)/b_{in}$, where y_2 is the sequent depth. It is observed that at submergence < 0.5, pressure integral can be strongly adverse in region I, and velocity profiles get closer to the free jump.

3.3.4 Empirical Expressions

Attempt is made to predict the velocity decay coefficient (c) and the jet spreading rate for varying H/b_{in} ratio and R_{in}. Figure 3.10 shows the variation of the velocity decay coefficient (c) and the jet spreading rate (b) with $R_{in}^{1/2}(H/b_{in})$. It is observed that these variations can be fitted by the following expressions,

$$c = 2.516(R_{in})^{0.027}\left(\frac{H}{b_{in}}\right)^{0.054}$$

Equation 3.11

$$S = 0.146(R_{in})^{-0.04}\left(\frac{H}{b_{in}}\right)^{-0.08}$$

Equation 3.12

The empirical expressions are applicable and assessed at $S_u > 0.5$, $H/b_{in} > 8.0$, and $R_{in} > 1{,}200$. The C series data are used as the validation data for empirical equations. Figure 3.10 shows simulated and empirical velocity profiles for these simulations (C1 to C7). Satisfactory agreement between the two was noted in region I. Based on the fitted equations, the standard wall jet behavior can be expected at $R_{in}^{1/2} H / b_{in}$ > 4,000.

The empirical expressions are not applicable at submergence, S_u < 0.5 where strong adverse pressure gradient prevails in region I. The empirical expressions are also not applicable at H / b_{in} < 8, where region I falls inside or at significantly close to the potential core. Strong adverse pressure gradient also exists in region I in this case, and potential core may not exist.

Wu and Rajaratnam (1995) found free jump-like behavior in several experiments at submergence as high as 7.42; the reason for such surprising behavior was not well explained. This study finds that in all those experiments H/b_{in} ratio varies from 4.5 to 9. This could be the reason for getting the free jump-like behavior at large submergence. It should be mentioned that at H/b_{in} = 2.0, and at large submergence, flow field can be well approximated by backward step flow experiments (Nie and Armaly, 2004).

Rajaratnam (1965) considered submerged jump as a wall jet under adverse pressure gradient. However, this study finds that pressure gradient is always adverse in region II only. In region I, pressure gradient is adverse when S_u < 0.5 or H/b_{in} < 8.0, and favorable otherwise. This feature is also observed in the pressure profiles measured by Rajaratnam (1965).

The wall shear stress is an important design parameter and is necessary to identify the scour. The wall shear stress in these simulations shows a similar profile as observed by Ead and Rajaratnam (2002) in the wall jet study and by Long et al. (1991) in the submerged jump study. The maximum wall shear stress at the inlet can be computed by,

$$\tau_{w,\max} = 0.0035 \rho u_{in}^2$$

Equation 3.13

It is verified that this empirical equation also works well for earlier works of Ead and Rajaratnam (2002) and Long et al. (1991).

Although simulations and experiments were conducted on smooth boundary, the field scenario may have rough boundary. A non-dimensional parameter to express roughness is Nikuradse's roughness (k^+) defined as, $k_s u^* / \nu$, where k_s is the roughness height. A surface is fully rough when $k^+>70$. Smith (2008) experimented effect of roughness on wall jet up to $k^+ = 130$ and found no notable effect on the velocity decay coefficient and jet spreading rate. Hence, empirical equations developed in this study may be applicable until $k^+ =130$.

3.4 Effect of Channel Length and Outlet

Series from D1 to D5 in Table 3.1 shows simulations used to analyze the effect of channel length. These five simulations have L/H ratio equal to 8.3, 6.8, 3.0, 2.1, and 1.5. The recirculation eddy is typically extended up to L/H = 5.0 and therefore simulations D1 and D2 did not show any effect of length scale on the jet region as L/H ratio in these two simulations were greater than 5.0. Figure 3.12

shows the streamline plot of flow field for simulation D3, D4, and D5. In simulation D3, the outlet weir is placed in region II and it was observed that region I was still unaffected by the outlet weir. In simulations D4 and D5, the outlet weir was placed inside region I. It was observed that the center of the recirculation was shifted to $0.66L$ in both cases. In these two cases flow behavior is similar to that observed in the case of impinging jet experiment by Beltaos and Rajaratnam (1972). Wall jet behavior is observed with increased spreading rate in region I, which extends to the center of recirculation located at a distance equal to $0.66L$ downstream of the inlet wall. Beyond that limit, impingement effect is predominant and the pressure integral increases. This increase in pressure integral is due to the combined effect of stagnation pressure developed by the outlet wall and the momentum loss.

The effect of weir was not observed at a distance $0.3L$ upstream of the weir. To get a complete understanding of the outlet influence, two simulations were carried out (D6 and D7) with line sink outlet located at mid-depth and channel bottom, respectively. Figure 3.13 shows the flow upstream of the line sink outlet located at mid-depth. The size of the line sink outlet was 2 cm.

A characteristic length scale to describe the influence of the outlet can be obtained by comparing the outlet induced velocity with the mean approaching velocity ($U_a = q/H$). For a line sink in a half-space, the sink induced velocity is $q/\pi r$. By equating this to U_a, one obtains,

$$r = H/\pi$$

Equation 3.14

where, r is the radial distance from the line sink. For point sink, similar derivation yields,

$$r = \sqrt{WH / 2\pi}$$

Equation 3.15

However, for the cases where outlet wall is placed inside the recirculation zone, these equations are not applicable. Figure 3.13 shows that the effect of line sink is almost negligible at a distance $0.3H$ upstream of the sink location, which is consistent with Equation 3.14.

3.5 Conclusions

This numerical study analyzes the wall jet behavior in a confined space for different inlet Reynolds number and water depths. Eight numerical results are validated with experimental data which shows satisfactory agreement. Simulation shows wall jet and a recirculation eddy on top of it, which is a typical submerged jump flow structure. Flow shows wall jet like behavior only up to the center of recirculation zone. Pressure rises sharply beyond the center of the recirculation zone and becomes constant where the recirculation ceases. This adverse pressure gradient causes loss of the momentum flux in this region.

Simulations show that the jet spreading rate, and the decay of the streamwise velocity varies with the inlet Reynolds number and with water depth at comparatively lower Reynolds number (<10,000), and at shallow water depth. A dimensionless number is found which can account for both effects. Empirical expressions are developed to predict the jet spreading rate and the decay coefficient as a function of this dimensionless number. It is observed that standard wall jet behavior is retrieved when this number is greater than 4,000.

It is observed that confinement does not affect the behavior of the jet and the recirculation zone when the length of the channel is greater than the natural length of the recirculation zone which is typically $5H$. When outlet wall is placed inside the recirculation zone, the center of recirculation is shifted upstream and the wall jet behaves as an impingement jet on the outlet wall. Outlet's type (weir or line sink) and the distance of the line sink from the channel bottom do not affect the behavior of the wall jet and the recirculation zone. Equations are developed to predict the region accelerated by the line sink outlet.

3.6 References

Abrahamsson, H., Johansson, B., and Lofdahl, L., (1994), A turbulent plane two-dimensional wall jet in a quiescent surrounding, Eur. J. Mech., B/Fluids, 13(5), 533-556.

Beltaos, S., and Rajaratnam, N., (1972), Plane turbulent impinging jets, Journal of Hydraulic Research, 11(1), 29-57.

CFX (2009), ANSYS CFX Solver Theory Guide, Release 12.0, ANSYS Inc., PA.

Ead, S.A., and Rajaratnam, N., (2002), Plane turbulent wall jets in shallow tailwater, Journal of Engineering Mechanics, ASCE.

Eriksson, J.G., Karlsson, R.I., and Persson, J., (1998), An experimental study of a two-dimensional plane turbulent wall jet, Experiments in Fluids, 25, 50-

60.

Hannoun, I.A., and Boulos, P.F. (1997), Optimizing distribution storage water quality: A hydrodynamic approach, Applied Mathematical Modeling, 21, 495-502.

Launder, B.E., and Spalding, D.B., (1974), The numerical computations of turbulent flows, Computer Methods in Applied Mechanics and Engineering, 3, 269-289.

Launder, B.E., and Rodi, W., (1981), The turbulent wall jet, Progress in Aerospace Sciences,19, 81-128.

Long, D., Steffler, P.M., and Rajaratnam, N., (1991), A numerical study of submerged hydraulic jumps, Journal of Hydraulic Research, 29(3), 293-308.

Ma, F., Hou, Y., and Prinos, P.,(2001), Numerical calculation of submerged hydraulic jumps, Journal of Hydraulic Research, 39(5), 493-503.

Naser, G., Karney, B.W., and Salehi, A.A., (2005), Two-dimensional simulation model of sediment removal and flow in rectangular sedimentation basin, Journal of Environmental Engineering., 131(12),1740-1749.

Nie, J.H., and Armaly, B.F., (2004), Reverse flow regions in three dimensional backward facing step flow, International Journal of Heat and Mass Transfer, 47, 4713-4720.

Rajaratnam, N., and Flint-Petersen, L., (1989), Low Reynolds number circular turbulent jets. Proc., Institution of Civil Engineers, Water Engineering Group, 87(2), 299-305.

Rajaratnam, N., (1965), Submerged hydraulic jump, Journal of the Hydraulics Division, Proc. of the ASCE, HY4, 71-95.

Rajaratnam, N., (1965b), The hydraulic jump as a wall jet, Journal of the Hydraulics Division, Proc. of the ASCE, HY 5, 107-131.

Shammaa, Y. and Zhu, D.Z., (2010), Selective withdrawal in two layer fluids using a temperature control curtain, Journal of Hydraulic Engineering, 136(4), 236-244.

Shammaa, Y., Zhu, D.Z., and Rajaratnam, N., (2009), Flow field in a rectangular basin with a line inlet and a circular outlet, Journal of Hydraulic Engineering., ASCE, 135(10), 857-864.

Schneider, M.E., and Goldstein, R.J., (1994), Laser Doppler measurement of turbulence parameters in a two-dimensional plane wall jet, Physics of Fluids, 6(9), 3116-3129.

Smith, B.S., (2008), Wall Jet Boundary Layer Flows Over Smooth and Rough Surfaces, PhD thesis, Virginia Polytechnic Institute.

Spalart, P.R., and Shur, M., (1997), On the sensitization of turbulence model to rotation and curvature, Aerospace Sci. Tech., 1(5), 297-302.

Wu, S., and Rajaratnam, N., (1995), Free jumps, submerged jumps, and wall jets, Journal of Hydraulic Research, 33(2), 197-212.

Table 3.1: Description of simulations carried out.

Simulation	Inlet velocity, (u_{in}), m/s	Inlet size, b_{in} ,m	Water depth, (H), m	Inlet Reynolds No, (R_{in})	Channel length, (L), m	Inlet Froude No, (F_{in})	H/b_{in}	Submergence, (S_u)
A1	1.23	0.0254	0.6	31,300	3.5	2.47	24	6.8
[1]A2	1.23	0.0254	0.5	31,300	3.0	2.47	20	5.5
A3	1.23	0.0254	0.41	31,300	2.46	2.47	16	4.2
A4	1.23	0.0254	0.31	31,300	2.46	2.47	12	2.9
A5	1.23	0.0254	0.25	31,300	2.46	2.47	10	2.25
[1]A6	1.23	0.0254	0.2	31,300	2.46	2.47	8	1.47
A7	1.23	0.0254	0.16	31,300	2.46	2.47	6	0.95
A8	1.23	0.0254	0.13	31,300	2.46	2.47	5	0.56
A9	0.82	0.0254	0.2	20,800	2.46	1.65	7.8	3.1
A10	0.4	0.0254	0.18	10,030	2.46	0.8	7	-
B1	0.05	0.0254	0.31	1,250	2.46	0.1	12	-
B2	0.077	0.0254	0.31	1,880	2.46	0.15	12	-
B3	0.1	0.0254	0.31	2,500	2.46	0.2	12	-
B4	0.14	0.0254	0.31	3,760	2.46	0.3	12	-
B5	0.41	0.0254	0.33	10,400	2.46	0.82	13	-
B6	0.61	0.0254	0.34	15,600	2.46	1.23	14	9.1
[1]B7	0.82	0.0254	0.35	20,800	2.46	1.65	14	6.2
[1]B8	1.23	0.0254	0.36	31,300	2.46	2.47	14	3.65
B9	2.44	0.0254	0.39	62,000	2.46	4.9	15	1.4
B10	3.27	0.0254	0.4	83,300	2.46	6.56	16	0.79
C1	2.1	0.015	0.3	31,300	2.46	5.44	20	1.77
C2	1.2	0.015	0.29	18,000	2.46	3.13	19	4.0
C3	3.0	0.015	0.32	45,100	2.46	7.84	21	0.9
C4	2.44	0.0254	0.32	62,000	2.46	4.9	12.6	0.83
C5	0.2	0.0254	0.46	5,216	2.46	0.41	18	-
C6	0.61	0.0254	0.49	15,600	2.46	1.23	19	14
[1]C7	1.62	0.0254	0.37	41,300	2.46	3.25	14.5	2.5
D1	0.82	0.0254	0.36	20,800	3.0	1.65	7.8	3.1
D2	0.82	0.0254	0.36	20,800	2.46	1.65	7.8	3.1
[1]D3	0.82	0.0254	0.36	20,800	1.1	1.65	7.8	3.1
[1]D4	0.82	0.0254	0.36	20,800	0.76	1.65	7.8	3.1
[1]D5	0.82	0.0254	0.36	20,800	0.54	1.65	7.8	3.1
[2]D6	1.23	0.0254	0.2	31,300	2.46	2.47	8	1.47
[2]D7	1.23	0.0254	0.2	31,300	2.46	2.47	8	1.47

[1] validated by the experimental data.

[2] line sink was used in these simulations.

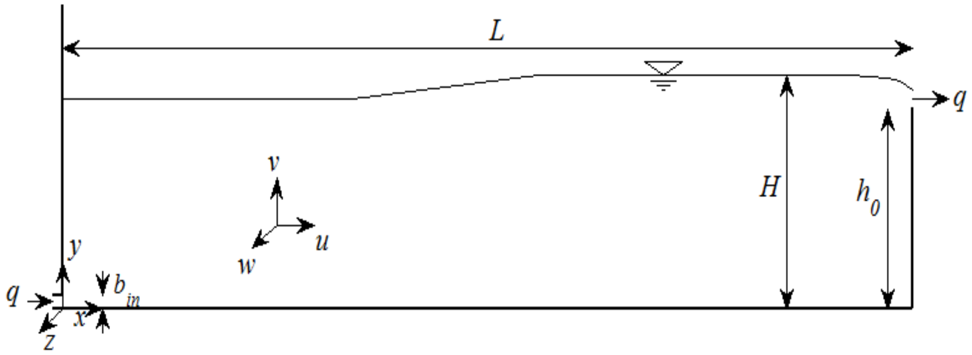

Figure 3.1: Side view of the schematic model geometry.

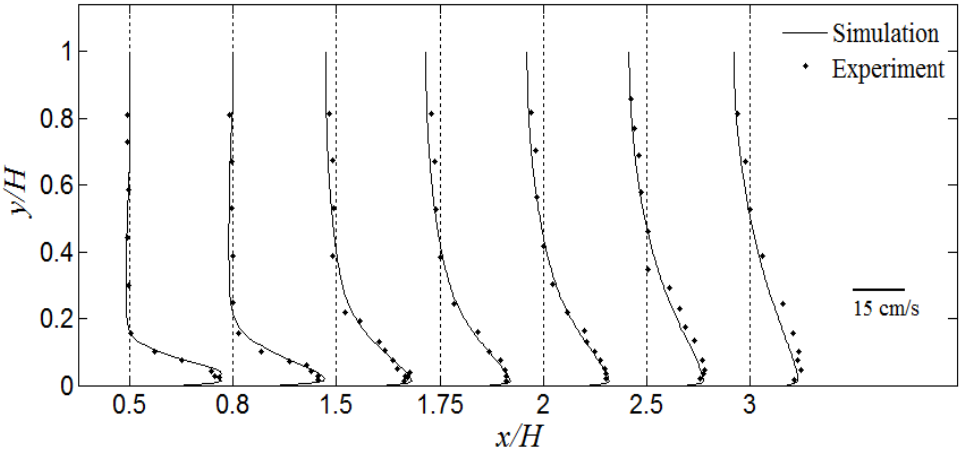

Figure 3.2: Comparison between numerical and experimental result for simulation B8.

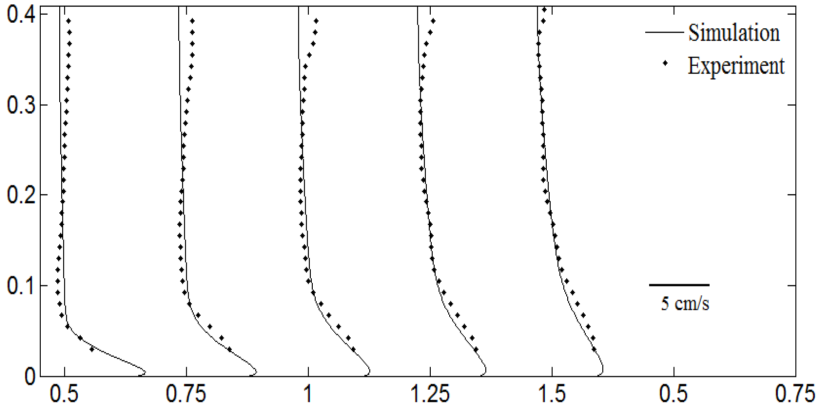

Figure 3.3: Comparison between simulation and Shammaa et al. (2009)`s experiment.

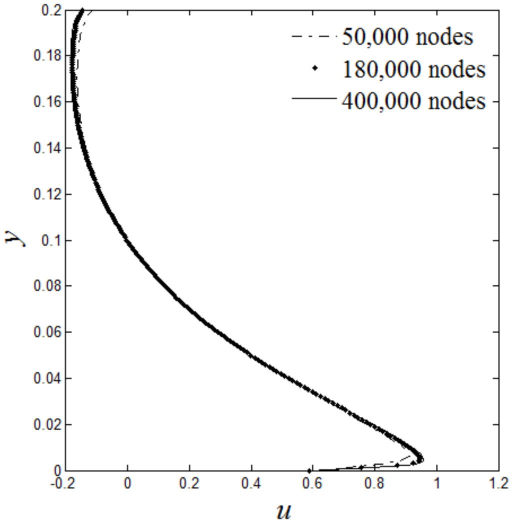

Figure 3.4: Grid independence check for the simulation A9.

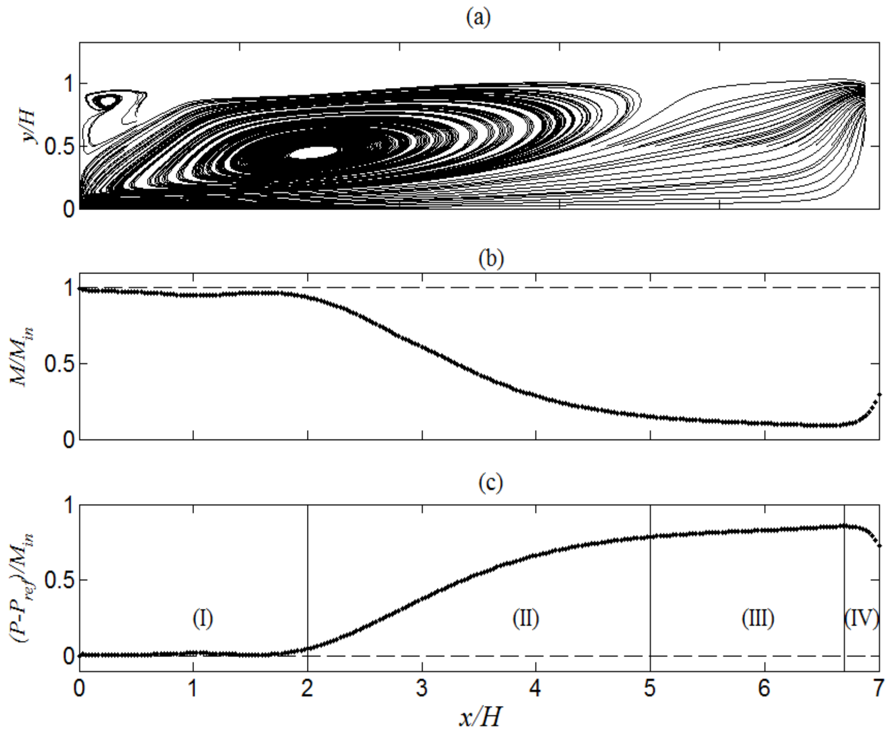

Figure 3.5: (a) Streamline plot, (b) normalized momentum flux, and (b) pressure integral with x for simulation C4.

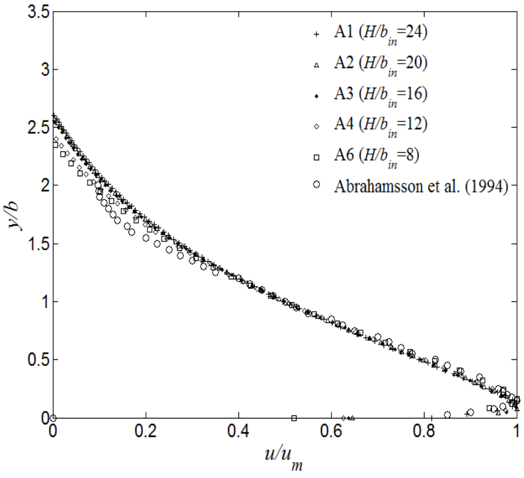

Figure 3.6: Normalized velocity profiles for simulations A1 to A4, and A6 at $(x/H = 2)$ and comparison with Abrahamsson et al. (1994)'s experimental data.

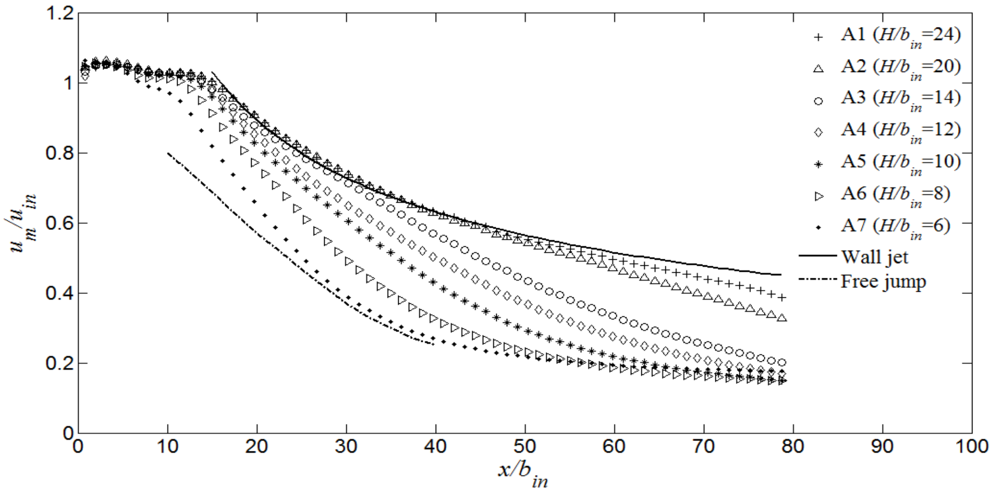

Figure 3.7: Maximum velocity profiles for different H/b_{in} ratio at R_{in} = 31,300.

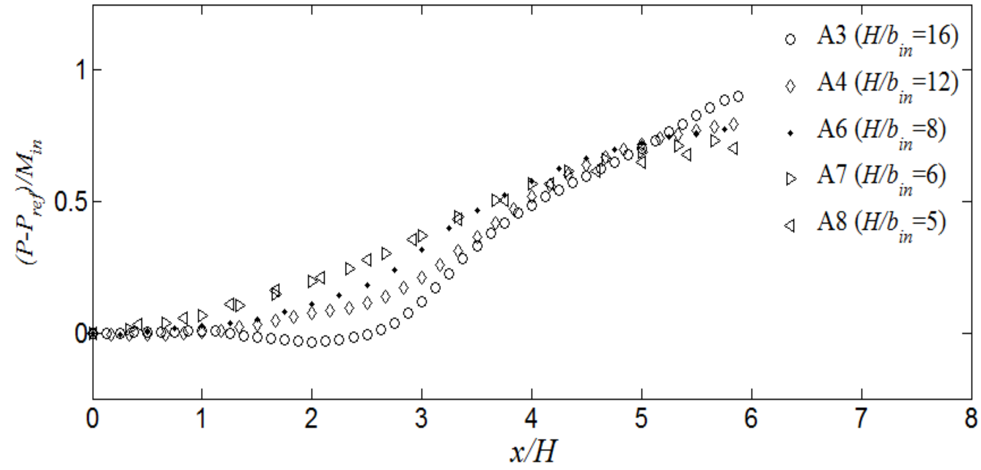

Figure 3.8: Normalized pressure integral of region I and II for various H/b_{in} ratio.

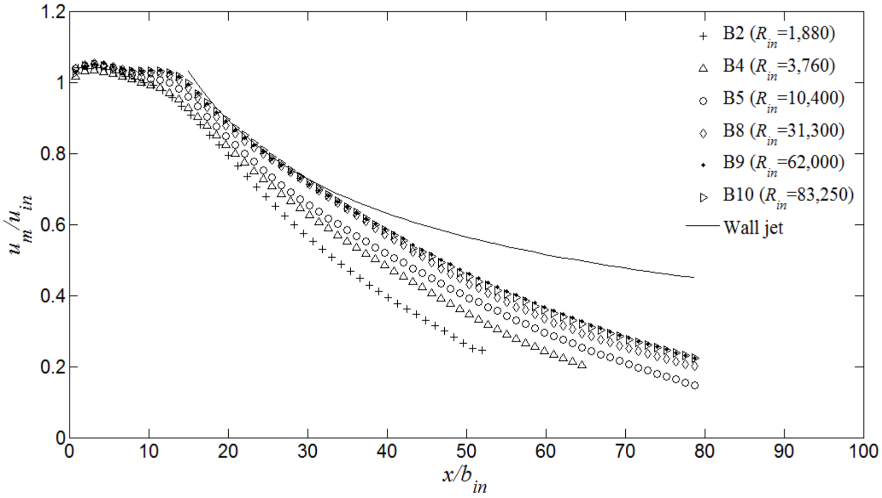

Figure 3.9: Maximum velocity profiles for different inlet Reynolds number at $H/b_{in} \approx 14$.

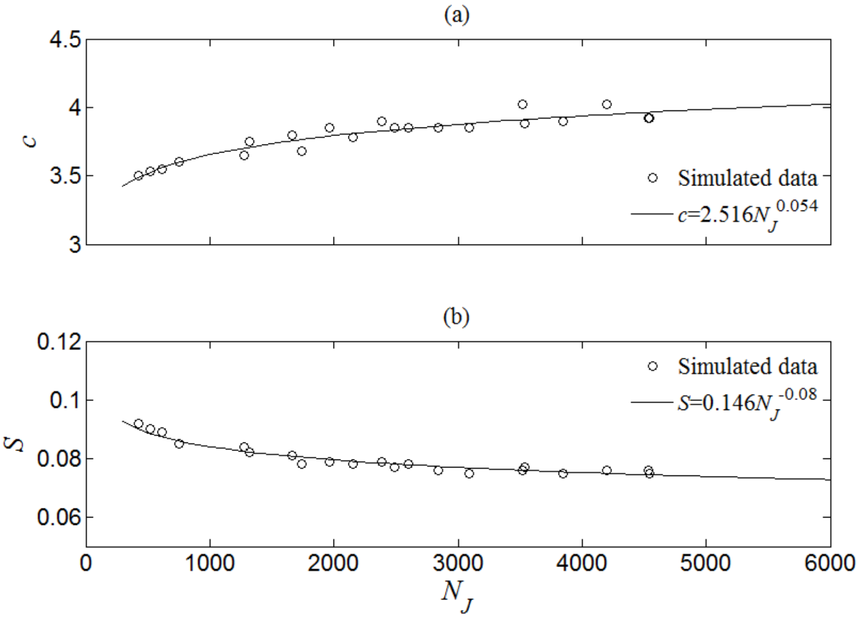

Figure 3.10: Variation of the velocity decay coefficient and the jet spreading rate with $N_J (= R_{in}^{1/2} H / b_{in})$.

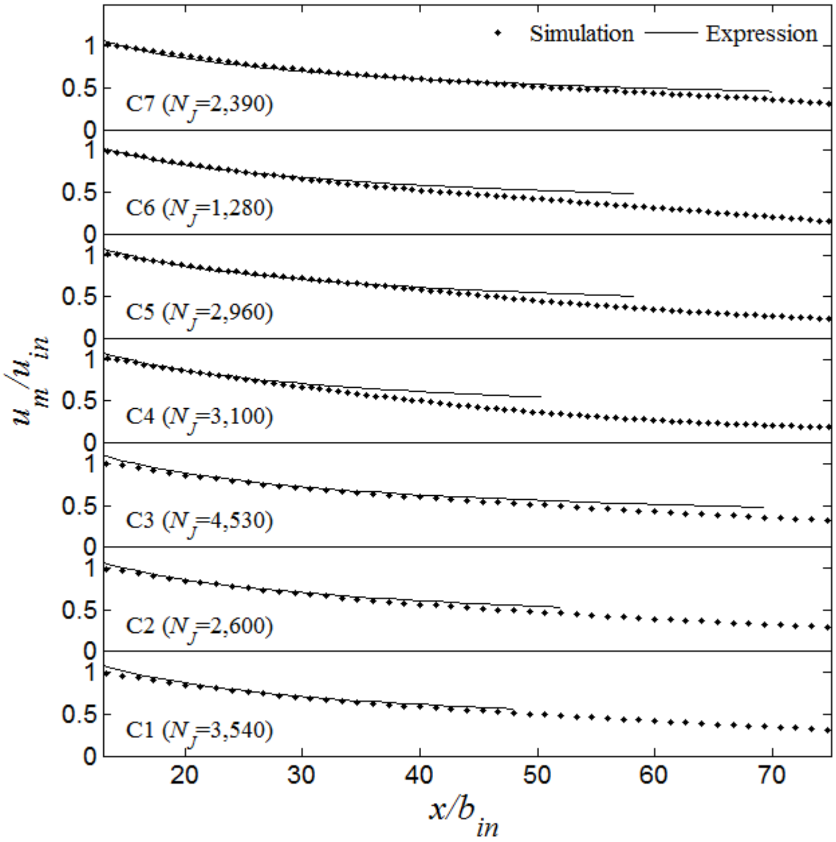

Figure 3.11: Comparison between simulated and empirical u_m profile.

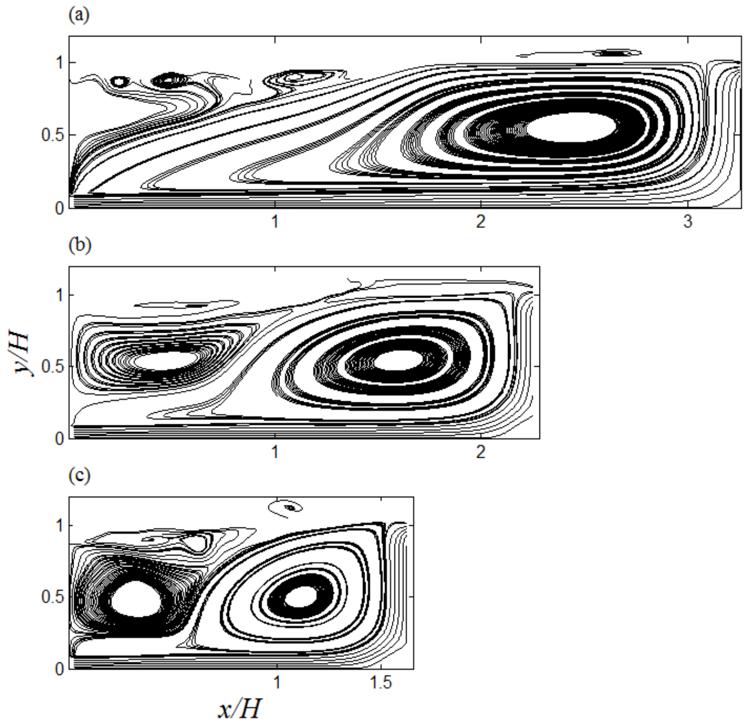

Figure 3.12 : Effect of length scale on wall jet behavior.

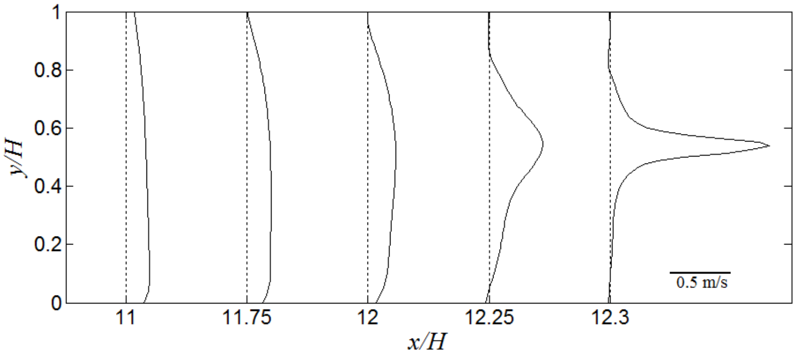

Figure 3.13: Flow upstream of the line intake located at mid-depth.

Chapter 4

Flow Upstream of Two-Dimensional Intakes[3]

4.1 Introduction

Analyzing flow upstream of intakes is important in many engineering applications, e.g., fish entrainment study, flow in sedimentation tank, flow induced by sluice gates, skimmer wall, and temperature control curtain (Gerges and McCorquodale, 1997; Shammaa and Zhu, 2010). Upstream of the intake, flow is accelerated and identifying the acceleration zone is important to design fish repulsion systems. To our knowledge, no comprehensive information is available in literature to the extent of the flow acceleration region and on how intake location, its size, and flow rate can affect this region. Flow acceleration region for multiple intakes is also an area of interest to explore. The primary

---

[3] A version of this chapter has been accepted in ASCE's Journal of Hydraulic Engineering.

objective of this study is to assess the flow acceleration region under various geometric and flow conditions and to analyze the interaction of multiple intakes. To fulfill these objectives, the Schwarz-Christoffel (S-C) transformation based model is applied in generating the flow field considering its reliability and computational simplicity in such applications.

The theoretical description of the S-C transformation in predicting the flow upstream of a line sink located at a two dimensional rectangular duct is available in hydrodynamics references, e.g. Vallentine (1967). However, this classical approach is applicable only when sink is located at the mid-depth or at the corner of the duct. This study upgraded this method to change the sink location to any depth in the duct. This upgraded method is used in the detailed flow analysis. This study also applied the S-C transformation for predicting flow upstream of two dimensional nozzle shaped intakes.

Other methods are also available in literature. Shammaa et al. (2005) integrated line sink equation to apply to the finite depth intake and added images to account for boundaries. Bryant et al. (2008) showed that multiple orifices can be modeled by superposition of individual orifice equations. Montes (1997), Vanden-Broeck (1997), and Hocking and Forbes (2000)'s approach is focused on numerical computation of the free surface profile. Belaud and Litrico (2008) developed a closed form solution to predict flow upstream of a contracted flume. Dias et al. (1980) solved nozzle intake using numerical conformal mapping technique.

4.2 Theoretical Development

A classical solution applying Schwarz-Christoffel transformation to obtain flow field upstream of a line sink located at the mid-depth or at the corner of a two-dimensional duct is available in literature (Vallentine, 1967). The geometry of a two dimensional water intake is shown in Figure 4.1, where *h* is the depth of water, *b* is the distance of line sink from the bottom, *d* is the size of the intake opening, and *q* is the flow-rate per unit width. The S-C based solution is applicable when $b = h/2$ and $d = 0$ which follows a two-step procedure. First, *z*-plane (*x*+*iy*) is transformed to *t*-plane using the relationship,

$$t = i \sinh \left(\frac{\pi z}{h} \right)$$

Equation 4.1

The *t*-plane to *w*-plane $(\varphi + i\psi)$ transformation is as follows,

$$w = -\frac{q}{\pi} \ln(t)$$

Equation 4.2

Substituting Equation 4.2 into Equation 4.1, and after algebraic simplification, the velocity potential comes out as,

$$\varphi = -\frac{q}{2\pi} \ln\left[\frac{1}{2}\left(\cosh\frac{2\pi x}{h} - \cos\frac{2\pi y}{h}\right)\right]$$

Equation 4.3

This equation inherently adds infinite number of sinks located at distance $\pm nh$ ($n = 1,2,3,...\infty$) from the mid-depth of the duct, and thereby boundary effect is accounted for without adding any image sinks.

Above solution is applicable only for a line sink located at mid-depth of the duct. Taking the upper-half (or lower-half) of the duct, the solution can be applied for a line sink located at the bottom (or the top) of the duct. However, for any other locations the solution does not work. The objective of this study is to overcome this limitation and to apply line sink solution to the intake having large opening. To do that, first the origin is shifted to the channel bottom from the mid-depth of the channel using the conventional procedure,

$$w = -\frac{q}{\pi}\ln\left[\cosh\frac{\pi}{h}(z-b')\right]$$

Equation 4.4

where, $b' = b - h/2$, or distance from the line sink to the channel mid-depth. Thereafter, the complex velocity (*dw/dz* = *u-iv*) is derived as,

$$u - iv = -\frac{q}{\pi}\tanh\frac{\pi}{h}(z-ib')$$

Equation 4.5

After algebraic manipulation, the expressions for *u* and *v* velocity components come out as,

$$u = -\frac{q}{h}\left[\coth\left(\frac{\pi x}{h}\right)\cos^2\left\{\frac{\pi(y-b')}{h}\right\} + \tanh\left(\frac{\pi x}{h}\right)\sin^2\left\{\frac{\pi(y-b')}{h}\right\}\right]^{-1}$$

$$v = \frac{q}{h}\left[\cosh^2\left(\frac{\pi x}{h}\right)\cot\left\{\frac{\pi(y-b')}{h}\right\} + \sinh^2\left(\frac{\pi x}{h}\right)\tan\left\{\frac{\pi(y-b')}{h}\right\}\right]^{-1}$$

Equation 4.6

This equation only shifts the origin towards the channel bottom and is valid when sink is located at the mid-depth $(b \neq h/2)$. This equation inherently adds infinite number of images located at $\pm nh$, ($n = 1,2,3,\ldots\infty$) distance from the sink location.

When $b \neq h/2$, images should be located at, $-2b, 2b'', -2b-2b'', 2b+2b'', -4b-2b'', 2b+4b'', -4b-4b'', 4b+4b'', \ldots$ etc., where, $b'' = h-b.$

This study found that, this image pattern can be achieved by adding two sinks; one located at distance *b* from the channel bottom, and the other located at distance -*b* from the channel bottom. For both sinks, the water depth is to be 2*h*, instead of *h*. The *u*-velocity obtained from these sinks are,

$$\frac{u_1}{U_\infty} = -\frac{1}{2}\left[\coth\left(\frac{\pi x}{2h}\right)\cos^2\left\{\frac{\pi(y-b_1')}{2h}\right\} + \tanh\left(\frac{\pi x}{2h}\right)\sin^2\left\{\frac{\pi(y-b_1')}{2h}\right\}\right]^{-1}$$

$$\frac{u_2}{U_\infty} = -\frac{1}{2}\left[\coth\left(\frac{\pi x}{2h}\right)\cos^2\left\{\frac{\pi(y-b_2')}{2h}\right\} + \tanh\left(\frac{\pi x}{2h}\right)\sin^2\left\{\frac{\pi(y-b_2')}{2h}\right\}\right]^{-1}$$

$$u_t = u_1 + u_2$$

Equation 4.7

where, $b_1' = b-h$, $b_2' = -b-h$, $U_\infty = q/h$ and u_t is the total *x*-directional velocity.

In order to derive the velocity-field for an intake having large opening, one needs to integrate u_t over the opening using the following relationship,

$$U = \frac{1}{d}\int_{j=b}^{j=b+d} u_t(j)\,db$$

Equation 4.8

where, *d* is the intake opening and *j* varies from *b* to (*b*+*d*), and u_t is a function of *j*, *x*, and *y*. Following the similar procedures, integral equation for vertical velocity *V* can also be computed.

An Analytical solution is also developed using Schwarz-Christoffel transformation for a non-rectangular intake or nozzle as shown in Figure 4.2. For the nozzle having interior angle α, the *z-t* transformation can be derived by solving the following integration,

$$z = A\int \frac{dt}{(1-t)^{-(1-\alpha/\pi)}} + B$$

Equation 4.9

Considering, at z=0, t=1, and at z=l_x, t=0, yields B=0, and Therefore, Equation 4.9 becomes,

$$z = \frac{\alpha l_x}{\pi}(1-t)^{\alpha/\pi}$$

Equation 4.10

The *w-t* relationship should be as follows,

$$w = -\frac{q}{\pi}\ln(t-1)$$

Equation 4.11

Substituting *t-z* relationship obtained from Equation 4.10 into Equation 4.11, and after some algebraic simplifications, the expressions for u and v come out as,

$$u = -\frac{q}{\alpha}\frac{x}{\left(x^2+y^2\right)} \quad \text{and} \quad v = -\frac{q}{\alpha}\frac{y}{\left(x^2+y^2\right)}$$

Equation 4.12

If the nozzle intake opening is large, the sink solution can be used by shifting the sink location upstream at distance equal to $d/(2\tan\alpha/2)$ as shown in Figure 4.2b.

4.3 Verification

Flow upstream of a two-dimensional intake is simulated using a computational fluid dynamic (CFD) package, ANSYS CFX (www.ansys.com), and the predicted result using Equation 4.8 is compared with the simulated result. The potential flow result is also compared with experimental data of Roth and Hager (1999). It should be pointed out that, a CFD solver is designed for real fluid and considers viscosity, turbulence, boundary layer formation, etc., while potential flow theory does not account for those. For the case of the flow upstream of a circular orifice, Anayiotos et al. (1995) found excellent agreement between the experimental data and numerical calculation, and therefore numerical solvers can be considered as a reliable tool in similar applications. The CFD solver used in the present study solves three-dimensional Navier-Stokes equation with Launder and Spalding (1974)'s $k-\varepsilon$ turbulence model. The free surface and side-walls were modeled as a free-slip wall. The channel bottom is modeled as a no-slip wall, where standard wall function is used. The solver applies unstructured mesh and central difference scheme for discretization of governing equations. The intake opening (d) is provided as 8 cm, and water depth (h) as 53 cm. The upstream boundary is located at 2 m upstream from the intake. The flow rate per unit width (q) at both the inflow and outflow boundary is provided as 1,750 cm^2/sec.

Figure 4.1 shows the schematic diagram of the model geometry and coordinate axes. Figure 4.3 shows the comparison between the theoretical, simulated and experimental (Roth and Hager, 1999) velocity profiles upstream of the intake located at $b=0$. This figure shows satisfactory agreement between the three. The theoretical profile successfully shows mean velocity ($=q/h$) at far upstream of the intake without adding any images. However, flow field developed by the potential flow model does not show up corner eddy as described by Roth and Hager (1999) upstream of the sluice gate, and boundary layer at channel bottom.

The potential equation for non-rectangular nozzle intake with large opening is also compared with the CFD result. In this simulation, q=500 cm^2/s, d=10 cm, and $\alpha = \pi / 3$ are used. The comparison between the theoretical and simulated result is shown in Figure 4.4.

4.4 Flow Analyses

For a line-sink in a half-space without boundaries, the u-velocity can be found in most of the fluid mechanics textbooks,

$$u = -\frac{q}{\pi} \frac{x}{\left(x^2 + y^2\right)}$$

Equation 4.13

If one substitutes $\alpha = \pi$ in the nozzle intake solution (Equation 4.12), it becomes equal to the line sink solution for unbounded domain in half-space (Equation 4.13). Therefore, the line-sink geometry in half-space (Equation 4.13) can be imagined as a nozzle having interior angle, $\alpha = \pi$. The velocities at any point inside the nozzle intake will be π / α times larger than the corresponding velocity in unbounded line sink in half space.

To account for the boundary, Shammaa et al. (2005) applied image sinks. This study found that the image method in this application underestimates velocity at x_∞, and number of images required to minimize the underestimation depends on the distance from the intake. Figure 4.5 shows that, with 50 images, underestimation at x=2h is only 5%, however at distance x=10h, the underestimation is 25%. With applying 150 images (Figure 4.5), the underestimation at x=10h is found 8%; however, at x=20h, the underestimation remains 15%. Hence, the greater the distance from the intake, the higher the number of images required to keep underestimation within a limit. These images are applied at a distance $\pm nh$ from the channel mid-depth, where n=1,2,3,…, and the sink is located at channel mid-depth. For practical interest, U_∞ can be estimated using q/h and near-intake flow field ($x \leq 2h$) can be estimated with 50 images to limit error within 5%.

Flow acceleration region is the region where flow starts to accelerate due to the influence of an intake. Identifying this region is of interest in designing fish-repulsion system. For a line sink located at channel bottom, the acceleration region can be identified by substituting $U = - q/h$ and $y = b$ in Equation 4.7 and solving for x, which yield $x = \infty$. Hence, mathematically flow starts to accelerate at infinite distance upstream of the intake. However, for practical interest, one needs to describe the extent of the acceleration region. This study defines the acceleration region as the distance x_a where x-directional velocity is 1% more than the average channel velocity, i.e. U = -1.01q/h, Substituting this value in Equation 4.7, and solving for x_a will yield,

$$x_a = \frac{2h}{\pi}\coth^{-1}(1.01) \quad \text{or} \quad 1.7\text{h}$$

Equation 4.14

When the sink is located at distance $h/2$ from the channel bottom, x_a is computed as 1.7(h/2). This is half of the distance computed for the line sink located at bottom. Figure 4.5 shows that flow starts to accelerate from this distance. Hence, acceleration region is a function of water depth as well as distance of line sink from the channel bottom. It is also observed that all u velocity profiles along intake centerline collapses to a single curve when normalized by intake velocity ($U_s = q/d$) and water depth (h) at all flow-rates (q). Hence, flow acceleration region does not depend on the velocity at intake. Shammaa et al. (2005) found that flow is nearly uniform at distance 1.5h upstream of the line sink. However, dependency of the location of sink was not explored and no theoretical justification was provided. Figure 4.6 shows the effect of intake opening for d/h =0.04, 0.07, 0.1, 0.2, and 0.5 while keeping other parameters as, h = 50 cm, q =50 cm^2/s. A line sink solution using Equation 4.7 is added in this figure. Far from the intake, velocity approaches to $U_\infty = q/h$ while near the intake velocity increases with decreasing d. The line sink solution shows very similar profile with finite opening intake as long as d/h<0.07. For larger d/h value, velocity profiles are still considerably similar to the line sink profile when x/h>0.5. Figure 4.7 shows the iso-velocity lines (1.01q/h) upstream of the intake located at the mid-depth for different d/h ratios. These lines demarcate the flow-acceleration region for a particular d/h ratio. It is observed that iso-velocity lines shift closer to the intake location with increasing d/h ratio. Therefore, flow acceleration region is also affected by d/h ratio. However, it is observed that the effect of d/h ratio is negligible as long as $d/h \le 0.3$. Hence, the acceleration region derived from sink solution can be applied to the intake having d/h ratio up to 0.3 with reasonable accuracy. For d/h=0.5 velocity computed using CFD solver is added as a validation, and both potential flow velocity and CFD derived velocity shows excellent agreement.

To investigate the effect of intake location, the location was varied in five different positions, where intake centerlines (b_c) were located at distances 0.1h, 0.2h, 0.3h, 0.4h and 0.5h from the channel bottom, respectively. In all cases, d=10 cm, q=50 cm^2/s, and h=50 cm. Figure 4.8 shows the theoretical and simulated velocity profile upstream of the intake for b_c/h=0.2, which reflects good agreement. The circles on these profiles show the location of U_{max}. It is interesting to note that the trajectory of U_{max} does not follow the intake center-line in this case. It heads towards the intake center-line from the channel bottom. The CFD shows similar trajectory, except the peak does not lie exactly on the channel bottom due to the formation of the boundary layer.

Figure 4.9 shows the normalized centerline velocity with longitudinal distances for all five intake levels. It is observed that by normalizing distances by h_m, all curves collapse to a single curve, where h_m is the larger distance from the intake centerline to the upper boundary or the lower boundary. Due to this normalization, all curves accelerate from the same location. Hence, acceleration region can be defined as 1.7h_m upstream from the intake. Water depth is varied in these cases, and it is observed that flow starts to accelerate at a distance 1.7h_m from the intake for other water depths as well.

Although potential flow model does not consider the effects of viscosity and flow turbulence, its agreement with CFD computation warrantees some discussion. This study changes several parameters of the numerical solver, and excellent agreement between the CFD solver and potential flow model is found for all the parameters tested. Two different turbulence models ($k-\varepsilon$ and shear stress transport), two different turbulence intensities at the inlet (*I*=1% and 5%), and two different upstream Reynolds numbers (*R*=5,000 and 25,000) are tested. The upstream Reynolds number is computed using $U_\infty h/\nu$, where ν is the kinematic viscosity of water. In these simulations, b_c/h=0.5 and d/h = 0.2 are used. Figure 4.10 shows the normalized *U* velocity profile along the intake center-line for all these simulations and a profile obtained using potential theory. Excellent agreement between all the simulations and theoretical profile is noticeable. This study attempts to find the possible reason behind the agreement. Figure 4.11 shows the normalized momentum-flux (*M*) and pressure integral (*P*) upstream of the intake. These parameters are calculated as,

$$\frac{M(x)}{M_\infty} = \frac{1}{M_\infty}\int_{y=0}^{h} \rho U^2(y)dy$$

$$\frac{P(x)}{M_\infty} = \frac{1}{M_\infty}\int_{y=0}^{h} p(y)dy$$

Equation 4.15

Where, *p(y)* and *U(y)* are the pressure and velocity at depth *y* located at *x*, M_∞ is the momentum-flux at far from the intake which is computed as $\rho U_\infty^2 h$. Figure 4.11 shows that close to the intake, momentum-flux increases due to the decrease in pressure integral. It is calculated that increase in momentum flux is 97.5% of the decrease in pressure integral. Therefore, Reynolds stresses and viscous forces take only 2.5% of the pressure integral. Potential flow model does not consider Reynolds stresses and viscosity effect. As these forces are negligible compare to the pressure integral, CFD solver and potential flow model show excellent agreement. For flow upstream of orifice, CFD solver and experiments showed excellent agreement (Anayiotos et al., 1995) and therefore, CFD result can be considered as reliable.

4.5 Multiple Intakes

Figure 4.12a shows flow upstream of two symmetric intakes with the same flow-rate. The circular marker shows the location of maximum velocity at each profile. The key observation is that, at x/h=1, the maximum velocity is located along the symmetry plane, and the velocity profiles show one single peak. At x/h=0.2, two peaks show up and each head towards one of the intake location. If one takes the upper-half portion of the space, flow-pattern is found to be similar to the pattern observed in Figure 4.8. Flow is accelerated at a distance of 1.7h_m , where h_m is the distance from the intake centroid to the upper surface or symmetry plane, whichever is larger. Similar computation can be carried out for the lower intake. This potential flow result is compared with the CFD computation, and excellent agreement is observed (Figure 4.12a). Another case is considered where the two intakes are located close to the upper and lower surfaces, rather than to the plane of symmetry. Figure 4.12b shows the velocity profile obtained for such a case.

Unlike the previous case, two peaks existed at the upper and lower surfaces at *x/h* = 1, and these peaks headed towards the intakes. The lower-half portion shows similar pattern as observed in Figure 4.8. In fact, image intake is located below the lower surface, and this pair of image intake and real intake pulled the peak at the lower-surface. The similar system occurred for the upper intake. In the previous case, the two real intakes pulled the peak along the symmetry plane, as they are close to each other compare to their images. The acceleration region can be predicted following the similar procedure as discussed in the previous paragraph.

If these two sets of intakes are combined, it can be seen from Figure 4.12c that only one peak exists at *x/h*=1 located at the symmetry plane. Thereafter, this peak is splitted at *x/h*=0.2 and each peak is located close to the mid-depth of each intake-pair. Finally, very close to the intake, the splitted peaks re-splitted and headed towards each intake. If the distance between the two peaks located at *x/h*=0.2 were greater than their image counterpart, they would merge with their image peaks at *x/h*=1, and would attach to the top and bottom surfaces, instead of merging on the symmetry plane. The closest peaks first merge together, thereafter the closest merged-peaks re-merged with each other, and this process continues until the distances between the merged peaks at a section are the same.

It is interesting to note that the upper peak at *x/h* = 0.2 (Figure 4.12c) does not lie at the mid-depth of the intake-pair; rather it is slightly shifted towards the symmetry plane. The reason is that, the upper peak at *x/h*=0.2 is pulled by the real intake-pair located below the symmetry plane as well as by the image intake-pair located above the top surface. As this real intake-pair is closer from the peak compared to the image intake-pair, the peak is shifted towards this real intake-pair. In other words, this peak is located at the centroid of these three intake-pairs. If the flow-rate is changed, this centroid is found to be shifted upward or downward. If it shifts upward, the merged peak can be closer to the image peak located above the surface compared to the real merged peak located below the symmetry plane. Therefore, final location of the peak can be attached to the top or bottom surface.

4.6 Conclusions

This study enables classical Schwarz-Christoffel (S-C) transformation based line sink solution (Vallentine, 1967) to be applied for two dimensional intakes having variable locations. The S-C transformation is also applied in the case of a flow upstream of two dimensional nozzle intakes. Flow upstream of the intake is accelerated. It is shown that flow starts to accelerate at a distance $1.7h_m$, where h_m is the larger distance from the line sink to the top or bottom boundary. This prediction for line sink also works well for intake having finite size (d) as long as $d/h \leq 0.3$. It is shown that the acceleration region depends on water depths, location of intake, and size of the intake opening (d), and does not depend on flow rates.

It is observed that flow profiles upstream of multiple intakes are affected by the relative distances between intakes and boundaries as well as flow rates of each intake. Upstream of intakes, the velocity peak induced by each intake merges with each other in a systematic manner, which can be explained by analyzing the distances between intakes. Methods to compute acceleration region for multiple intakes are also explained.

It is shown that line sink in half-space without boundaries can be imagined as a nozzle intake having interior angle (α) equal to 180°. Velocity in such nozzle intake can be computed from unbounded half-space line sink velocity by multiplying by π / α.

4.7 References

Anayiotos, A.S., Perry, G.J., Myers, J.G., Green, D.W., Fan, P.H., Nanda, N.C., (1995), A numerical and experimental investigation of the flow acceleration region proximal to an orifice, Ultrasound in Med. and Biol., 21(4), 501-516.

Belaud, G., and Litrico, X., (2008), Closed form solution of the potential flow in a contracted flume, Journal of Fluid Mechanics, 599, 299-307.

Bryant, D.B., Khan, A.A., and Aziz, N.M., (2008), Investigation of flow upstream of orifices, Journal of Hydraulic Engineering, 134(1), 98-104.

Dias, F., Elcrat, A.R., Trefethen, L.N, (1980), Ideal jet flow in two dimensions, Journal of Fluid Mechanics, 185, 275-288.

Gerges, H., and McCorquodale, J.A., (1997), Modelling of flow in rectangular sedimentation tanks by an explicit third-order upwinding technique, International Journal for Numerical Methods in Fluids, 24, 537-561.

Roth, A., and Hager, W.H., (1999), Underflow of standard sluice gate, Experiments in Fluids, 27, 339-350.

Hocking, G.C., and Forbes, L.K., (2000), Withdrawal from a fluid of finite depth through a line sink including surface-tension effects, Journal of Engineering Mathematics, 38, 91-100.

Launder, B.E., and Spalding, D.B., (1974), The numerical computations of turbulent flows, Computer Methods in Applied Mechanics and Engineering, 3, 269-289.

Montes, J.S., (1997), Irrotational flow and real fluid effects under planar sluice gates, Journal of Hydraulic Engineering, 123(3), 219-232.

Shammaa, Y., and David, Z., (2010), Experimental study on selective withdrawal in a two-layer reservoir using a temperature-control curtain, ASCE Journal of Hydraulic Engineering, 136(4), 234-246.

Shammaa, Y., Zhu, D.Z., and Rajaratnam, N., (2005), Flow upstream of orifices and sluice gates, Journal of Hydraulic Engineering, 131(2), 127-133.

Vallentine, H.R., (1967), Applied Hydrodynamics, 2nd Edition, 201-202.

Vanden-Broeck, J.M., (1997), Numerical calculations of the free-surface flow under a sluice gate, Journal of Fluid Mechanics, 330, 339-347.

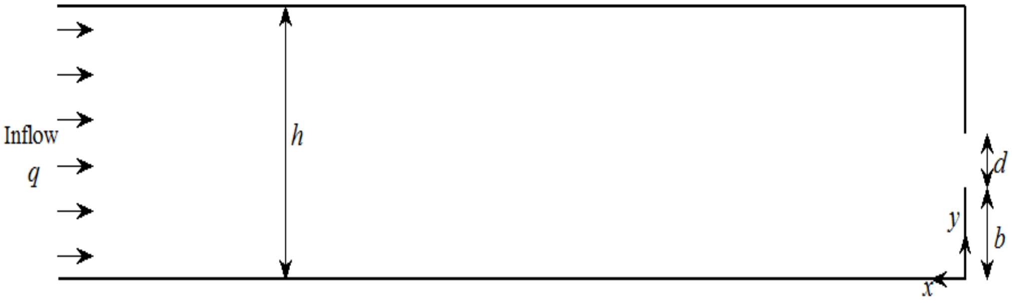

Figure 4.1: A 2D schematic side-view profile of the model geometry.

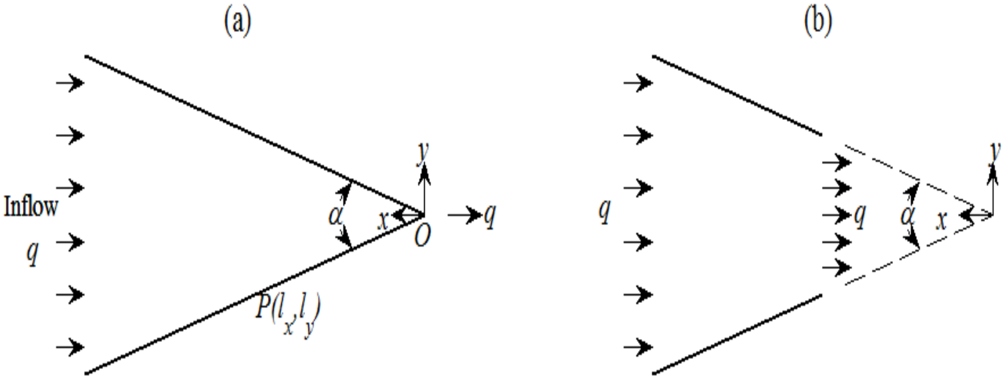

Figure 4.2: The nozzle intake geometry for (a) line opening, and (b) large opening.

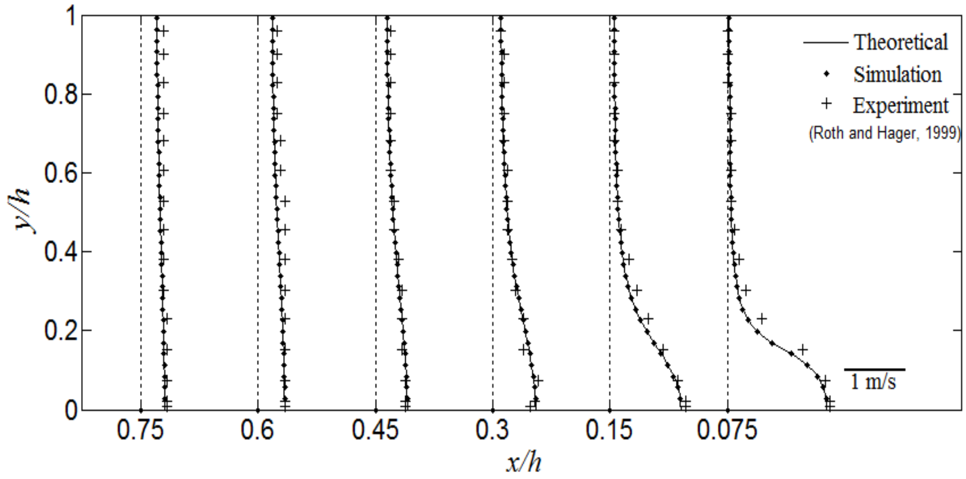

Figure 4.3: Theoretical, simulated, and experimental u-velocity profiles upstream of the intake.

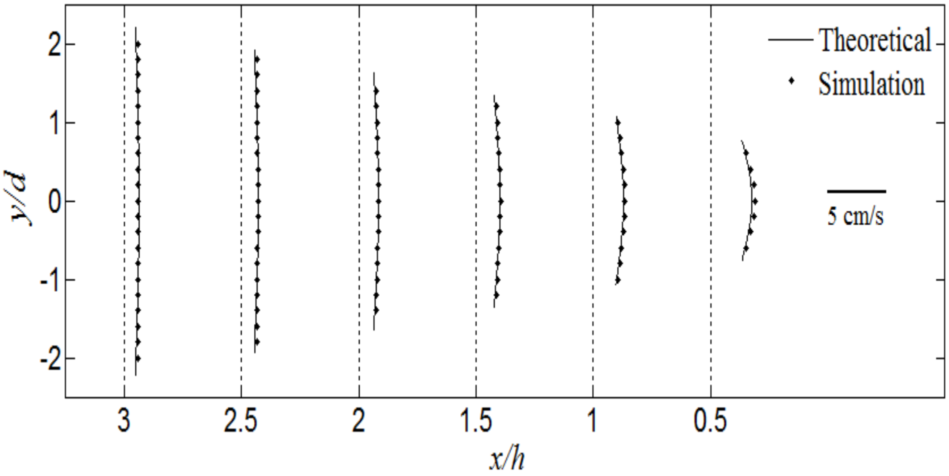

Figure 4.4: Theoretical and simulated velocity profiles for nozzle intake.

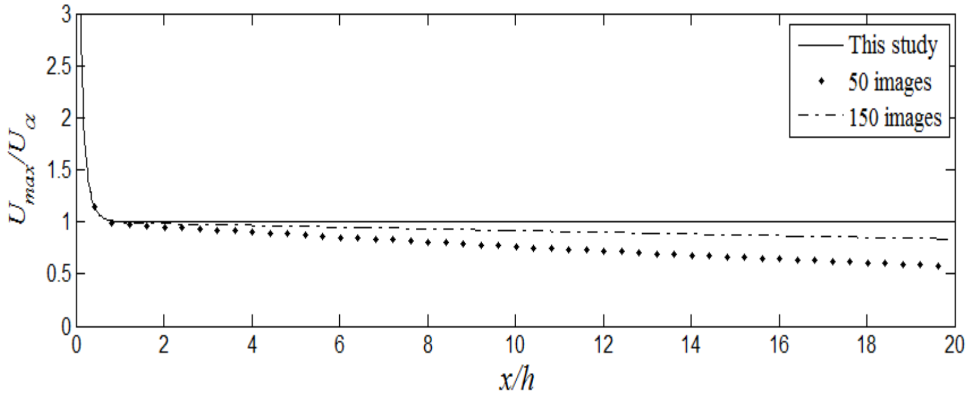

Figure 4.5: The maximum velocity profiles along intake centerline obtained using image methods and method developed in this study.

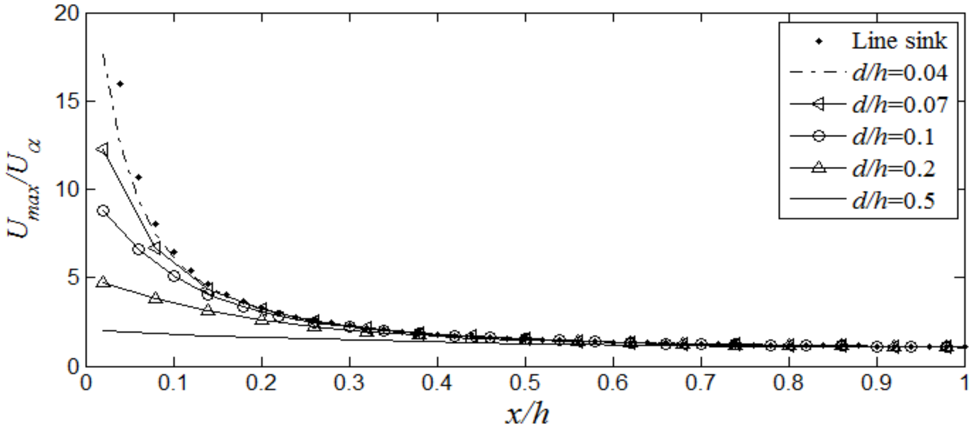

Figure 4.6: Normalized centerline u-velocity for different d/h ratios.

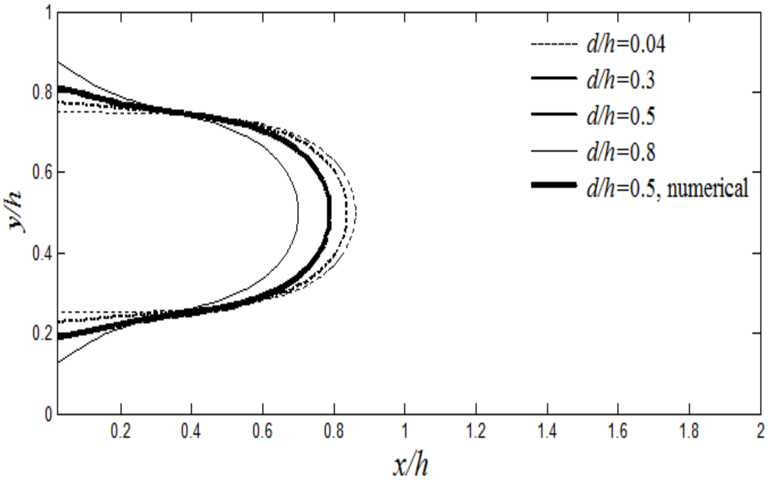

Figure 4.7: Iso-velocity lines upstream of the intake for different d/h ratios.

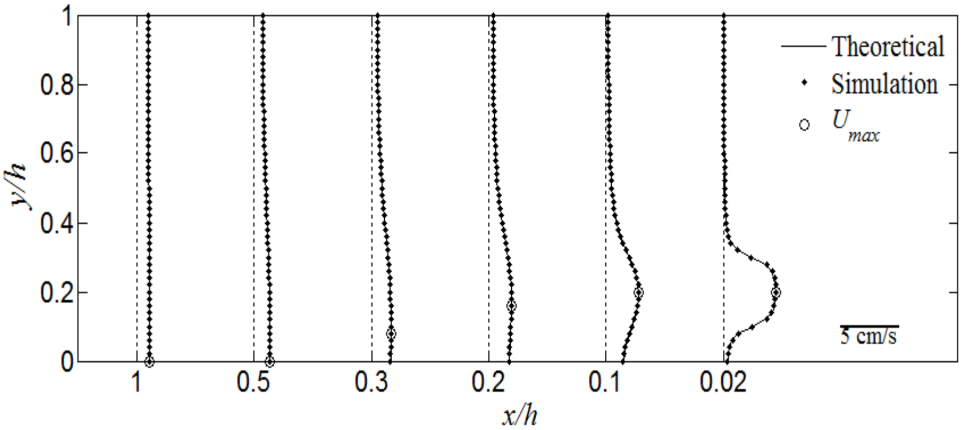

Figure 4.8: Theoretical and simulated u-velocity profiles for b_c/h=0.2.

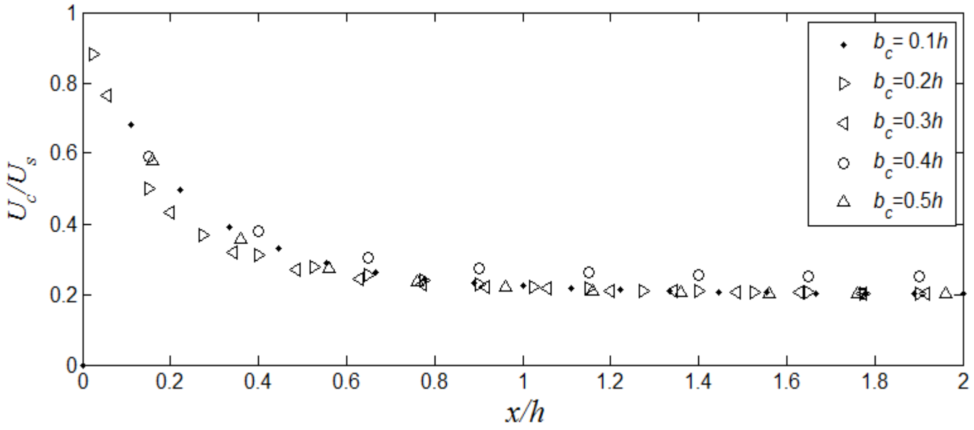

Figure 4.9: Normalized centerline velocity profiles for different intake levels.

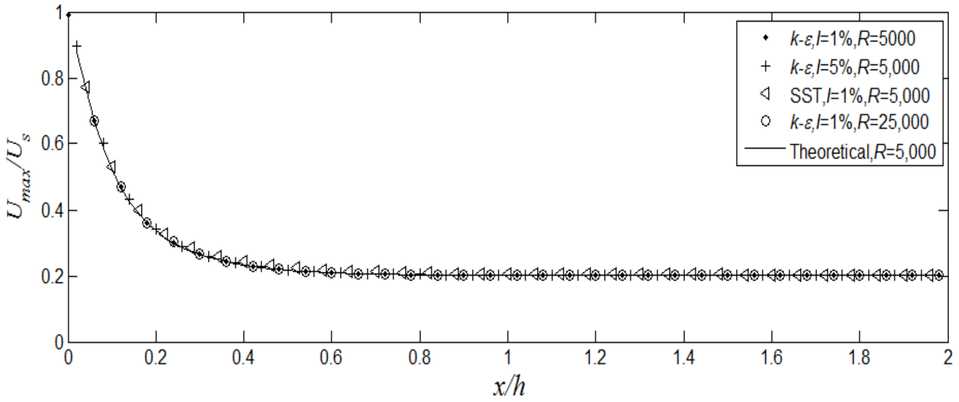

Figure 4.10: Comparison of numerical u-velocity profiles along intake centerline with varying parameters.

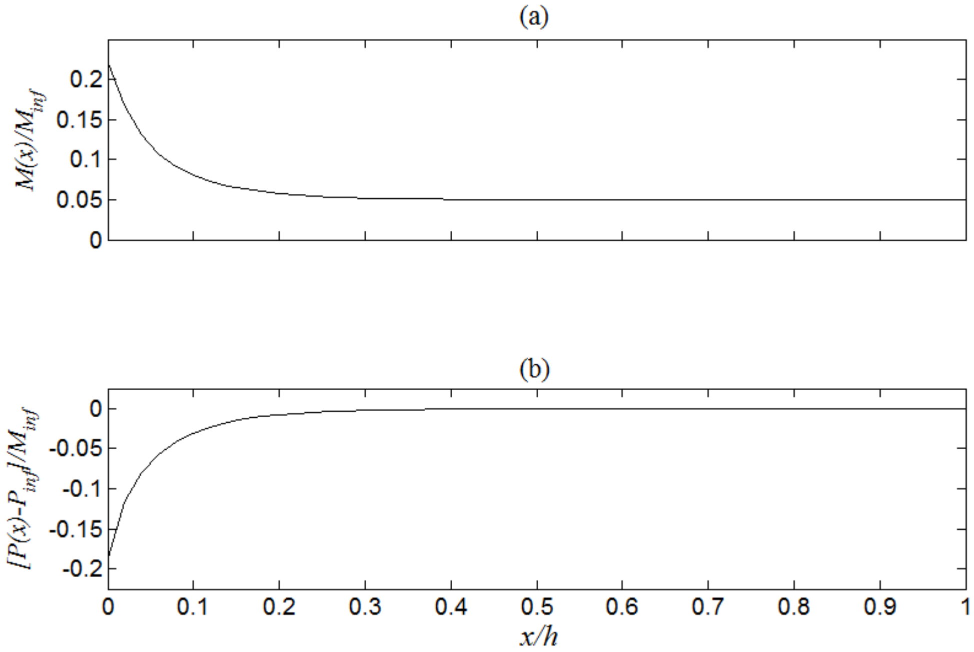

Figure 4.11: Normalized momentum-flux and pressure integral upstream of an intake.

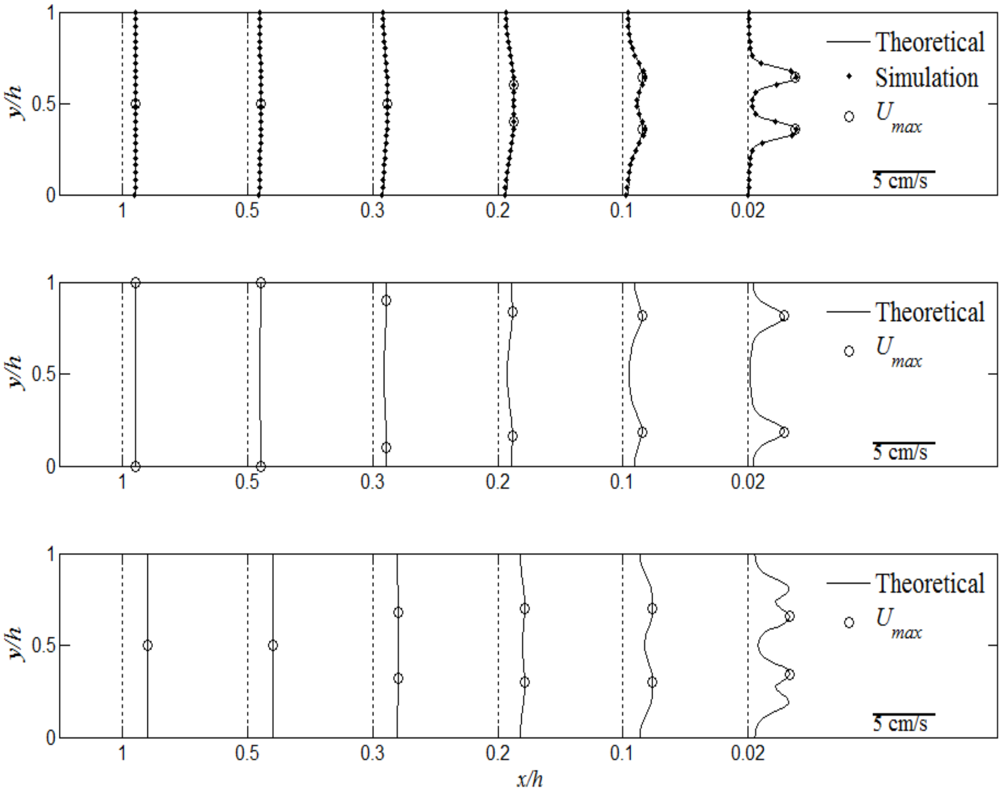

Figure 4.12: Velocity profiles upstream of multiple intakes located (a) close to the plane of symmetry, (b) close to the upper and lower boundaries, (c) combination of both.

Chapter 5

Selective Withdrawal with Two Dimensional Intakes

5.1 Introduction

During summer, lakes upstream of a dam can be stratified and density can vary with depth. Close to the surface, water can be warm and at the bottom it can be cold. If water is withdrawn from such a stratified reservoir, either the warm layer or the cold layer can be withdrawn depending on the location of an intake. This phenomenon is known as selective withdrawal. This study is focused on selective withdrawal for a line sink with discrete stratification. Understanding selective withdrawal with a line sink is important for flow upstream of temperature control curtains (Shammaa and Zhu, 2010), skimmer walls (Harleman and Elder, 1965), and so on. Craya (1949) developed a criterion to determine the maximum flow rate above which both layers will be withdrawn. This equation is valid when the lower boundary is located at infinity. Gariel (1949) verified Craya (1949)'s theory with experimental data. Theoretical and experimental works of Harleman and Elder (1965), Jirka (1979), and Wood and Lai (1972) are also based on withdrawing water from a reservoir of infinite depth. To-date no theoretical criterion has been developed to get the incipient withdrawal for an intake located at the horizontal bottom boundary. The primary objective of this study is to derive an expression for such a case.

Velocity distribution in the stratified withdrawal condition is not well-documented in the literature. The probable reason behind this may be associated with the difficulty in experimentally creating steady-state conditions in stratified withdrawal scenarios. Shammaa and Zhu (2010) used a PIV technique to retrieve the instantaneous velocity in an unsteady condition for a point sink. The computational fluid dynamics (CFD) model may provide quality information of velocity fields when one layer or both layers withdraw. Therefore, the second objective of this study is to assess the velocity field predicted by the CFD solver and to compare it with unstratified flow fields.

5.2 Background

Using the two layer Bernoulli's equation, Craya (1949) derived a densimeric Froude number (F) for discrete stratification,

$$F = \frac{q}{\sqrt{\frac{\Delta\rho}{\rho} g h^3}}$$

Equation 5.1

where, q is the flow rate per unit width, $\Delta\rho$ is the density difference, h is the depth of the interface measured from the intake level (Figure 5.1), and ρ is the density of the withdrawal layer. Craya (1949) derived that if $F \leq 1.72$ only one layer will be withdrawn from, otherwise both layers will be withdrawn. This situation can be created by changing q, h, or $\Delta\rho$. The maximum flow rate or the minimum water depth necessary to withdraw one layer only is known as 'critical flow rate' (q_c) and 'critical depth' (h_c). This study is not using 'critical' as a key-word as not to create confusion with the critical flow-rate and critical depth widely used for flow over a weir and other open channel flows. This study rather uses 'incipient flow rate' (q_i), 'incipient water depth' (h_i), and incipient Froude number (F_i) to describe the incipient conditions. It can be shown that these two flow-rates are related by $q_i = \pi q_c$. Gariel (1949) experimentally verified Craya (1949)'s equation, and found the incipient Froude number to be 1.525 instead of 1.72. Harleman and Elder (1965) derived the maximum discharge equation for the skimmer wall problem to withdraw from the lower layer, where upstream water depth was assumed to be infinite. Wood and Lai (1972)'s experiment is also based on withdrawal from an infinite depth reservoir with a contracted intake. Hocking (1991b) did an experiment from a bottom line sink in a draining condition. However, his experimental data showed a high degree of scattering due to large interfacial diffusion. It is noteworthy that the diffused interface may show a reduction in outlet density much before the actual draw-down is taking place.

A bunch of theoretical works are available to get the interface profile at a specific Froude number. These theoretical interface profiles are available both for infinite depth (Tuck and Vanden-Broeck, 1984) and for finite depth reservoirs (Hocking 1991a, Vanden-Broeck and Keller, 1987). These theoretical interfaces may take a stagnation type profile (Hocking and Forbes, 1991) or cusped shape profiles (Tuck and Vanden-Broeck, 1984) depending on the Froude number. The limitation of this approach is that it does not provide us any information on the incipient Froude number at which both layers start to be withdrawn from. Another limitation is that these approaches show large deviation from the experimental results. For example, Tuck and Vanden-Broeck (1984) obtained a unique cusp solution at $F = 3.56$ for an infinite depth reservoir, however Gariel (1949)'s experiment showed that both layer starts to be withdrawn at $F = 1.52$. Therefore the unique cusp solution obtained at $F = 3.56$ is not an indication of incipient drawdown. For the finite depth problem, it is possible to get the cusped solution for $F \geq 1$ to infinity (Hocking, 1991a). However, this does not tells us at which F incipient drawdown occurs or whether it occurs at $F \geq 1$. Hence, Craya (1949)`s work remains the only effective means to calculate the incipient drawdown to-date.

Before withdrawal, a 'stagnant' type interface turns to a cusped shape. It can be derived that the water depth above the intake (y_s) is 2/3 of the upstream water depth (h) above the intake for an infinite depth reservoir. This derivation assumes that the upstream velocity is negligible, which is only possible when the upstream water depth is very large. If the bottom boundary is horizontal, and the intake is located at the bottom, this assumption is no longer valid and the '2/3' law is no longer applicable. This is perhaps the reason behind that no solution is available for incipient Froude number for an intake located at the horizontal bottom boundary. One objective of this study is to develop a theoretical expression for this mathematically intractable problem. No information is available in the literature on the velocity field for withdrawal from a single layer or both layers. Identifying the velocity field is important for fish entrainment studies. The second objective of this study is to explore the velocity field induced by the stratification.

To fulfill these objectives, this study uses a Computational Fluid Dynamic (CFD) solver. The CFD solver is validated by the theoretical works of Craya (1949) and experimental works of Gariel (1949) for the non-bottom case. It should be mentioned that the CFD solver was found to be reliable for the intake problems with unstratified flow (Islam and Zhu, 2010).

5.3 Numerical Model

The numerical model solves the unsteady multiphase three dimensional Reynolds Averaged Navier-Stokes equations with the curvature modified $k-\varepsilon$ turbulence model to assess eddy viscosity. The solver uses unstructured tetrahedral meshes with central difference advection scheme. The governing equation of the flow solver for phase a is,

$$\frac{\partial r_a \rho_a}{\partial t} + \frac{\partial r_a \rho_a u_j}{\partial x_j} = 0$$

$$\frac{\partial r_a \rho_a u_i}{\partial t} + \frac{\partial r_a \rho_a u_j u_i}{\partial x_j} = -\frac{\partial p}{\partial x_i} + \frac{\partial}{\partial x_j}\left\{(\mu + \mu_t)\left(\frac{\partial u_i}{\partial x_j} + \frac{\partial u_j}{\partial x_i}\right) - \frac{2}{3}\rho_a k \delta_{ij}\right\} + \left(\rho_a - \rho_{ref}\right) g_i$$

Equation 5.2

where, ρ_a is the density of phase a, r_a is the volume fraction of phase a, k is the turbulent kinetic energy, δ_{ij} is the Kronecker delta, p is the pressure, and μ_a is the molecular viscosity of phase a. Another set of RANS equation need to be solved for phase b. The transport equation for volume fractions are,

$$\frac{\partial r_a}{\partial t} + u_j \frac{\partial r_b}{\partial x_j} = 0$$

$$r_b = 1 - r_a$$

Equation 5.3

Turbulence was assumed to be homogenous and the transport equations are,

$$\frac{\partial \rho k}{\partial t} + \frac{\partial \rho k u_j}{\partial x_j} = \frac{\partial}{\partial x_j}\left\{\left(\mu + \frac{\mu_t}{\sigma_k}\right)\frac{\partial k}{\partial x_j}\right\} + fP_k - \rho\varepsilon - \frac{\mu_t}{\sigma_\rho \rho} g_i \frac{\partial \rho}{\partial x_i}$$

$$\frac{\partial \rho \varepsilon}{\partial t} + \frac{\partial \rho \varepsilon u_j}{\partial x_j} = \frac{\partial}{\partial x_j}\left\{\left(\mu + \frac{\mu_t}{\sigma_\varepsilon}\right)\frac{\partial \varepsilon}{\partial x_j}\right\} + C_1 \frac{\varepsilon}{k} P_k - C_2 \rho \frac{\varepsilon^2}{k}$$

$$\mu_t = \rho C_\mu \frac{k^2}{\varepsilon}$$

$$\rho = r_a \rho_a + r_b \rho_b$$

$$\mu = r_b \mu_b + r_a \mu_a$$

Equation 5.4

where, μ_t is the eddy viscosity, and P_k is the production of turbulence. Standard values for the model constants, which were used are: C_1=1.44, $C_2 = 1.92$, σ_k =1.0, $\sigma_\varepsilon = 1.3$, and $C_\mu = 0.09$. In the buoyancy production term, σ_ρ= 2 is used. The curvature corrected $k - \varepsilon$ model multiplies P_k by a factor (*f*), to account for the streamline curvature. The detail formulation to estimate *f* is given by Spalart and Shur (1997).

The numerical model geometry is shown in Figure 5.1. It's length (L) is 1.8 m, height (H) is 0.4 m and the outlet level (b) varies. A complete description of all the simulations carried out is given in Table 5.1. The flow-rate (q) increases slowly until the incipient drawdown occurs. This flow-rate is tabulated as the incipient flow-rate for a given interface height (h). The flow-rate was increased at the rate of 2e-5 m^2/s^2. At such a low gradient of flow rate, no wave activity was observed on the interface. An average grid spacing of 2.5 mm was used in the domain and local refinement was provided at the intake location. With this grid spacing, the interface thickness was kept within 1 cm and the location of average density was considered the location of interface.

5.4 Validation

All simulations carried out were compared with Gariel (1949)'s experimentally determined incipient Froude number. Series A (Table 5.1) shows numerical incipient Froude number at different distances from the channel bottom. It was observed that the numerical solver can predict the Gariel (1949)'s incipient Froude number of 1.525 when the intake is sufficiently far from the channel bottom $(b/h \geq 2.0)$. At $b/h < 2.0$, the boundary effect predominates and the incipient Froude number reduces. When a sink is located at bottom, the incipient Froude number was found to be approximately 0.54, which is close to the Hocking (1991)'s experimental value of 0.46. Figure 5.2 shows two stages of draw-down process for simulation A2. A stagnant-type interface (Figure 5.2a) turns to a cusp shape interface at $F > 1.4$ (Figure 5.2b). This is consistent with

Hocking and Forbes (1991)`s theoretical work, as Hocking and Forbes (1991) found stagnant type solutions up to $F = 1.4$. It was also observed that incipient drawdown occurs at $F \approx 1.52$ (Figure 5.2b). These observations are consistent with Gariel (1949)`s experimental and Craya (1949)`s theory. When the intake was located at the channel bottom, a theoretical model was developed showing that the theoretical model agrees well with simulations. Shammaa and Zhu (2010) carried out experimental investigation of selective withdrawal using point sink. Comparison between numerical solver and the investigation of Shammaa and Zhu (2010) is shown in Figure 5.3. Excellent agreement is noted.

5.5 Theoretical Development

5.5.1 Horizontal Bottom

The method developed in this study, is based on two steps. In step 1, one needs to estimate the height of the interface above the sink, or cusp height (y_s). In step 2, one needs to compute the height of the interface (h') at $x = \infty$ using y_s. The Euler's v-momentum equation for the lower layer is as follows,

$$\rho u \frac{\partial u}{\partial x} + \rho v \frac{\partial v}{\partial y} = -\frac{\partial p}{\partial y} - \Delta \rho g$$

Equation 5.5

where, v is the vertical velocity. At the outlet wall, $u = 0$. Considering the bottom boundary, the vertical velocity (v) can be estimated using potential flow theory as follows,

$$v = -\frac{2q}{\pi y}$$

Equation 5.6

Substituting u and v velocity in Equation 5.5,

$$\rho \frac{4q^2}{\pi^2 y^3} = \frac{\partial p}{\partial y} + \Delta \rho g$$

Equation 5.7

It is expected that to entrain the upper layer fluid, at $y = y_s$, $\partial p / \partial y$ should be equal to zero. Substituting $\partial p / \partial y = 0$ in Equation 5.7, and after rearranging, one obtains,

$$\frac{q}{\sqrt{\frac{\Delta \rho}{\rho} g y_s^3}} = \frac{\pi}{2}$$

Equation 5.8

This equation was found to reliably estimate y_s for any sink location. However, for an infinite depth reservoir, and for a sink located close to the bottom, the equation to compute v is different. For an infinite depth reservoir, $v = -q/\pi y$ and the equation to compute y_s is,

$$\frac{q}{\sqrt{\frac{\Delta \rho}{\rho} g y_s^3}} = \pi$$

Equation 5.9

For a sink located at a distance of b from the bottom, v can be computed as,

$$v = -\frac{q(2y + b)}{\pi y (y + b)}$$

Equation 5.10

The equation to compute y_s is,

$$\frac{q^2(2y_s+b)(b^2+2by_s+2y_s^2)}{\pi^2 y_s^3(y_s+b)^3}=\frac{\Delta\rho}{\rho}g$$

Equation 5.11

Numerical iteration is required to retrieve y_s from this equation. It is observed in simulations (simulation B1, B2, B3) that increasing sink opening size does not affect q_i, or y_s. Similar features were experimentally observed by Harleman and Elder (1965) and Jirka (1979) for their skimmer wall study. For the horizontal bottom case, this issue can be proven through analogy with a free overfall problem. In a free overfall problem, the critical depth, $y_c=1.398y_b$, where y_b is the brink depth, or the depth at the brink of the overfall (Handerson, 1966). At the critical section, the Froude number is equal to 1, that is

$$\frac{q}{\sqrt{\frac{\Delta\rho}{\rho}g\,y_c^3}}=1$$

Equation 5.12

Substituting, $y_c=1.398y_b$ in Equation 5.12, one obtains,

$$\frac{q}{\sqrt{\frac{\Delta\rho}{\rho}g\,y_b^3}}=1.65$$

Equation 5.13

Comparing Equation 5.13 with Equation 5.8, it can be shown that $y_b=0.97y_s$, in other words, $y_b\approx y_s$. This implies that at $q=q_i$, the water depth at the free overfall problem and water depth at the upstream of the line sink is nearly the same. For this reason, increasing the line sink opening does not affect the flow parameters. If one assumes that the sink size (d) is close to y_s, the energy equation can be applied between the outlet section and far upstream section, which is,

$$\frac{\Delta\rho}{\rho}h+\frac{q^2}{2gh^2}=\frac{\Delta\rho}{\rho}y_s+\frac{q^2}{2gy_s^2}$$

Equation 5.14

This equation can be used to estimate h. In the selective withdrawal problem, it is observed that at far upstream flow is subcritical, and the densimetric Froude number (F_D) is less than 1. Close to the outlet, flow is supercritical ($F_D > 1$ $F_D > 1$), and flow is critical somewhere in between. Therefore, h and y_s are the alternate depths of each other. The cusp height (y_s) is found to be close to $0.5h$. These features are similar to the free-overfall problem. Vanden-Broeck and Keller (1987) obtained solution for all values of $F \geq 1$ for sink on a horizontal bottom. At the incipient condition, F at upstream section is less than 1, and therefore these solutions are not capable of detecting the incipient condition.

5.5.2 Tilted Bottom

If the bottom forms an angle α with the horizontal line, the vertical velocity at the sink wall can be computed following Islam and Zhu (2010)'s equation as follows,

$$v=-\frac{q}{(0.5\pi+\alpha)y}$$

Equation 5.15

Therefore, the equation to compute y_s is as follows,

$$\frac{q}{\sqrt{\frac{\Delta\rho}{\rho} g y_s^3}} = \frac{\pi}{2} + \alpha$$

Equation 5.16

where, α is in radian. To compute h, the energy equation (Equation 5.14) can be applied by taking q' instead of q, where

$$q' = \frac{\pi}{(\pi + 2\alpha)} q$$

Equation 5.17

5.6 Results and Discussions

5.6.1 Incipient Criteria

From Table 5.1, it is observed that Gariel (1949)'s incipient criteria is valid as long as $b/h \geq 2$. At b/h<2, the bottom boundary effect is predominant. The incipient Froude number is 0.54 and 1.54 at b/h=0 and 2, respectively. At intermediate values of b/h, F increases with increasing b/h, which may be empirically fitted. An analytical solution is presented to determine the cusp height for all these cases. Table 5.1 shows the comparison between the theoretical and the simulated cusp height. Excellent agreement is observed between the two. It is observed that $y_s \approx \frac{2}{3}h$ when $b/h > 2$, which is expected. As the sink gets close to the channel bottom, y_s gets close to $0.5h$..

This study developed a theoretical model to predict the incipient Froude number when b/h=0. Simulated and theoretical values of the incipient Froude number for this condition are shown in Table 5.1 (simulations B1, B4, B5, and B6). Excellent agreement between the two is noted.

A theoretical model was developed to compute the Froude number for the titled bottom. Simulation B7 and B8 shows (Table 5.1) the numerical result when bottom has 5 degree angle with the horizontal. Theoretically computed y_s and h are also tabulated. Both showed reasonable agreement.

5.6.2 Velocity Prediction

Velocity prediction in stratified flow is an interesting area to explore. This study analyzed velocity profiles for the cases for one layer withdrawals as well as when both layers are withdrawn. For one layer withdrawals, it is observed that velocity profiles in the withdrawal layer can be fairly well estimated using the Islam and Zhu (2010)'s unstratified equation, considering the upper boundary is located at the interface instead of the water surface. Figure 5.4 shows the simulated u velocity profile when one layer withdraws with $h = 0.075$ m, $b = 0.2$ m, $q = 0.002$ m^2/s, and $\Delta\rho / \rho = 0.002$. The interface is located at $y/(h+b) = 1.0$. Velocity above the interface level is found to be nearly zero. A theoretical profile was computed by assuming the upper boundary was located at interface level. Both showed excellent agreement.

When both layers are withdrawn, the unstratified equation can still be applied without any modification when $h \approx 0$. Figure 5.5 shows a case where $h = 0$, $b = 0.2$ m, $q = 0.002$ m^2/s, and $\Delta\rho / \rho = 0.002$. In this case, both layers withdraw at almost the same rate and the unstratified equation of Islam and Zhu (2010) can be applied by keeping the upper boundary at the water surface. In Figure 5.5 excellent agreement between the simulated velocity profiles and the theoretical profiles were obtained.

For the case when $0 < h < h_i$, it is observed that $q_l > q_u$, where q_l is the withdrawal rate from the lower layer and q_u is the withdrawal rate from the upper layer. Therefore, velocity in the upper layer is found to be less than the velocity in the lower layer. The q_l and q_u can be empirically related to the interface height h using the following relationship,

$$q_l = \frac{q}{2}\left(1 + \frac{h}{h_i}\right)$$

$$q_u = q - q_l$$

Equation 5.18

It can be calculated from Equation 5.18 that, when $h \approx h_i$, $q_l \approx q$ and $q_u \approx 0$. Figure 5.6 shows a case where $h = h_i / 2$. The interface is located at $y/(h+b) = 1$. Reduction in velocity above the interface is clearly noticeable. To predict the flow field below the interface, Islam and Zhu (2010)'s equation can be applied using q_l instead of q and taking the upper boundary as the interface. Again, velocity in the upper layer can be predicted using the same equation with q_u and taking the lower boundary as the interface. The predicted velocity field is shown in Figure 5.6. It is observed that this combination approach predicts the flow-field very accurately except very close to the intake.

5.7 Conclusions

This study analyzed different aspects of flow upstream of a line sink in a stratified environment. A multiphase computational fluid dynamic solver was used to generate the flow field and the interface level. It was observed that the CFD solver can predict the incipient withdrawal height very consistently with Gariel (1949)'s experimental data when the sink is located sufficiently far from the bottom and with Hocking (1991)'s experimental data when sink is located at the bottom.

It was observed that the bottom boundary effect is predominant when $b/h \leq 2$. The incipient Froude number reduces by 0.54 from 1.54 as the sink location approaches the bottom. Using Euler's equation, an expression is developed to predict the interface height above the sink location, or the cusp height. This equation was formulated for any location of sink above the bottom. Using this cusp height estimator, a theoretical model was developed which can accurately predict the incipient height when the sink is located at the bottom. The model is also applicable for a sink with large opening size and for the titled bottom case.

The velocity field upstream of the line sink was analyzed for the stratified condition. It was observed that the unstratified equation can fairly accurately predict the flow-field when one layer withdraws by taking the interface level as the upper boundary. When both layers are withdrawn, the withdrawal rate for each layer depends on the height of the interface. An algorithm was suggested to predict the flow-field under such condition. It can also be concluded that the CFD solver can be considered as a reliable tool in predicting both the interface level and the velocity field in stratified flow.

5.8 References

Craya, A., (1949), Theoretical research on the flow of nonhomogenous fluids, La Houille Blanche, 4, 44-55.

Gariel, P.P., (1949), Experimental research on the flow of non-homogenous fluids, La Houille Blanche, 56-64.

Harleman, D.R.F., and Elder, R.A., (1965), Withdrawal from two layer stratified flows, Journal of the Hydraulics Division, Proceedings of the ASCE, HY4, 91(2), 43-58.

Henderson, F.M., (1966), Open Channel Flow, p. 194, The Macmillan Company, NY.

Hocking, G.C., and Forbes, L.K., (1991), A note on the flow induced by a line sink beneath a free surface, J. Aust. Math. Soc. Ser. B 32,251-260.

Hocking, G.C., (1991), Critical withdrawal from a two-layer fluid through a line sink, Journal of Engineering Mathematics, 25, 1-11.

Hocking, G.C., (1991), Withdrawal from two layer fluid through line sink, Journal of Hydraulic Engineering, 117(6), 800-805.

Islam, M.R., and Zhu, D.Z., (2010), Flow upstream of two dimensional intakes, Journal of Hydraulic Engineering, (in press).

Jirka, G.H., (1979), Supercritical withdrawal from two-layered fluid systems, Part 1: Two-dimensional skimmer wall, Journal of Hydraulic Research,17(1), 43-51.

Shammaa, Y., and Zhu, D.Z., (2010), Experimental study on selective withdrawal in a two-layer reservoir using a temperature-control curtain, ASCE Journal of Hydraulic Engineering, 136(4), 234-246.

Vanden-Broeck, J.M., and Keller, J.B., (1987), Free surface flow due to a sink, J. Fluid. Mech., 175, 109-117.

Vanden-Broeck, M., and Tuck, E.O., (1984), A cusp-like free-surface flow due to a submerged source or sink, J. Austral. Math. Soc. Ser., B 25, 451-462.

Wood, I.R|., and Lai, K.K., (1972), Selective withdrawal from a two layered fluid, Journal of Hydraulic Research, 10(4), 475-493.

Table 5.1: Description of simulations carried out.

Test Run	Flow rate, q_m, (m2/s)	Intake location, (b), m	Intake size, (d), m	$\frac{\Delta\rho}{\rho}$	Interface height, (h), m	$\frac{b}{h}$	Cusp height, (y_s), m	Froude no, (F)	y_s theory m	h theory m	F theory
A1	0.0024	0.3	0.0025	0.002	0.05	6	0.035	1.53	0.032	__	__
A2	0.0024	0.2	0.0025	0.002	0.05	4	0.033	1.53	0.032	__	__
A3	0.0024	0.1	0.0025	0.002	0.05	2	0.035	1.53	0.032	__	__
A4	0.0036	0.05	0.0025	0.002	0.07	0.71	0.045	1.39	0.046	__	__
A5	0.006	0.035	0.0025	0.008	0.065	0.54	0.04	1.3	0.041	__	__
A6	0.0017	0.025	0.0025	0.002	0.05	0.5	0.03	1.08	0.028	__	__
A7	0.0024	0	0.0025	0.002	0.1	0	0.049	0.54	0.049	0.094	0.6
B1	0.0024	0	0.0025	0.002	0.1	0	0.049	0.54	0.049	0.094	0.6
B2	0.0024	0	0.03	0.002	0.1	0	__	0.54	__	__	__
B3	0.0022	0	0.05	0.002	0.1	0	__	0.5	__	__	__
B4	0.003	0	0.0025	0.003	0.1	0	0.05	0.55	0.05	0.094	0.6
B5	0.0036	0	0.0025	0.004	0.1	0	0.05	0.57	0.051	0.099	0.58
B6	0.0036	0	0.0025	0.002	0.12	0	0.066	0.62	0.064	0.122	0.6
[1]B7	0.0036	0	0.0025	0.002	0.12	0	0.065	0.64	0.064	0.12	0.64
[1]B8	0.0027	0	0.0025	0.002	0.1	0	0.055	0.61	0.051	0.096	0.64

[1] These simulations are done with tilted bottom.

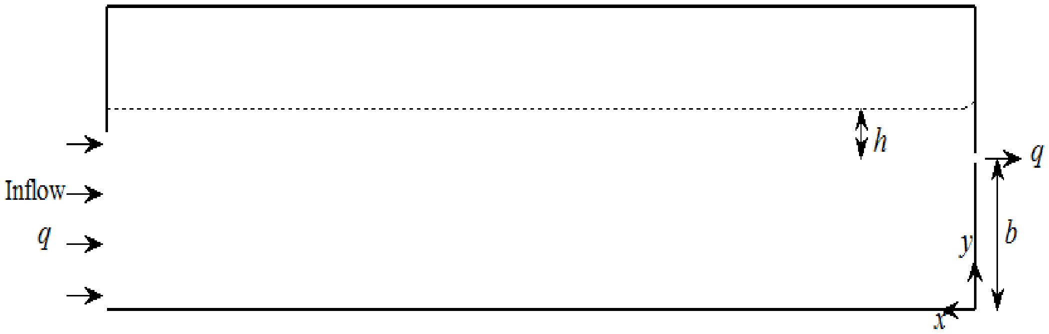

Figure 5.1: A 2D schematic side view of the model geometry.

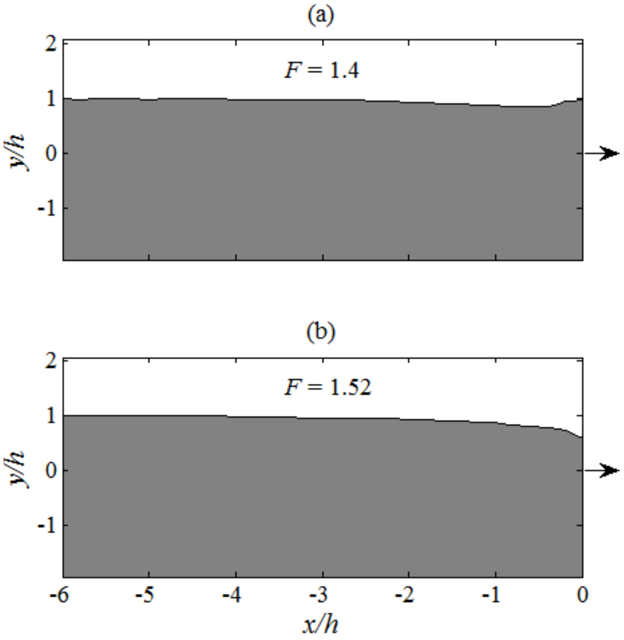

Figure 5.2 : Computational interface profile at two different Froude number for simulation A2.

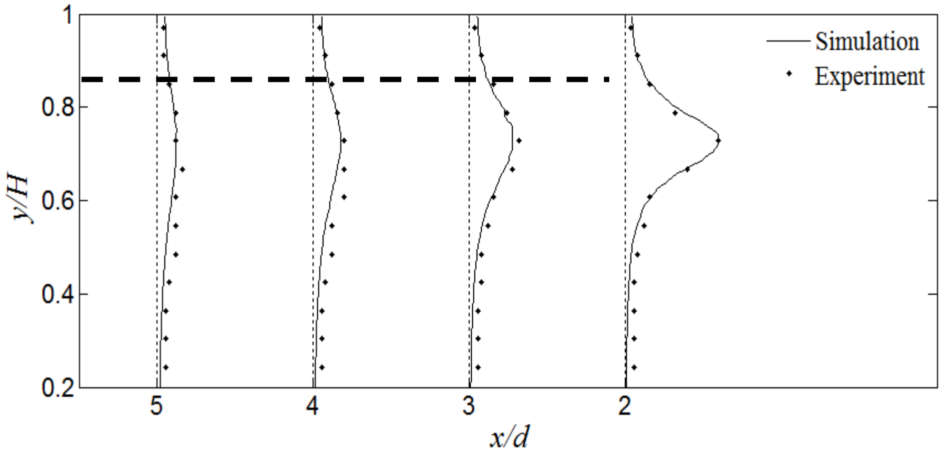

Figure 5.3: Comparison between simulation and the experiment of Shammaa and Zhu (2010).

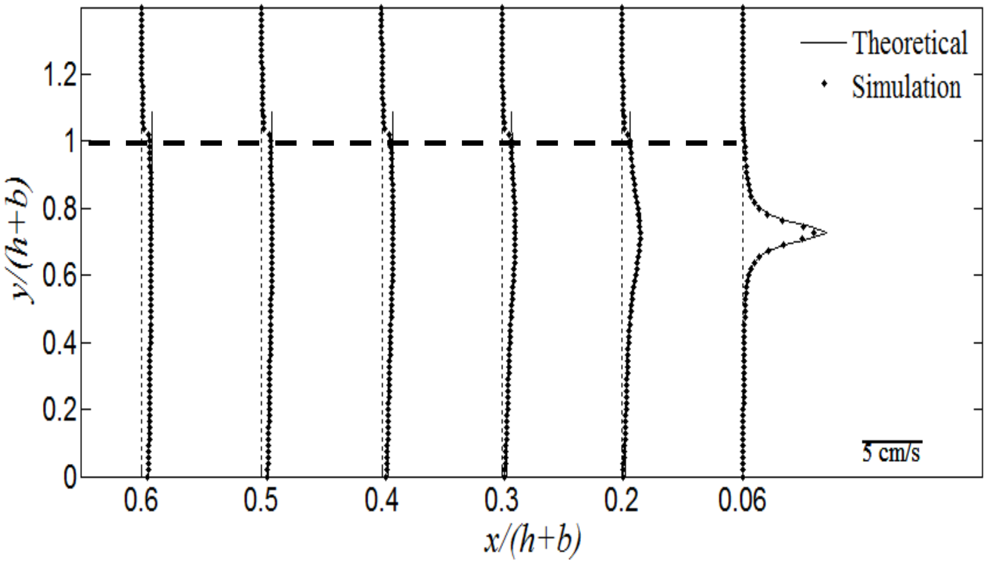

Figure 5.4 : Comparison between theoretical and simulated u velocity profiles when one layer withdraws.

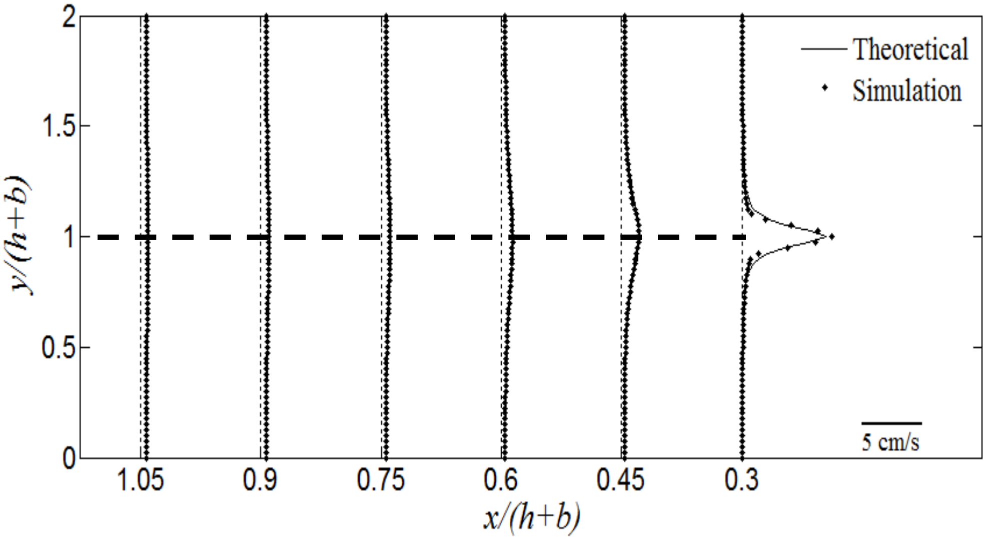

Figure 5.5: Comparison between theoretical and simulated velocity profiles when $h = 0$.

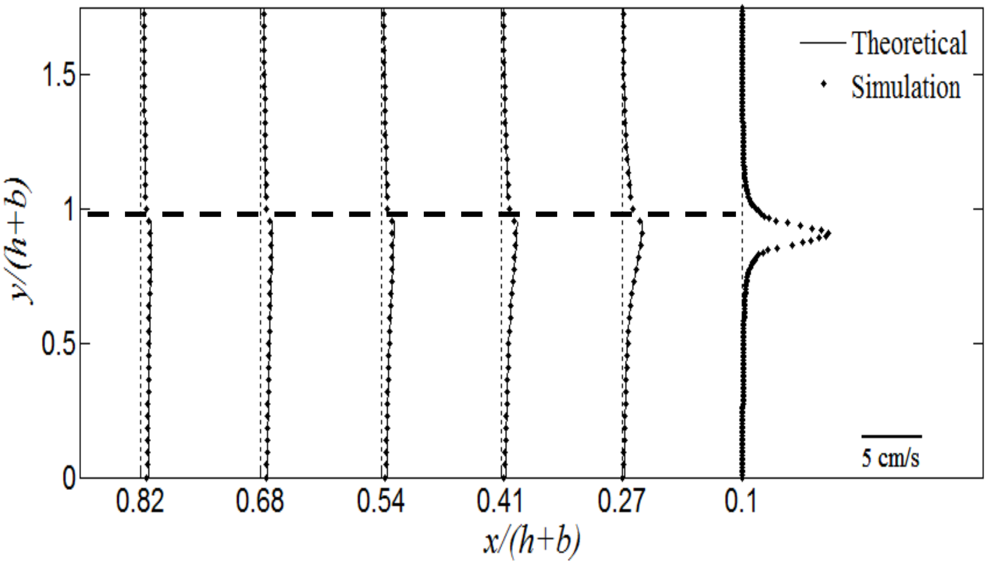

Figure 5.6: Comparison between theoretical and simulated velocity profiles when $h = 0.5h_i$.

Chapter 6

Conclusions and Recommendations

6.1 General Conclusions

This paper based thesis is primarily concerned with assessing the flow field induced by hydropower intakes, with special focus on the flow modified by temperature control curtains. The general conclusions are summarized below.

Chapter 2 investigated the applicability of potential flow theories in estimating the flow-field upstream of hydropower intakes through a review work. It is concluded that potential flow theories can be considered as a reliable tool in predicting the near intake flow field of hydropower dams of various intake geometries and orientations. These flow fields can be used for studying fish entrainment and in installing fish repulsion systems.

Chapter 3 investigated the flow field downstream of a temperature control curtain. It was documented that the flow-field downstream of a temperature control curtain can be hypothesized as a wall jet with a recirculation zone above it

(Shammaa et al., 2009). This study found that pressure is adverse downstream of the center of the recirculation zone, which causes a drop in momentum-flux. The wall jet behavior is preserved only up to the center of the recirculation zone where the pressure-gradient is small. The jet spreading rate and the velocity decay coefficient were observed to vary with the inlet Reynolds number and water depth. Empirical expressions were developed to get these properties as a function of the inlet Reynolds number and water depth. The effect of the outlet boundary was observed on the jet region only when it was placed inside the jet region. The wall jet then behaved as an impinging jet on the outlet wall and Beltaos and Rajaratnam (1972)'s observation on impinging jets is clearly noticeable. An expression was developed to estimate the maximum wall shear stress and to estimate the outlet affected region.

Chapter 4 investigated the unstratified flow-field upstream of the curtain where the curtain was modeled as a two dimensional sink. Emphasis is given to identify the flow acceleration region upstream of a two dimensional sink, which can be useful for fish entrainment studies. Using the Schwarz-Christoffel transformation, mathematical expressions were developed to estimate the flow-field upstream of the curtain and to estimate the extent of the acceleration zone. It was found that the water depth, as well as size, and location of the intake can affect the acceleration zone. When the intake size is small, the acceleration zone can extend up to 1.7h where h is the water depth. It was observed that when the line sink is not located at bottom, the location of the maximum velocity upstream of the intake can deviate away from the intake centerline. The method of images was found unsuitable at far upstream as it can seriously underestimate velocities. The interaction of multiple intakes was also analyzed.

Chapter 5 investigated stratified flow upstream of the curtain. This study developed a theoretical model to get the incipient withdrawal condition for a two dimensional sink located on the horizontal bottom. The method was also extended for a tilted bottom. It was found that the unstratified flow-field can be used to predict the velocity field in the stratified condition when only one layer withdraws by placing the upper boundary at the interface level. When both layers are withdrawn, the unstratified equation can still be applied after some modifications. It was observed that the effect of the bottom boundary is negligible when $b/h>2$, where h is the interface depth and b is distance of the intake from the horizontal bottom boundary. In this regime, Craya (1949)'s theory can be applied to predict the incipient withdrawal condition.

In Appendix A, a despike algorithm for Acoustic Doppler Velocimeter (ADV) data is presented. In Chapter 3, numerical results were validated with experiments in jet studies. The experimental data was taken with a 200 Hz four beam ADV. The conventional despike algorithm was found to be unsuitable in the jet region, where 30-40% data can be corrupted with spikes. A kernel density based despike algorithm was developed to remove spikes from the ADV data. This method develops a density map of data clusters and spike clusters. By developing a suitable algorithm, data clusters can be isolated from spike clusters. This method can also be used as a generic outlier removal algorithm.

Appendix B is concerned with developing a correction scheme to improve the accuracy of the numerical scheme. It was shown that for a one dimensional problem, all the truncation error terms can be converted to a series summation. By adjusting this series summation in the numerical computation, the numerical error can be dramatically reduced. The method is extended for the inhomogeneous problem. Following this idea, an approximate solution was developed for two dimensional problems.

6.2 Future Research Scope

Immense opportunities are available to extend the ideas developed in these studies. Some of them are:

It was observed in Chapter 3 that wall jet properties are significantly affected by the shallow water depth and by the inlet Reynolds number. A turbulence study may be able to explain this behavior. It can be hypothesized that a recirculation system reintroduces the eddy and therefore a shallow water depth may increase the turbulence level and thereby the jet spreading rate. Therefore, a turbulence study can be recommended as a future study.

In Chapter 4, using potential flow theories, the velocity field for a two dimensional nozzle was predicted. The developed equation may be applied to predict the velocity field in a curved intake. This issue can be investigated in detail as a future study. Future studies may also focus on developing a close-form solution for a point sink with boundaries, and on analyzing the effect of boundaries on the acceleration zone for the case of point sinks. Examining the interaction of multiple point sinks can also be an interesting topic.

It may also be possible to develop a simple expression to predict the pressure field upstream of an intake. In a region with strong pressure gradients, fish may not quickly adjust their bladder system to maintain neutral buoyancy and may lose stability (NPP, 2005). Therefore, simple mathematical expressions can be developed to predict the high risk region based on the pressure field where fish may become disoriented.

Chapter 5 analyzed the boundary effect on the incipient withdrawal condition for a line sink. Similar studies can be conducted to assess the boundary effect on the incipient withdrawal for a point sink. An expression can be developed to determine the cusp height when the point sink is located close to the bottom.

6.3 References

Beltaos, S., and Rajaratnam, N., (1972), Plane turbulent impinging jets, Journal of Hydraulic Research, 11(1), 29-57.

Craya, A., (1949), Theoretical research on the flow of nonhomogenous fluids, La Houille Blanche, 4, 44-55.

NPP (2005), Fish Entrainment and Mortality Study, Vol 1, NY Power Authority.

Shammaa, Y., Zhu, D. Z., and Rajaratnam, N., (2009), Flow field in a rectangular basin with a line inlet and a circular outlet, Journal of Hydraulic Engineering, ASCE, 135(10), 857-864.

Appendix A

A Kernel-Density Based Algorithm for Despiking ADV data[4]

A.1 Introduction

Acoustic Doppler Velocimeter (ADV) data is often contaminated by spikes, and de-spiking is often considered essential during post-processing of ADV data. Nikora and Goring (1998) showed that Kolmogorov's universal '-5/3' slope is not maintained with spiked ADV data. Doppler noises and spikes in the acoustic measurements can arise due to the random motion of seeding particles within the sampling volume (Voulgaris and Trowbridge, 1998), velocity aliasing (Rusello, 2009), air bubbles (Liu et al, 2002), and boundary interferences (Lane et al., 1998), among others. A number of algorithms have been developed in the last

---

[4] A version of this article has been submitted to the ASCE's Journal of Hydraulic Engineering.

decade to despike ADV data, which serves the same purpose as outlier detection algorithm in statistics. Goring and Nikora (2002) proposed an acceleration threshold method and a phase-space threshold method to despike ADV data. The phase-space threshold method was later modified by Wahl (2003) and was included in a post-processing software, WinADV (Wahl, 2003). In the acceleration threshold method, accelerations and velocities greater than (or less than) a certain threshold are considered as spikes and are eliminated. The eliminated data is replaced by applying an appropriate interpolation technique. The entire process is repeated until no further spikes are detected. The idea behind the phase-space threshold method is to develop a three dimensional map placing u-velocity, its first derivative (Δu), and second derivative ($\Delta^2 u$) on each axis, and thereafter drawing an ellipsoid. The axes of the ellipsoid are determined using the universal threshold (Donoho and Johnstone, 1994) as the cut-off value. The three-dimensional ellipsoid is projected on the three coordinate planes and therefore three ellipses are formed. Any data point that resides outside any of the ellipses is considered to be a spike and is replaced. The entire process is repeated until no further spikes are detected. The hypothesis behind this method is that good data points lie in a cluster in the $u - \Delta u - \Delta^2 u$ space and spikes lie outside the cluster. Wahl (2003) modified the phase-space method to detect the outlier on a true ellipsoid, rather than on its projections. Another key contribution of Wahl (2003)'s study is to apply robust statistics, i.e. using median as the location estimator, and median absolute deviation (MAD) as the spread estimator as suggested by Rousseeuw (1998). The robust statistical method eliminates the necessity of iterations. Wahl (2003) applied Chauvenet's criterion instead of the universal threshold as the cut-off value. Cea et al. (2007) developed another method similar to the phase-space threshold method, but uses three velocity components (*u*, *v*, and *w*) along three coordinate axes, rather than *u*-velocity components and its derivatives. This method, termed as velocity correlation filter, is also based on iterations and uses the universal threshold as the cut-off value. The time series plot of the earlier studies shows that the spikes were similar to phase-wrapping spikes for which true velocity can be retrieved (Rusello, 2009).

This study uses measured data from a wall jet as a test case which shows a large amount of spikes due to the presence of a free shear layer and strong turbulence. It was observed that all the three standard despiking methods mentioned above are inefficient in this region. This motivated the development of a new algorithm that is suitable for this region. The developed algorithm uses a bivariate kernel-density estimator (Duong and Hazelton, 2003) to generate a density plot in $u-\Delta u$, and $w-\Delta w$ space, where u and w are the x and z directional velocity components, respectively, as shown in Figure A.1, and Δu and Δw are their first derivatives. The density plot is then used to separate data cluster from the surrounding outlier clusters. This method can be used in other regions where spike density is not sufficiently large as well.

A.2 Algorithm Description

In this study, ADV measurements were obtained for a wall jet in an experimental flume as shown in Figure A.1. The experimental set-up has an inlet opening b_{in} =

2.54 cm, water depth H = 0.36 m, unit width flow rate q = 0.03 m^2/sec, channel length L = 2.45 m, and outlet height h_0 = 0.3 m. A bistatic sonar four beam Vectrino probe (Nortek AS model, VCN 7569) was used with 200 Hz sampling frequency. Approximately 72 samples were collected to assess the performance of the standard despike algorithms and to verify the new algorithm. Each sample has 60,000 data points measured over five minute duration The ADV measurements were also compared with the mean velocity results of Ead and Rajaratnam (2002) using a Pitot tube.

Figure A.2 shows the mean velocity profiles at several locations, where the data was despiked with the phase-space method, Wahl (2003)'s methods and the velocity correlation method. It was observed that in the jet region mean velocities are scattered and typical wall jet profiles as obtained by Ead and Rajaratnam (2002) using a pitot-tube were not retrieved. This study found that in the jet region, the amount of outliers can be as high as 30-40% of the total sampled data. Despike methods based on the universal threshold or Chauvenet's criteria include outliers in all the three algorithms mentioned above. Figure A.3 shows the time series of u velocity at a point 'P1', where spikes are visible at regular intervals. The point 'P1' is located a distance of 216 cm downstream of the inlet and at 1.4 cm above the channel bottom. Figure A.4a shows the outlier demarcation using the phase-space method in the $u-\Delta u$ space and Figure A.4b shows outlier demarcation with Cea et al. (2007)'s velocity correlation method in the u-w space for the point 'P1'. The central spot is the data cluster and surrounding spots are created due to spikes. Figure A.4 shows that spike spots are located inside the ellipse, which demonstrates the inefficiency of the two algorithms in this situation. Outliers inflate the standard deviation and thereby increase the size of the ellipse. Wahl (2003)'s one-step procedure was also found to be inefficient in this region. Reducing the cut-off threshold can solve this problem. However, it was observed that a low cut-off threshold trims the data points in the region where the spike density is less. Figure A.5 shows another data-point 'P2' located 72 cm downstream of the inlet and 25 cm above the bottom, where the spike density was found to be very insignificant. It was observed that the universal threshold works efficiently in this region and the smaller cut-off ratio trims the data points. Based on the above observations, this study attempts to develop a method that uses a variable cut-off threshold. In other words, the cut-off threshold is automatically determined form the data and spike morphology.

This can be achieved by using a bivariate kernel-density estimation. The kernel density is a non-parametric estimation of density (Silverman, 1986). It is similar to a histogram, but its advantage is that it can provide a smooth estimation of density if a suitable bandwidth is selected. A bivariate kernel density with a Gaussian kernel can be estimated by (Duong and Hazelton, 2003),

$$\hat{f}(\mathbf{x},\mathbf{y}) = \frac{1}{2\pi N h_x h_y} \sum_{i=1}^{N} e^{-\frac{(\mathbf{x}-x_i)^2}{2h_x^2} - \frac{(\mathbf{y}-y_i)^2}{2h_y^2}}$$

Equation A.1

where, N is the total number of samples, h_x and h_y are the band widths in the two axes, x_i and y_i are the realizations of the two variables, x and y are the locations where densities are to be estimated, and $\hat{f}(\mathbf{x},\mathbf{y})$ is the estimated density at this location. For example, in the phase-space method, $(\mathbf{x}, \mathbf{y})$ can be replaced by (u, $\mathbf{\Delta u}$), and in the velocity correlation method of Cea et al. (2007), $(\mathbf{x}, \mathbf{y})$ can be replaced by $(\mathbf{u}, \mathbf{w})$. Figure A.6a shows the kernel-density estimation of the $u - \Delta u$ space shown in Figure A.4a. The large peak shows the main data cluster. By drawing an ellipse at the foot-print of this peak, the data cluster can be separated from the outliers. Figure A.6b shows the ellipse in the $u - \Delta u$ space. Comparing with Figure A.4a, this ellipse only retains the main data cluster and excludes the spike clusters.

This study finds a modified version of the $u - \Delta u$ space more efficient. Goring and Nikora (2002) computed Δu using the relationship $(u_{i+1} - u_{i-1})/2$, which is a central difference approximation. Figure A.7a shows a hypothetical spike located at point 4 (i = 4) and Figure A.7b shows an approximation of Δu using a central difference approximation. With this approximation, the 3rd and the 5th point can be identified as spikes, although these are not real spikes. With a backward difference approximation, point 5 can be identified as a spike and with a forward difference approximation, point 3 can be identified as a spike. In the jet region, where 30-40% data might be discarded as spikes, loosing additional points is not worthwhile. To solve this problem, this study proposes to compute Δu using both forward and backward approximations, and choose the one which has the minimum absolute value. It is observed that this definition removes less outliers compare to the central difference approximation. The detailed outlier detection algorithm developed in this study can be described as follows:

1. Decide a pair of variables for the variable space, e.g., u and Δu. The Δu is to be computed using both backward and forward approximations, and select the one having a smaller absolute value. For generalization, u and Δu are represented by x and y hereafter.

2. Estimate the rotation angle of principal axes using the classical least square approximation,

$$\theta = \tan^{-1}\left(\frac{N\sum_{i=1}^{N} x_i y_i - \sum_{i=1}^{N} x_i \sum_{i=1}^{N} y_i}{N\sum_{i=1}^{N} x_i^2 - \left(\sum_{i=1}^{N} x_i \right)^2} \right)$$

Equation A.2

3. Transform the data using the following formula,

$$x_t = x\cos\theta + y\sin\theta, \quad \text{and} \quad y_t = -x\sin\theta + y\cos\theta$$

Equation A.3

4. Rescale the data by the following formula so the data range will be from 0 to 1,

$$x_s = \frac{x - \min(x)}{\max(x) - \min(x)}, \quad \text{and} \quad y_s = \frac{y - \min(y)}{\max(y) - \min(y)}$$

Equation A.4

5. Obtain the kernel-density estimation using the scaled data by Equation A.1. Now, locate the peak $\hat{f}(x_p, y_p)$ and extract the two density profiles, $\hat{f}(\mathbf{x}, y_p)$ and $\hat{f}(x_p, \mathbf{y})$.

6. Estimate the cut-off point from the slope of the density profiles. This study found an optimum criteria to define the cut-off point as, $n_x \left| \Delta\hat{f}(\mathbf{x}, y_p) \right| / \hat{f}(x_p, y_p) \le 0.4$ and $n_y \left| \Delta\hat{f}(x_p, \mathbf{y}) \right| / \hat{f}(x_p, y_p) \le 0.4$, where n_x and

n_y are the number of grid points used in the kernel density matrix, $\Delta\hat{f}(\mathbf{x}, y_p) = \Delta\hat{f}(x_{i+1} - x_i, y_p)$, and $\Delta\hat{f}(x_p, \mathbf{y}) = \Delta\hat{f}(x_p, y_{i+1} - y_i)$.

7. Use these cut-off points to calculate the major and minor axes of the ellipse and flag the points located outside the ellipse as the outliers.

8. Repeat steps 1-7 for the pair of $w - \Delta w$ and flag outliers located in this space. Eliminate outliers detected in either space.

A four beam ADV only uses two beams (Beam 1 and 3) to compute *u* and *w* components of velocity and the other two beams (Beam 2 and 4) to compute *v* and another set of *w* components of velocity. For this reason, outliers detected in the *v* velocity components do not need to be removed from *u* and *w* measurements.

Computing a bivariate kernel-density matrix is computationally intensive. This study uses open downloadable MATLAB source code ‘kde2d’ (Botev, 2009) which uses a fast Fourier transformation and can compute a density matrix estimation in fraction of a second. A constant band-width of $h_x = h_y = 0.01$ was found as optimal for all samples tested. Note that all the data points were normalized using Equation A.4.

A.3 Results and Discussions

The outlier detection method developed in this study can be applied in any space. However, this study found the $u - \Delta u$, and $w - \Delta w$ spaces more efficient compare to the *u*-*w* space, where Δu and Δw are computed according to the definition suggested in this study. Outliers in the *u*-*w* space show complex patterns, which outsmart despike algorithms. Figure A.8 shows the jet velocity profiles despiked with the method developed in this study. Compared to Figure A.2, the procedure developed in this study is able to retrieve the jet profiles, which compared very well with Ead and Rajaratnam (2002)'s Pitot tube measurements. Figure A.9 shows the clean time series of *u* velocity measurements at point P1. Comparing with Figure A.3, this figure shows that spikes with a magnitude greater than 0.75 m/s and less than -0.75 m/s were efficiently removed. Figure A.10 shows the power spectral density of point P1 of despiked data and the raw data. It is observed that the despiked data closely follows the Kolmogorov's '-5/3' slope in the inertial subrange.

'Correlation' is a data quality index provided by the manufacturers of the ADV. Each velocity is an average of several velocities (Nortek, 2004)) and the correlation tells us how similar these velocities are. Martin (2002) reported that turbulence obviously decreases correlation and Cea et al. (2007) debated on the necessity of discarding data with poor correlation. Figure A.11a shows a portion of the time series of beam velocity from position P2 where turbulence is comparatively weak. Figure A.11b shows the corresponding correlation of that beam. In the first half of the figure, velocity fluctuation is negligible and correlation is close to 100, whereas in the second half portion velocity fluctuates due to turbulence and the correlation is also found to decrease. This study observed that spikes may have correlations greater than 70 while good data may have a correlation less than 70. Discarding data with a correlation less than 70 takes out a significant amount of useful data while retaining a portion of spikes and does not eliminate the necessity of applying a despike algorithm. Figure A.8 shows another set of velocity profiles, where data with correlation <70 was discarded and replaced with an interpolated velocity prior to the despike algorithm. Combining the decorrelation and despike algorithms does not change the mean velocity profiles, rather it removes a significant amount of useful data located inside the data cluster.

Using a four-beam probe, any velocity components can be computed in atleast two different ways and outliers can be removed using the *u*-*u* space, the *v*-*v* space or the *w*-w space. However, the disadvantage of this method is that it will use all four beams and measurements will be discarded if any of the four beam velocity is corrupted. In the two beam approach, measurements will be discarded if any of the two beam velocities are corrupted. That is why the four beam approach is less efficient and it will lose more data points.

A.4 Concluding Remarks

ADV data is often contaminated with spikes and several despike algorithms are available in the literature. However, this study found that standard despike algorithms are not efficient in the turbulent jet region, where 30-40% data can be contaminated by spikes. Applying a constant cut-off threshold (e.g. universal threshold) was found to be the reason for this inefficiency. This study develops a despike method which can determine the cut-off point from the morphology of the data. To achieve this, a bivariate kernel-density function is used to produce a density map of the main data cluster and spike clusters, which in turn helps to isolate the data cluster from the surrounding spike clusters. It is observed that the spectral plot obtained from despiked data shows ‘-5/3’ slope in the inertial subrange and mean velocity profiles retrieve typical jet profiles. It is observed that decorrelation prior to the despike algorithm does not improve the data quality, rather it removes significant amount of useful data.

A.5 References

Botev, Z., (2009), Kernel Density Estimation, http://www.mathworks.com/

Cea, L., Puertas, J., and Pena, L., (2007), Velocity measurements on highly turbulent free surface flow using ADV, Exp. in Fluids, 42, 333-348.

Donoho, D.L., and Johnstone, I.M., (1994), Ideal spatial adaptation by wavelet shrinkage, Biometrika, 81(3), 425–455.

Duong, T., and Hazelton, M.L., (2003), Plug-in bandwidth matrices for bivariate kernel density estimation, Nonparametric Statistics, 15(1), 17-30.

Ead, S.A., and Rajaratnam, N., (2002), Plane Turbulent wall jets in shallow tailwater. Journal of Engineering Mechanics, ASCE, 2, pp 143-155.

Goring, D.G., and Nikora, V.I., (2002), Despiking acoustic Doppler velocimeter data, Journal of Hydraulic Engineering, 128(1), 117-126.

Lane, S.N., Biron, P.M., Bradbrook, K.F., Butler, J.B., Chandler, J.H., Crowell, M.D., Mclelland, S.J., Richards, K.S., Roy, A.G., (1998), Three dimensional measurement of river channel flow processes using acoustic Doppler velocimetry, Earth Surface Proc. and Landforms, 23, 1247-1267.

Liu M., Zhu, D.Z., and Rajaratnam, N., (2002), Evaluation of ADV measurements in bubbly two-phase flow, Proc. of the Hydraulic measurements and experimental methods conference, Colorado.

Martin, V., Fisher, T.S.R., Millar, R.G., and Quick, M.C., (2002), ADV data analysis for turbulent flows: low correlation problem, Proc. of the Hydraulic measurements and experimental methods conference, Colorado.

Nortek (2004), Vectrino Velocimeter, User Guide, Nortek As.

Nikora, V.I., and Goring, D.G., (1998), ADV measurements of turbulence: can we improve their interpretation?, Journal of Hydraulic Engineering, 124(6), 630-634.

Rousseeuw, P.J., (1998), Robust estimation of identifying outliers, Handbook of Statistical Methods for Engineers and Scientists, 2nd Edition, McGraw-Hill, NY,17.1-17.15.

Rusello, P.J., (2009), A practical primer for pulse coherent instruments, Nortek Technical Note, TN-027, Nortek.

Silverman, B.W., (1986), Density Estimation for Statistics and Data Analysis, Chapman and Hall, NY.

Voulgaris, G., and Trowbridge, J.H., (1998), Evaluation of acoustic Doppler velocimeter (ADV) for turbulence measurements, Journal of Atmospheric and Oceanic Technology, 15, 272-288.

Wahl, T. L., (2003), Discussion of “Despiking acoustic Doppler velocimeter data” by Derek G. Goring and Vladimir I. Nikora, J. Hydraul. Engng., 484-489.

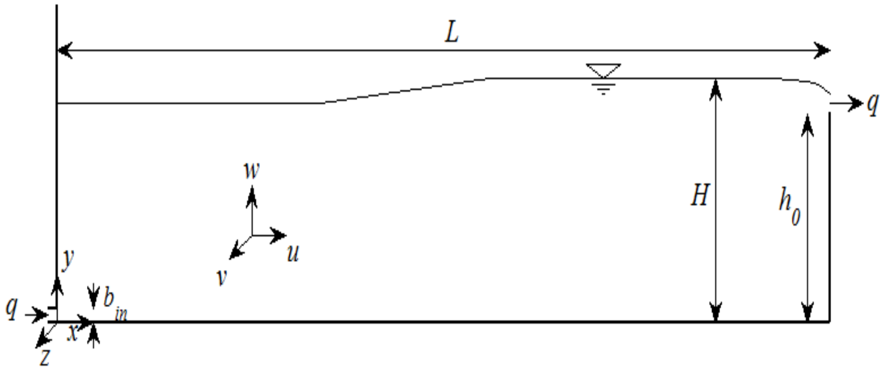

Figure A.1: A side view of the test set up having a wall jet in a rectangular channel.

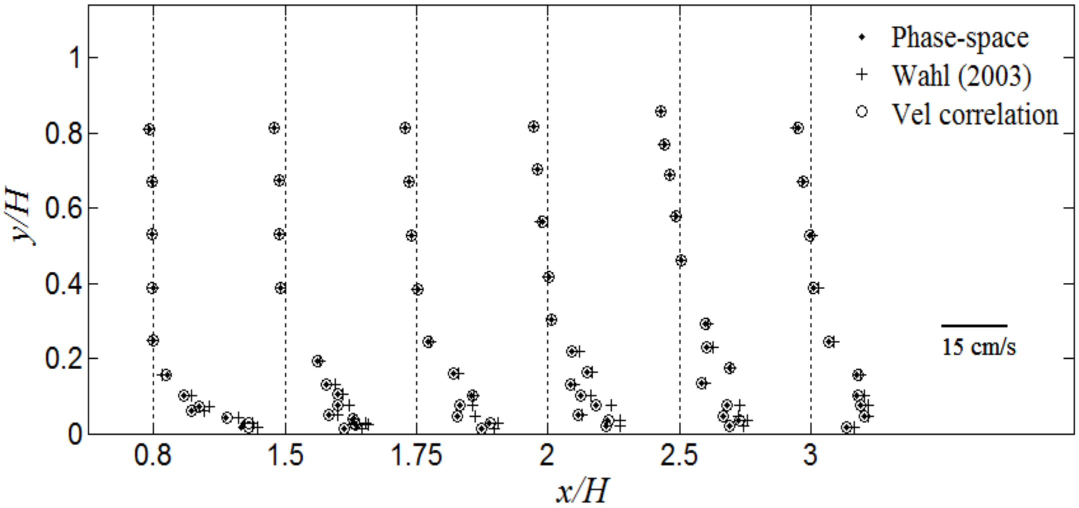

Figure A.2: Mean velocity profiles with spikes removed by three conventional methods.

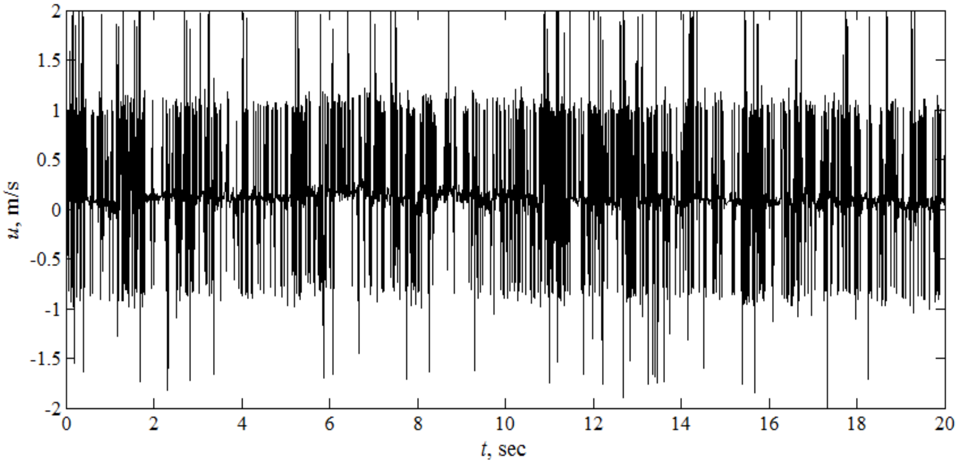

Figure A.3: Time series of u velocity at point P1 (located at 216 cm downstream from inlet and 1.4 cm above bottom) showing spikes.

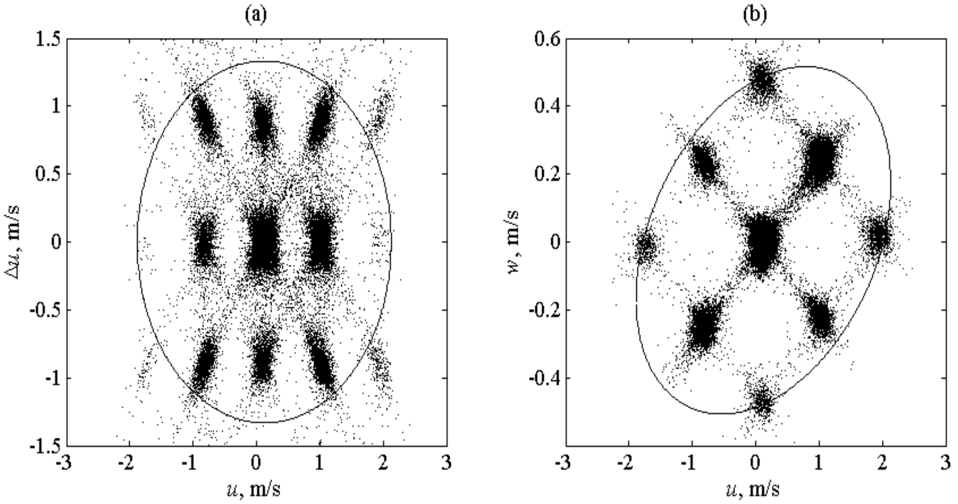

Figure A.4: Outlier detection at point P1 in (a) $u - \Delta u$ space with phase-space threshold method and in (b) u-w space with velocity correlation method.

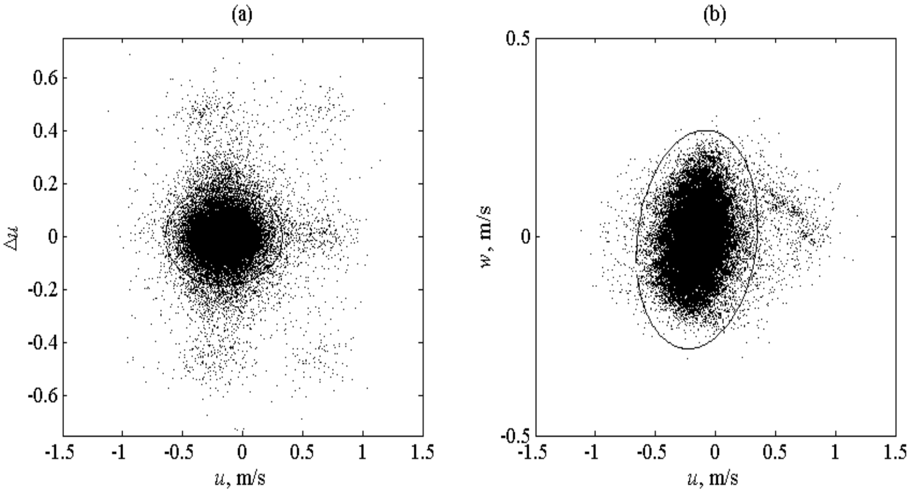

Figure A.5: Outlier detection at point P2 (located at 72 cm downstream from inlet and 25 cm above bottom) with (a) phase-space method, (b) velocity correlation method.

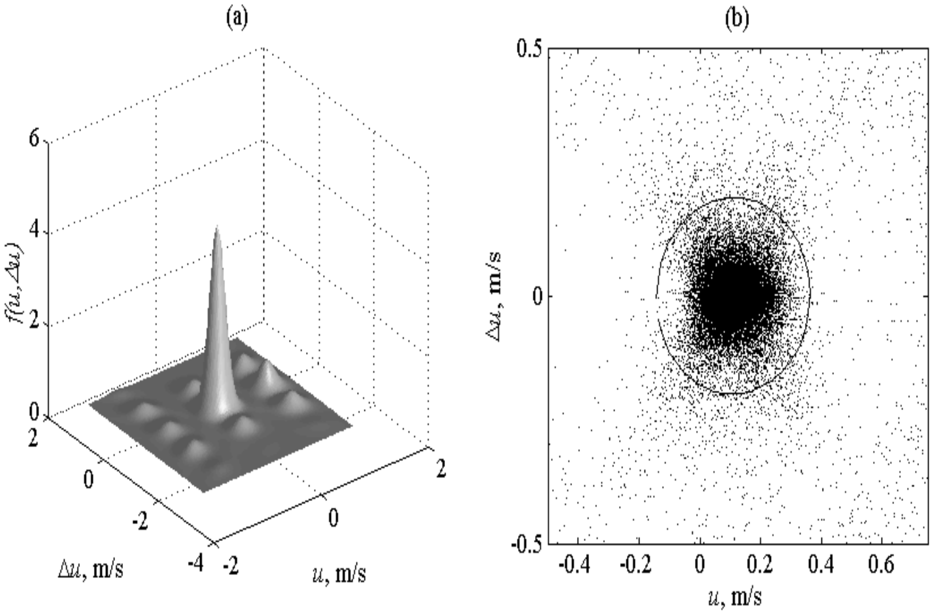

Figure A.6: (a) Kernel density plot and, (b) outlier demarcating ellipse of point P1.

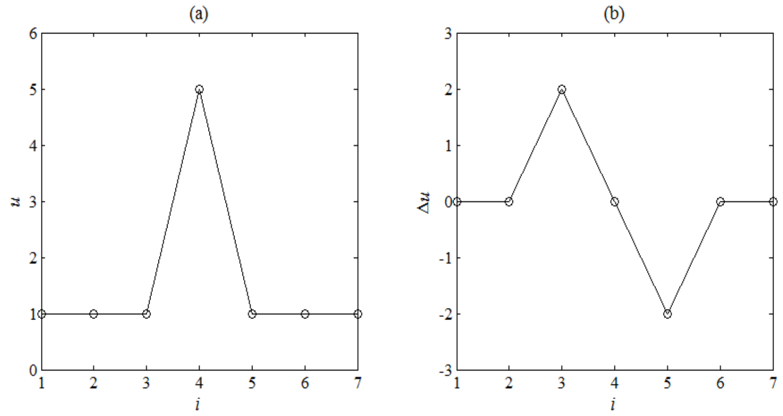

Figure A.7: A hypothetical spike and its derivative with central difference approximation.

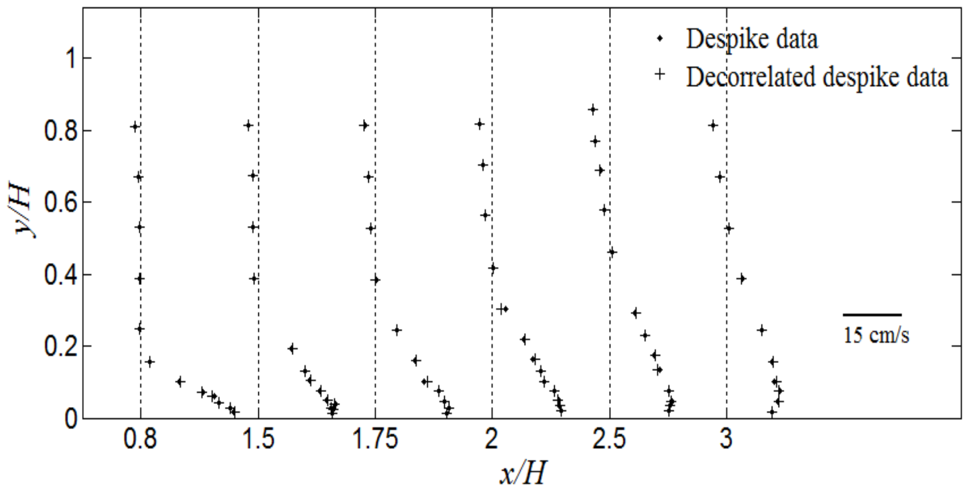

Figure A.8: Data despiked with the method developed in this study.

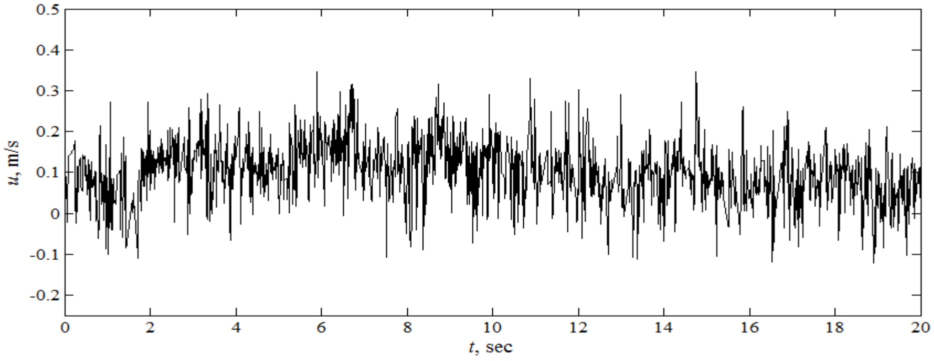

Figure A.9: A portion of spike removed time series of position P1.

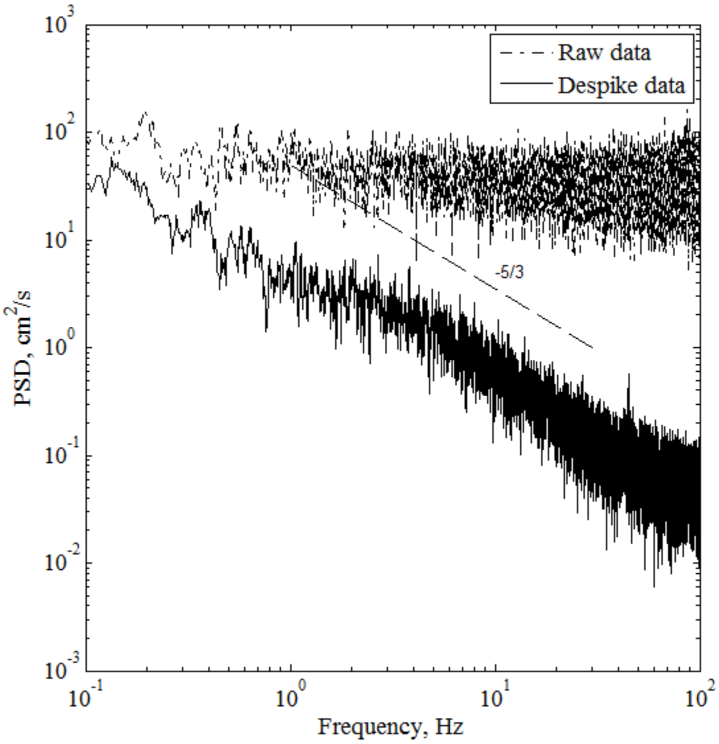

Figure A.10: The power spectral density of u velocity component of raw data and despike data at point P1.

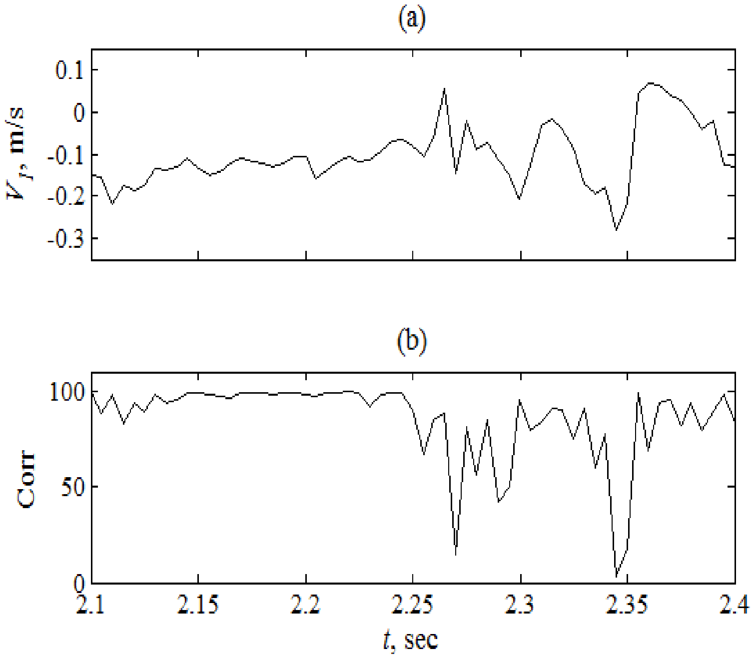

Figure A.11: A portion of time series of (a) beam velocity and (b) correlation at point P2.

Appendix B

Anti-Diffusion in Central Difference Scheme at Steady-State Transport Equation[5]

B.1 Introduction

In a scalar transport equation, the central-difference scheme causes numerical oscillation when the cell-Peclet number is greater than two (Hall and Porsching, 1990). This issue can be solved by grid-refinement. However, the limitation of computing power might not allow sufficient refinement to obtain oscillation free results (Versteeg and Malalasekera, 2007). The common treatment is to add diffusion to remove oscillations; which in turn makes the model diffusive (Wang

---

[5] A version of this chapter was accepted in the Progress in Computational Fluid Dynamics Journal.

and Hutter, 2001). For example, the hybrid difference scheme of Spalding (1972) applies a central difference scheme in the region where the cell-Peclet number is less than two, and an upwind scheme elsewhere. The Flux Corrected Transport method applies false diffusion in the case where the gradient of a variable is large in a central difference based model, and adds anti-diffusion in the region having a sharp-gradient in an upwind based model (Wang and Hutter, 2001). Hence, regions with sharp gradients of variables suffer numerical diffusion in both schemes. The upwind scheme, though free of oscillation, has numerical diffusion which can yield physically incorrect result (Huang et al., 1985). Despite this issue, Patel et al. (1985) recommended an upwind difference scheme when 5% error is acceptable considering its stability advantage. The quadratic upwind differencing scheme (QUDS) of Leonard (1979) can provide oscillations at higher cell-Peclet number. Although the recent version of QUDS developed by Hayase et al. (1992) is free of oscillation, it suffers from a diffusion problem along with minor undershoots and overshoots (Versteeg and Malalasekera, 2007). The Power-law scheme of Patankar (1980) also suffers from numerical diffusion. It should be emphasized that only grid-refinement can ensure an oscillation-free, as well as a non-diffusive result.

In this study, we showed that a central difference scheme causes anti-diffusion when applied to a steady-state scalar transport equation. An iterative anti-diffusion correction algorithm is developed based on a Taylor analysis of the truncation error terms. Once this anti-diffusion is accounted for, the numerical result is significantly improved, and oscillation is eliminated or minimized. In this study, the term ‘anti-diffusion’ is used to describe the behavior of the numerical scheme that reduces physical diffusion.

B.2 Theoretical Development

Consider a steady-state scalar transport equation of the following form,

$$U\frac{\partial\varphi}{\partial x} = D\frac{\partial^2\varphi}{\partial x^2}$$

Equation B.1

The Taylor series expansion of Equation B.1 discretized with central difference scheme is as follows,

$$U\frac{\delta\varphi}{\delta x} - D\frac{\delta^2\varphi}{\delta x^2} = -\frac{U\Delta x^2}{3!}\frac{\delta^3\varphi}{\delta x^3} + \frac{D\Delta x^2}{2(3!)}\frac{\delta^4\varphi}{\delta x^4} - \frac{U\Delta x^4}{5!}\frac{\delta^5\varphi}{\delta x^5} + \frac{D\Delta x^4}{3(5!)}\frac{\delta^6\varphi}{\delta x^6} - \frac{U\Delta x^6}{7!}\frac{\delta^7\varphi}{\delta x^7} + \ldots$$

Equation B.2

The right-hand-side of Equation B.2 is truncation errors. By successively differentiating Equation B.1, it can be shown that,

$$U\frac{\partial^k\varphi}{\partial x^k} = D\frac{\partial^{k+1}\varphi}{\partial x^{k+1}} \qquad k = 2,3,4,\ldots,\infty$$

Equation B.3

Applying Equation B.3, the $(k+1)^{th}$ order derivative can be transformed to a $(k)^{th}$ order derivative. Applying the same procedure, the $(k)^{th}$ order derivative can be transformed to a $(k-1)^{th}$ order derivative. Eventually, it can be transformed to a second-order derivative. The relationship between the $(k)^{th}$ order derivative and the second order derivative will be as follows,

$$\frac{\partial^k \varphi}{\partial x^k} = \left(\frac{U}{D}\right)^{k-2} \frac{\partial^2 \varphi}{\partial x^2} \qquad k = 3,4,5,\ldots,\infty$$

Equation B.4

Using Equation B.4, all the right-hand-side derivatives of Equation B.2, can be transformed to second-order derivatives, which after some algebraic manipulation will be as follows,

$$U\frac{\delta\varphi}{\delta x} = D_1 \frac{\delta^2 \varphi}{\delta x^2}$$

$$D_1 = D\left(1 - \sum_{k=1}^{\infty} \frac{kP^{2k}}{(k+1)(2k+1)!}\right)$$

Equation B.5

where, $P = U\Delta x / D$ is the cell-Peclet number. Comparing Equation B.5 with Equation B.1, it is observed that the central difference scheme, reduces the physical diffusion from D to D_1 when applied to a steady-state one dimensional scalar transport equation. This is opposite to the upwind scheme, which increases the physical diffusion and makes the numerical result more diffusive. The existence of this anti-diffusion can be demonstrated by comparing the numerical result with the analytical solution. The analytical solution of Equation B.1 for boundary conditions, $\varphi(0) = 0$ and $\varphi(1) = 1$ is as follows,

$$\varphi(x) = \frac{1 - e^{Ux/D}}{1 - e^{U/D}}$$

Equation B.6

Figure B.1 shows the analytical and the numerical result for a small reach located very close to the downstream boundary where the gradient of $\varphi(x)$ is very steep. In this example, $U = 1, \Delta x = 0.01$ and $D = 0.01$, which yields $P = 1$. Figure B.1 shows that the numerical result underestimates $\varphi(x)$ compare to the analytical result, which should be due to the anti-diffusion effect. This underestimation is 18% at $x = 0.98$. Using Equation B.5, $D_1 = 0.0091$ was obtained for this D and when the analytical result was recomputed using D_1 (instead of D), excellent agreement with the numerical result was observed. This example supports that the difference between the numerical and the analytical result is due to the inherent anti-diffusion effect of the central-difference scheme.

B.3 Remedy

In this study, an iterative procedure is proposed to obtain an anti-diffusion free result. Our goal is to estimate $D*$ such that,

$$D^* \left(1 - \sum_{k=1}^{\infty} \frac{k \left(P^* \right)^{2k}}{(k+1)(2k+1)!} \right) = D$$

Equation B.7

where, $P^* = U\Delta x / D^*$. This equation can be solved using a numerical scheme (e.g. bisection method) for a finite value of k and the estimated D^* can be used in the central-difference scheme instead of D. It is observed that the first 5 terms in Equation B.7 is sufficient. In such case, the scheme can be considered as sixth order accurate. The central-difference scheme computes anti-diffusion based on D^* and when this anti-diffusion is subtracted from D^* (following Equation B.7), the true diffusion, D is reflected in the result.

In the previous example, $D^* = 0.0108$ yields $D = 0.01$ (Equation B.7). Figure B.2 shows two numerical results, one with D and the other with D^* as the diffusion term. It is observed that the numerical result with D^* compares very well with the analytical solution. This example supports the effectiveness of the anti-diffusion correction algorithm developed in this study.

In three-dimensional problems with varying velocities, the extra computation time needed to apply this diffusion correction scheme can be large. On the other hand, it is well-known that the central–difference scheme causes oscillation at most practical cell-Peclet numbers. As this diffusion correction algorithm reduces the effective cell-Peclet number, it helps to eliminate or minimize oscillations.

Figure B.3 shows an example where $P > 2$ and therefore oscillation is expected. In this example, $U = 1,\ \Delta x = 0.01,\ D = 0.0033,$ which yields $P = 3$, $D^* = 0.00531$, and $P^* = 1.88$. As $P^* < 2$ the anti-diffusion corrected numerical results are oscillation free.

This anti-diffusion correction algorithm also helps to minimize oscillation for cases with a very large P. In the above example, let $D = 10^{-5}$, which yields $P = 10^3, D^* = 0.003664648$, and P^*=2.72. Figure B.4 shows that while an anti-diffusion corrected central-difference scheme produces small under-shooting, an uncorrected central-difference scheme produces notorious oscillation. The reason for this small undershooting is that $P^* > 2$. The only remedy for this undershooting is the local refinement of grid points.

It is confirmed that adding anti-diffusion with D makes the numerical result diffusive and cannot solve the anti-diffusion effect. The reason is that, it reduces the cell-Peclet number and the numerical anti-diffusion is based on the reduced cell-Peclet number and is less than the added diffusion.

B.4 Inhomogeneous Problem

Consider an inhomogenous equation of the following form,

$$U\frac{\partial \varphi}{\partial x} = D\frac{\partial^2 \varphi}{\partial x^2} + f(x)$$

Equation B.8

where, *f*(*x*) is the source/sink term. Applying a similar derivation to the one stated previously, the following expression can be obtained,

$$\frac{\partial^k \varphi}{\partial x^k} = \left(\frac{U}{D}\right)^{k-2} \frac{\partial^2 \varphi}{\partial x^2} - \sum_{j=1}^{k-2} \frac{U^{k-j-2}}{D^{k-j-1}} \frac{d^j f(x)}{dx^j} \qquad k = 3,4,5,\ldots,\infty$$

Equation B.9

The second term on the right hand side appears due to the source/sink term. By substituting Equation B.9 into the Taylor series expansion equation and after algebraic manipulation, one can obtain two different correction terms, one for the diffusion term, and the other for the source/sink term. The correction for diffusion term is the same as in Equation B.7, which yields D^*. This D^* is to be used in the correction equation for source/sink term which is as follows,

$$f^*(x) = f(x) - C^*$$

$$C^* = \sum_{j=1}^{\infty} \sum_{k=j}^{\infty} \frac{k\Delta x^{2k}}{(k+1)(2k+1)!} \left(\frac{U}{D^*}\right)^{2k-2j+1} \frac{d^{2j-1} f(x)}{dx^{2j-1}} + \sum_{j=1}^{\infty} \sum_{k=j+1}^{\infty} \frac{k\Delta x^{2k}}{(k+1)(2k+1)!} \left(\frac{U}{D^*}\right)^{2k-2j} \frac{d^{2j} f(x)}{dx^{2j}}$$

Equation B.10

The $f^*(x)$ should be used instead of $f(x)$ in the numerical solver. It is observed that, if $f(x)$ is constant, no correction for source/sink term is necessary as all the derivatives of f are zero in such a case. An example is demonstrated for $f(x) = x$ in Figure B.5. The correction is applied on a relatively coarse grid computation (100 nodes), and the corrected result is compared with the uncorrected finer grid solution (1000 nodes). As the truncation error is smaller in the finer grid solution, the corrected coarse grid solution should be closer to the uncorrected finer grid solution. Figure B.5 shows the comparison between the finer grid solution, the coarse grid solution and the corrected coarse grid solution for U = 1 and D = 0.01. It is observed that the corrected coarse grid solution and the finer grid solution coincide perfectly.

B.5 Two Dimensional Problem

Consider a two-dimensional scalar transport equation of the following form,

$$U\frac{\partial\varphi}{\partial x}+V\frac{\partial\varphi}{\partial y}=D_x\frac{\partial^2\varphi}{\partial x^2}+D_y\frac{\partial^2\varphi}{\partial y^2}$$

Equation B.11

where, D_x and D_y are the diffusion coefficients in the x and y directions, respectively. For the two dimensional problem, it was not possible to convert all the truncation error terms to their second order derivatives. Hence, the correction formulation developed in this study is approximate. One needs to estimate D_x^* and D_y^* such that,

$$D_x^*-\frac{U^2\Delta x^2}{2(3!)D_x^*}+\frac{U^2\Delta y^2}{2(3!)D_y^*}=D_x$$

$$D_y^*-\frac{V^2\Delta y^2}{2(3!)D_y^*}+\frac{V^2\Delta x^2}{2(3!)D_x^*}=D_y$$

Equation B.12

This D_x^* and D_y^* are to be used in the two dimensional scalar transport equation. A two-dimensional bisection method can be employed to determine D_x^* and D_y^*. The performances of these corrections are assessed for the following conditions: U = 1, V = 0, D_x = 0.01, D_y = 0.002. The boundary conditions are:

$\varphi(0, W/2.05) = 1; \varphi(x,0) = 0; \varphi(0, y) = 0$, when $y < W/2.05$ and $y > W/2.05$, $\frac{\partial \varphi}{\partial y}(x, w) = 0$; and $\frac{\partial \varphi}{\partial x}(L, y) = 0$.The performance of the model is assessed by comparison with a finer grid solution. Figure B.6 shows the contours of $\varphi(x, y)$ in this two-dimensional test case. Figure B.7 shows the profiles obtained using a [75x75] grid, [25x25] grid, and [25x25] grid with diffusion correction. The diffusion corrected coarse grid solution makes a 60% improvement as compared to the fine grid solution. In this solution, D_x^* and D_y^* are computed as 0.007 and 0.002, respectively.

Another example is considered where $U = 0.5$, $V = 0.25$, $D_x = 0.01$, $D_y = 0.005$. The boundary conditions are the same as the previous case. Figure B.8 shows the profiles obtained using a coarse grid [25x25], fine grid [75x75] and diffusion corrected coarse grid solution. It appears that the diffusion correction makes some improvements when compared to the fine grid solution. The D_x^* and D_y^* are computed as 0.0093 and 0.0052, respectively.

It is interesting to compare the result with a second order upwind scheme. Figure B.9 shows the comparison between the second order upwind scheme, the central difference scheme, and the diffusion corrected central difference scheme; with all computations carried out using a [75x75] grid. At this grid, D_x^* and D_y^* are computed as 0.0099 and 0.005 respectively, which is almost equal to D_x and D_y. Hence, the central difference and the diffusion corrected central-difference scheme produce an identical result. It is observed that the second order upwind scheme also produces a very similar result due to its second order accuracy. The computation time for the second order upwind scheme is found as 117.8797 second in a computer having a 2 GHz processor speed and 2 GB RAM using the MATLAB. The central difference scheme and its diffusion correction system require 117.837 s. Hence, both approaches require nearly the same time.

B.6 Conclusions

This study shows that the central-difference scheme inherently causes anti-diffusion in a steady-state one-dimensional scalar transport equation. This anti-diffusion is an outcome of the truncation error. This is opposite to the upwind scheme which adds numerical diffusion and increases physical diffusion. An iterative method is proposed to solve the anti-diffusion problem. It is shown that this anti-diffusion correction algorithm helps to eliminate or to minimize numerical oscillation. If applied, this novel technique would improve the quality of the numerical results. This correction is also formulated for an inhomogenous equation. For two-dimensional problems, an approximate solution is developed.

B.7 References

Hall, C.A., Porsching, T.A., (1990), Numerical Analysis of Partial Differential Equations, Prentice Hall, NJ, 3-5.

Hayase, T., Humphrey, J.A.C., Greif, R., (1992), A consistently formulated QUICK scheme for fast and stable convergence using finite-volume iterative calculation procedures. J. Comput. Phys., 98, 108-118.

Huang, P.G., Launder, B.E., Leschziner, M.A., (1985), Discretization of non-linear convection processes: A broad-range comparison of four schemes. Comput. Methods. Appl. Mech. Eng., 48, 1-24.

Leonard, B.P., (1979), A stable and accurate convective modelling procedure based on quadratic upstream interpolation, Comput. Methods. Appl. Mech. Eng., 19, 59-98.

Patel, M.K., Markatos, N.C., Cross, M., (1985), A critical evaluation of seven discretization schemes for convection-diffusion equations, International Journal for Numerical Methods in Fluids,5, 225-244.

Patankar, S.V., (1980), Numerical Heat Transfer and Fluid Flow, Hemisphere Publishing Corporation, NY.

Spalding, D.B., (1972), A novel finite-difference formulation for differential expressions involving both first and second derivatives, Int. J. Numer. Methods. Eng, 4, 557-559.

Versteeg, H.K., Malalasekera W., (2007), An Introduction to Computational Fluid Dynamics: The Finite Volume Method, Pearson-Prentice Hall, 132.

Wang, Y., Hutter, K., (2001), Comparisons of numerical methods with respect to convectively dominated problems. International Journal for Numerical Methods in Fluids,37, 721-745.

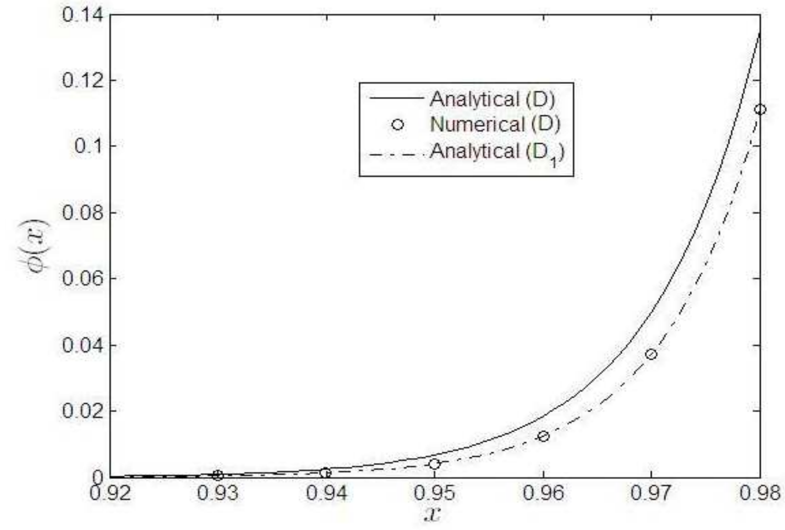

Figure B.1: Analytical and numerical result showing anti-diffusion effect.

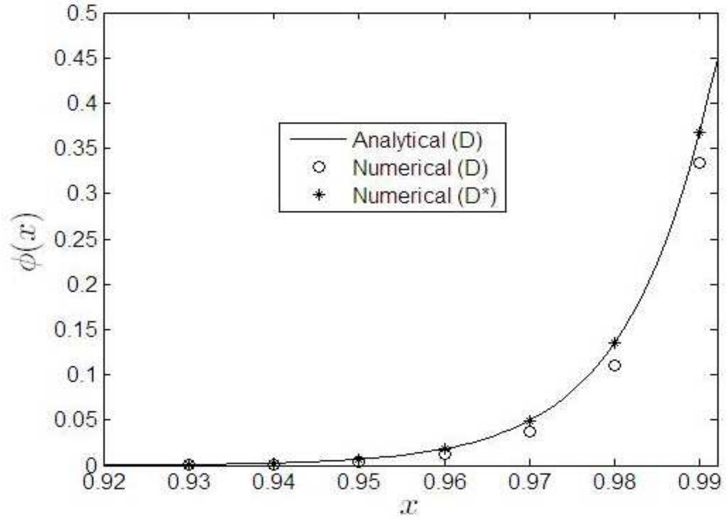

Figure B.2: Performance of anti-diffusion correction algorithm for $P = 1$.

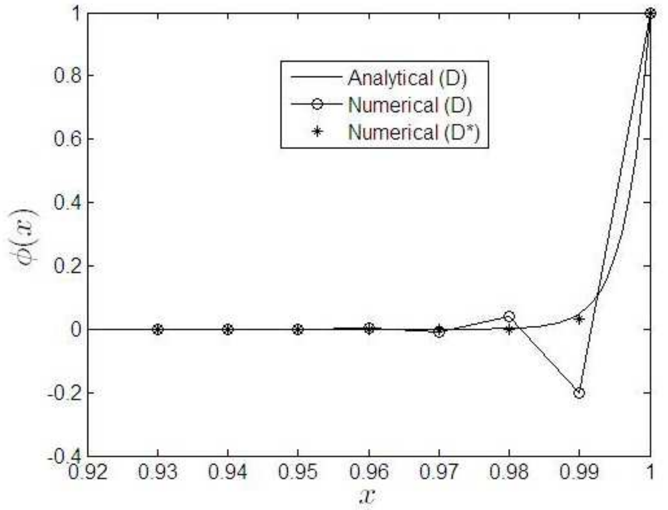

Figure B.3: Performance of anti-diffusion correction algorithm for $P = 3$.

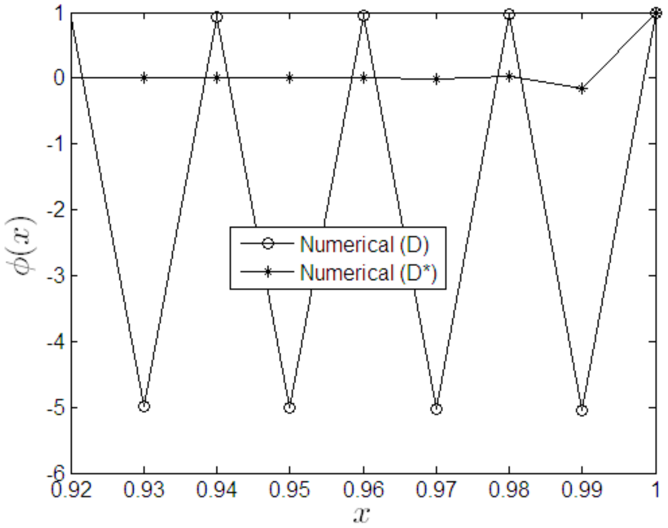

Figure B.4: Performance of the anti-diffusion correction algorithm for $P = 1000$.

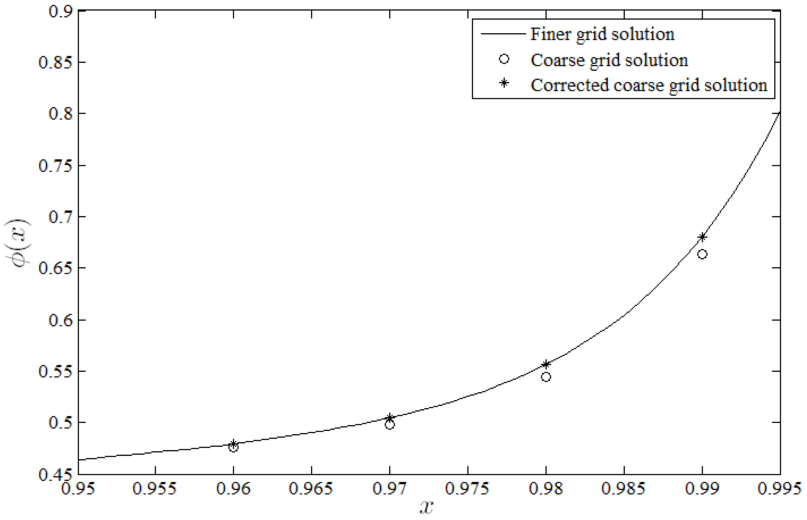

\

Figure B.5: Performance of correction algorithms for inhomogenous equation.

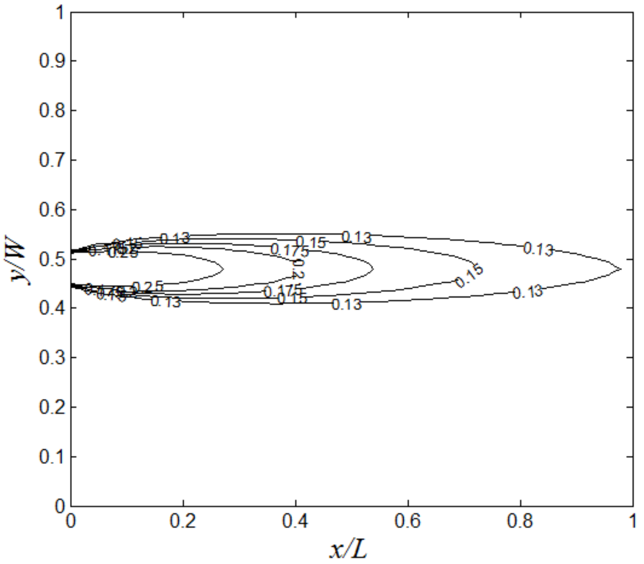

Figure B.6: Contours of $\varphi(x, y)$ in a two-dimensional test-case.

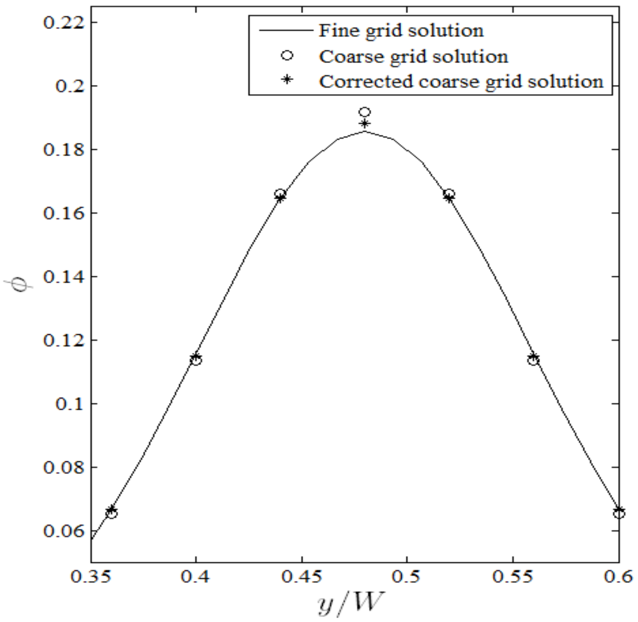

Figure B.7: Profiles of $\varphi(x, y)$ at $x/L = 0.5$ using fine grid [75x75], coarse grid [25x25] and coarse grid with diffusion correction.

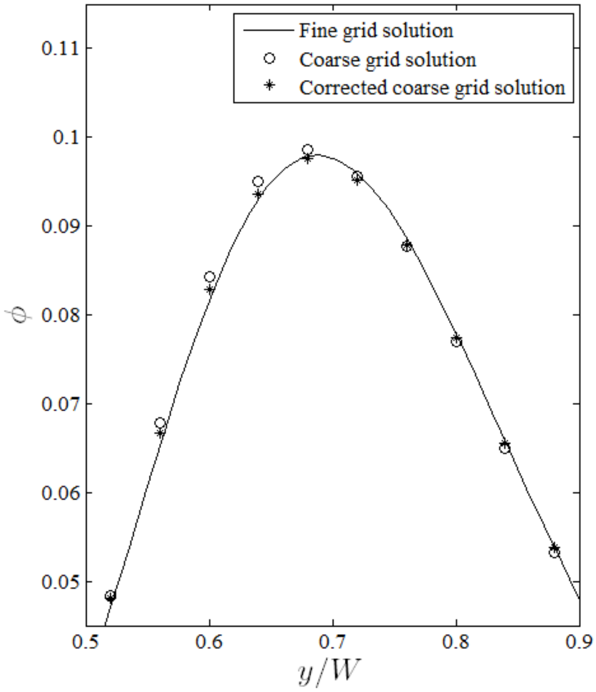

Figure B.8: Profiles of $\varphi(x, y)$ at x/L = 0.5 using fine grid [75x75], coarse grid [25x25] and coarse grid with diffusion correction for $V \neq 0$.

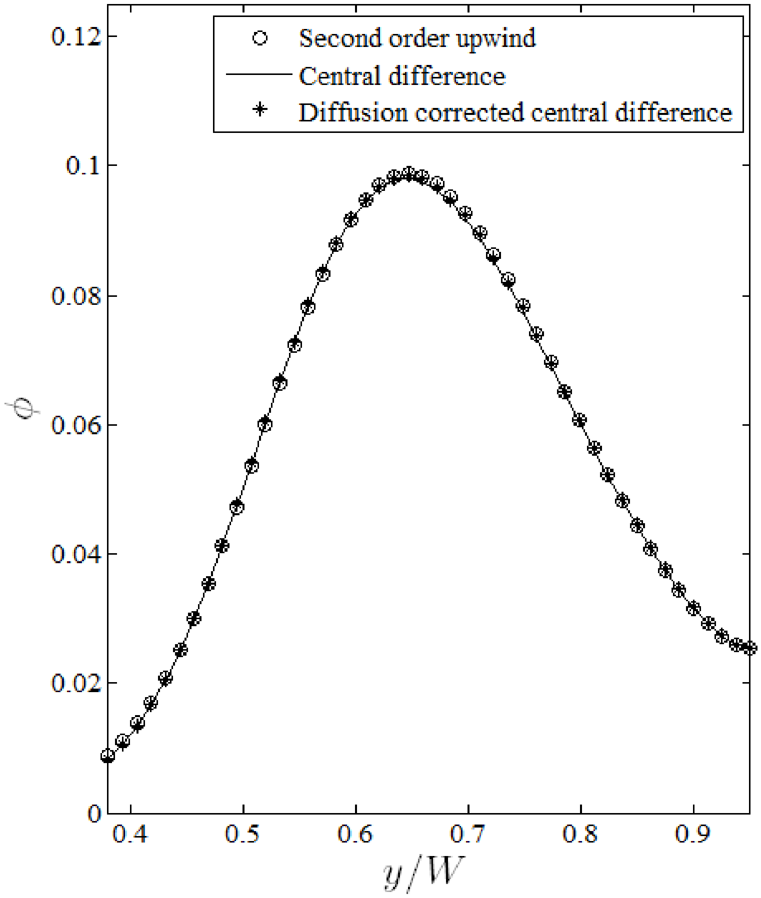

Figure B.9: Profiles of $\varphi(x, y)$ at $x/L = 0.5$ using second order upwind scheme, central difference and diffusion corrected central difference scheme.